East European Journal of Physics

No 2. 2022

2022

East European Journal of Physics

Східно-європейський фізичний журнал

ORIGINAL ARTICLES

East European Journal of Physics

No 2.   2022

INFLUENCE OF THE INERT GAS PRESSURE ON INTRINSIC STRESS IN DIAMOND-LIKE COATING DEPOSITED FROM VACUUM ARC CARBON PLASMA†

Alexandr I. Kalinichenko*, Vladimir E. Strel'nitskij

National Science Centre "Kharkiv Institute of Physics and Technology"
Kharkiv, 61108, str. Akademicheskaya 1, Ukraine
Corresponding Author: aikalinichenko@kipt.kharkov.ua

Within the framework of the model of the nonlocal thermoelastic peak of low-energy ion, the formation of intrinsic stress in a carbon coating deposited from the vacuum arc plasma in the argon atmosphere is theoretically studied. It is shown that the flow of particles bombarding the deposited coating contains, along with C^+ ions, also Ar^+ ions involved in the formation of intrinsic stress in the coating. The flux density of Ar^+ ions resulting from ionization losses of C^+ ions passing through the argon atmosphere is proportional to both the flux density of C^+ ions and the density (pressure) of argon. Expressions are obtained for the intrinsic stress in the deposited carbon coating depending on the bias potential on the substrate and the argon pressure for the cases of both constant and pulsed potentials. The analysis of the obtained expressions shows that the intrinsic stress in the carbon coating decrease with increasing argon pressure.
Keywords: Diamond-like carbon coatings; Plasma-ion deposition; Vacuum arc; Argon atmosphere; Thermal peaks; Intrinsic stress; Growth rate
PACS: 81.15-z, 68.60Bs

Diamond-like carbon (DLC) coatings are of significant interest for applications associated with extreme tribological conditions, providing high efficiency, performance and reliability. The strong covalent sp^3 bonding in ta-C coatings provides high mechanical hardness, toughness, chemical and thermal stability, making them highly suitable for harsh tribological conditions, including high speeds, loads and temperatures.

Due to the unique combination of properties, thick microcrystalline diamond-like films are most preferred for use in tools, while thinner nanocrystalline DLC coatings are widely used for surface modification of parts used in mechanical engineering, aerospace, medicine, micromechanics, and other industries. Such coatings are characterized by low coefficient of friction, chemical inertness, biocompatibility and high radiation resistance. [1-5].

The development of equipment and processes for high-quality DLC deposition over the large area is the urgent and important task, the solution of which will increase the productivity of the process, as well as expand the list of processed articles. In addition, there is a great need for the deposition of diamond-like carbon on the surface of articles with complex shapes (cylindrical, spherical and others, for example, the friction joints of endoprostheses). Improving the characteristics and functional properties of DLC is impossible without knowledge of the physical mechanisms which determine the deposition rate and the processes of formation of the structure and phase composition of the coating material. Therefore, it is important to theoretically study the mechanisms of DLC synthesis, to reveal the role of the bombardment of the growth surface with low-energy ions (from 0.1 to ~ 1 keV) in the sputtering and activation of radiation-stimulated processes and the effect of deposition conditions on intrinsic stress in the coating.

The important type of the process of DLC production is the deposition of carbon coatings from the carbon plasma of the vacuum arc in sufficiently rarefied atmosphere of the inert gas. For obtaining coatings with parameters providing the best performance characteristics, such as hardness and high adhesion to the substrate, it is necessary to investigate the dependence of the properties of coatings on the type of inert gas and its pressure. The key parameter providing the above properties of the DLC is the intrinsic stress arising during the coating deposition.

In this paper, we study the dependence of intrinsic stress in the deposited coating on the pressure of the inert gas in the atmosphere of working installation.

MATHEMATICAL MODEL

We will assume that the flux of C^+ ions is deposited on the substrate surface in atmosphere of easily ionized inert gas, argon. As a result, the mixture of ion fluxes falls on the deposited surface: the flux j_1 of C^+ ions knocked out from the cathode and the flux j_2 of Ar^+ ions generated when gas atoms collide with the flux of C^+ ions. Assuming that the number of ionized Ar atoms is small compared to the initial amount, the following expression can be written for the flux j_2:

$$j_2 = \alpha P j_1, \tag{1}$$

Here P is the argon pressure, α is the coefficient that, generally, depends on the design of the installation.

The initial energy E_0 of C^+ ions in the setup chamber is 20 to 25 eV (up to the thin near-surface layer near the substrate, where the ions are additionally accelerated by the bias potential). Modeling the passage of the low-energy C^+

ion with such an energy through the argon atmosphere using the SRIM2000 software package shows that the following approximate expression for the average projective ion path is valid: L_C, cm = 0.076/P, where P is given in Torr units. The ionization loss of the C + ion can be estimated from the expression $\Delta E_{ion} \sim 0.3 E_0 D / L_C =$, where D is the characteristic distance traveled by the ion in the gaseous atmosphere of the vacuum chamber, specified in cm. The coefficient 0.3 corresponds to the fraction of ionization energy losses of the C^+ ion ~ 30%. The above estimate is valid under the condition $D < L_C$ that is satisfied at pressures P <10^{-3} Torr. Assuming that all ionization losses of the ion C^+ are spent on the formation of Ar^+ ions, we obtain the following estimate for the number of Ar^+ ions formed by one C^+ ion: $N_{Ar} \sim 10DP$, that is, $\alpha \sim 10D$. Here we use the following average ionization potential of Ar I_{Ar} = 11.6 eV. For the coating deposition systems used, the conditions $P < 10^{-3}$ Torr and $D < 10^2$ cm are satisfied, whence $\alpha P < 1$ follows.

When deriving the formula for intrinsic stress, basically, the line of reasoning used in works [6-9] is repeated. At this, the model of a nonlocal thermal peak (NTP) of a low-energy ion is widely used - an overheated and overstressed nanometer region near the ion trajectory in the target material, in which thermalized phonon losses of the ion contain [10]. Computer simulation using the SRIM2000 software package [11] has shown that the NTP can be approximated by a spherical segment adjacent to the target surface, the center of which lies in the middle of the average projective range of the ion. The effective lifetime t_T, volume $V(t, E)$, and temperature $T(t, E, T_0)$ of the NTP of the ion are calculated within the framework of the previously developed model [10, 11]. So, the volume of the near-surface NTP is found by the formula

$$V(E, t) = \pi \left[\frac{2}{3} R(E, t)^3 + \frac{L(E)}{2} R(E, t)^2 - \frac{1}{3} \frac{L(E)^3}{8} \right],$$ (2)

where $R(E, t) = \frac{L(E)}{2} + 2\sqrt{\kappa(\tau + t)}$ is the radius of the NTP created by the ion with energy E at time t, $L(E)$ is the average projective range of the ion, $\tau \sim 10^{-13}$ s. is the ion-ion relaxation time; κ is the phonon thermal diffusivity of the coating material. Temperature $T(t, E)$ in the NTP is calculated from the equation that takes into account the dependence of the heat capacity on temperature [10, 12]:

$$\frac{\eta(E)E}{\rho C V(E, t)} = TD\left(\frac{\theta}{T}\right) - T_0 D\left(\frac{\theta}{T_0}\right),$$ (3)

where ρ is the density, $C = 3v_a k_B / M$ is the high-temperature limit of the heat capacity of the target material, $\eta(E)$ is the fraction of phonon losses of the ion with energy E in the target material, T_0 is the substrate temperature, θ is the Debye temperature of the target material, k_B is the Boltzmann constant, v_a is the number of atoms in the molecule of the target material (for carbon coating $v_a = 1$), $D(x)$ is the Debye function having the form [12]:

$$D(x) = \frac{3}{x^3} \int_0^x \frac{z^3 \, dz}{e^z - 1}.$$ (4)

The lifetime $t_T(E)$ of the NTP is determined by the rate of its cooling. Assuming that the peak is cooled only by thermal conductivity, we obtain for the effective cooling time of the peak $t_T(E) = R(E, 0)^2 / 4\kappa$. Functions $L(E)$ and $\eta(E)$ were calculated using the SRIM2000 software package [11]. The results of calculating the functions $\eta(E)$ for C^+ and Ar^+ ions in the carbon coating are shown in Fig. 1.

The dependences of the NTP volumes of C^+ and Ar^+ ions in the carbon coating on the ion energy are shown in Fig. 2.
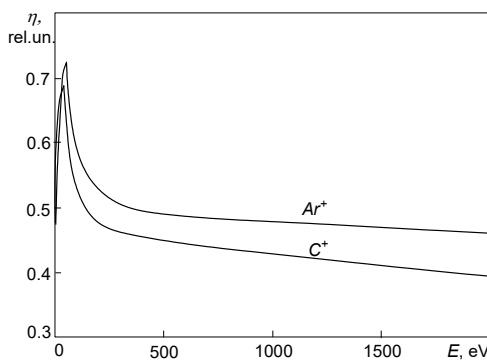
Figure 1. Phonon loss functions for C^+ and Ar^+ ions in the DLC coating.
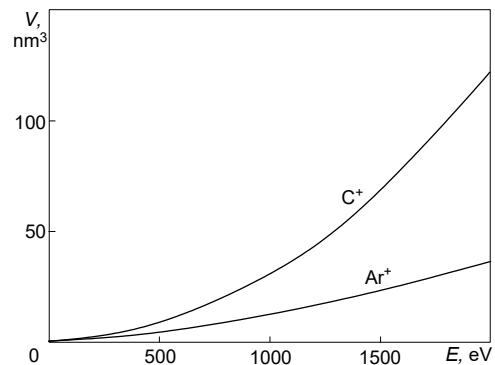
Figure 2. Volumes of NTP of C + and Ar + ions in the DLC coating depending on the ion energy

The results of calculating the NTP temperatures as functions of the ion energy are shown in Fig. 3. In the calculations, the substrate temperature was assumed to be $T_0 = 300$ K.

The data obtained on the characteristics of the NTP allow us describing the intrinsic stress formation in the coating deposited from mixed flow of C^+ and Ar^+ ions. It is assumed that intrinsic stresses are formed as a result of two simultaneous but oppositely directed processes: 1) stress generation due to implantation of the incident ion beam and 2) stress relaxation due to thermally activated processes of defect migration in the NTP of ions [6]. In addition, the stated model [7–9], like the Davis's one [6], is based on the hypothesis of proportionality between the density of defects formed as a result of ion scattering by target atoms and the volumetric deformation of the target.

The rate of defects formation by ions of the i-th species, per unit surface of the coating, is proportional to the ion flux density j_i and the number of defects $\zeta_i(E)$ formed by one ion of the i-th species. In papers [6,7], the approximation $\zeta_i(E) \sim \sqrt{E}$ was used [13]. In this work, the defect formation functions are calculated numerically using the SRIM2000 program code [9, 11] (see Fig. 4).
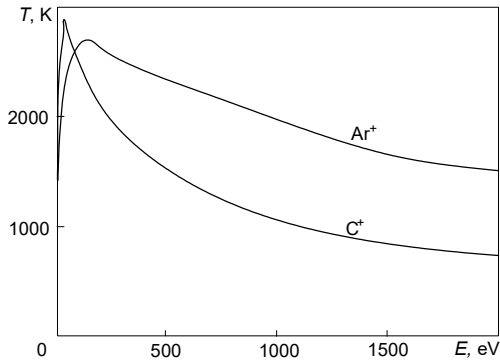
Figure 3. Temperatures in the peaks of C^+ and Ar^+ ions in the carbon coating depending on the ion energy.
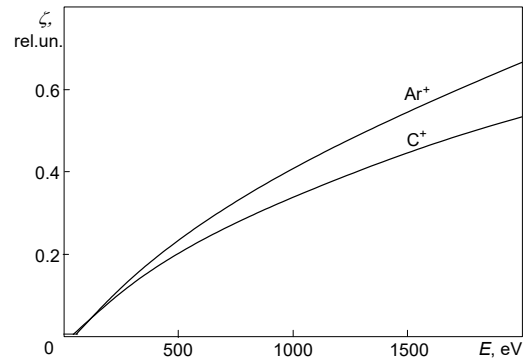
Figure 4. Functions of defect formation of C^+ and Ar^+ ions in the carbon coating.

Thus, the total rate of defect formation by the mixed beam of ions of two species is determined by the expression:

$$\dot{n}_d(U) \sim j_1 \zeta_1(E_1(U)) + j_2 \zeta_2(E_2(U)). \tag{5}$$

Using (1), we obtain from (5):

$$\dot{n}_d((U)) \sim j_1 \left(\zeta_1(E_1(U)) + \alpha P \zeta_2(E_2(U)) \right). \tag{6}$$

Here we used the notation $E_i = q_i(U + U_0) + E_{0i}$, q_i is the charge of the i-th species ion, U_0 is the floating potential, E_{0i} is the initial energy of the i-th species ion.

The opposite process of stress relaxation is determined by the number of thermally activated transitions $w_i(E)$ of atoms in the NTP of the i-th species ion with energy E.
Function

$$w_i(U) = n_0 \nu \int_0^{t_T} V_i(t, E_i) \, e^{-\frac{u}{k_B T_i(t,E_i,T_0)}} \, dt , \tag{7}$$

specifies the number of thermally activated transitions in the NTP of the ion, which determine the migration rate of defects with the activation energy u and, therefore, the stress relaxation rate at the target temperature T_0.

The rate of defect loss, per unit area, is proportional to $w_i(E)$, to the fraction of defects n/n_0 and to density of the implanted ion flux j_i. After summing up the contributions of two species ions to the migration process, we obtain the following expression for the rate of defect loss:

$$\dot{n}_R(U) = \frac{n}{n_0} \left[j_1 w_1(E_1) + j_2 w_2(E_2) \right] = j_1 \frac{n}{n_0} \left(w_1(E_1) + \alpha P w_2(E_2) \right). \tag{8}$$

The resulting rate, per unit area, with which defects are implanted in the film, is equal to $j_1 n / n_0$. Here we have taken into account that only ions of the 1st species (carbon ions) build up the coating. On the other hand, the resulting rate of introduction of defects is set by the difference between the rate of appearance of defects due to implantation and

the rate of their loss due to thermally activated migration. Consequently, the condition of constancy of density of defects leads to the relation:

$$ j_1 \frac{n}{n_0} = \dot{n}_d - \dot{n}_R . \tag{9} $$

Substituting $\dot{n}_d$ and $\dot{n}_R$ from Eqs. (6), (8) in Eq. (9) and expressing in the resulting equation the fraction n/n_0 of implanted ions in the film, we obtain for intrinsic stress in the case of the constant bias potential (so called the direct current (DC) mode):

$$ \sigma(U,P) = \frac{AE_Y}{1-\Pi} \frac{\zeta_1\left(E_1(U)\right) + \alpha P \zeta_2\left(E_2(U)\right)}{1 + w_1\left(E_1(U)\right) + \alpha P w_2\left(E_2(U)\right)}, \tag{10} $$

where E_Y and Π are the Young's modulus and the Poisson's ratio of the coating material, correspondingly. Here, we used the relationship $\sigma = E_Y \varepsilon / (1-\Pi)$ between stress σ and volumetric deformation ε, which is determined by the density of defects n/n_0. Coefficient A is found by comparing the theoretical curve with the experimental data.

Expression (10) was generalized to the case of the pulse potential mode [8]. Intrinsic stress in the pulse potential mode is given by the expression:

$$ \sigma(U,P) = \frac{AE_Y}{1-\Pi} \frac{\left(\zeta_1\left(E_1(U)\right) + \alpha P \zeta_2\left(E_2(U)\right)\right) ft_p + \left(\zeta_1\left(E_1(0)\right) + \alpha P \zeta_2\left(E_2(0)\right)\right)\left(1 - ft_p\right)}{1 + \left(w_1\left(E_1(U)\right) + \alpha P w_2\left(E_2(U)\right)\right) ft_p + \left(w_1\left(E_1(0)\right) + \alpha P w_2\left(E_2(0)\right)\right)\left(1 - ft_p\right)}, \tag{11} $$

where, t_p is the duration of the high voltage pulse, f is the pulse repetition rate.

When calculating the intrinsic stress in the deposited coating, it is necessary to take into account the deposition temperature T_0, which can vary significantly with the energy of the deposited ions, since the ion flux heats the coating surface. In the approximation of the linear theory of thermal conductivity with constant coefficient of thermal conductivity and in the stationary mode, the deposition temperature T_0 is related to the bias potential U by linear dependence:

$$ T_0(U) = T_{00} + \lambda q\left[\left(U_0 + E_0\right)\left(1 - ft_p\right) + \left(U + U_0 + E_0\right) ft_p\right]\left(1 + \alpha P\right), \tag{12} $$

where T_{00} is the temperature of the non-irradiated substrate. The average charge q of C^+ and Ar^+ ions, according to experimental data, is, with sufficient accuracy, equal to the elementary (proton) charge. The value λ depends on the technical parameters of the coating deposition installation. The value of λ was chosen from the condition that the deposition temperature was equal to its experimental value at known energy of the deposited ions.

RESULTS AND DISCUSSION

In Fig. 5 shows the dependence of intrinsic stress on the bias potential for different values of the parameter αP in both cases of the direct current (DC) and pulse potential regimes. The calculations were performed for the case of the absence of the argon atmosphere $\alpha P = 0$, and for the case of $\alpha P = 1$. As can be seen from the Fig. 5, the addition of Ar^+ ions to the flow of incident particles does not change behavior of dependence $\sigma(U)$ but leads to a certain decrease of intrinsic stress in the deposited carbon coating.
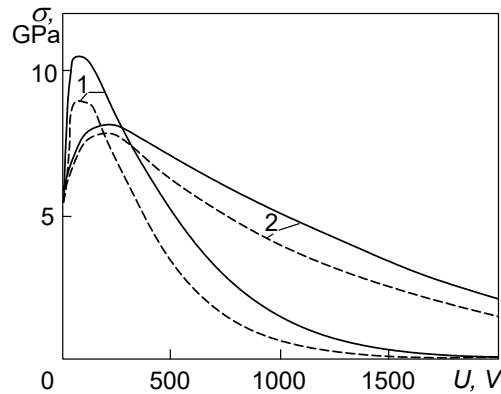
Figure 5. Dependence of intrinsic stress in deposited carbon coating on bias potential at different pressures of inert gas. Curves 1 – the case of the DC regime ($ft_p = 1$), curves 2 – the case of the pulse potential regime ($ft_p = 0.12$). Solid curves correspond to $aP = 0$, and dashed curves correspond to $\alpha P = 1$.

To study the dependence of intrinsic stress on the inert gas pressure P, we represent expression (10) in the form:

$$\sigma(P) = B\frac{1+aP}{1+bP}, \tag{13}$$

where

$$B(U) = \frac{AE_Y}{1-\Pi}\frac{\zeta_1(E_1(U))}{1+w_1(E_1(U))}, \tag{14}$$

$$a(U) = \frac{\alpha\zeta_2(E_2(U))}{\zeta_1(E_1(U))}, \tag{16}$$

$$b(U) = \frac{\alpha w_2(E_2(U))}{1+w_1(E_1(U))}. \tag{17}$$

are the positive definite functions of the bias potential U.

For given values of U, the parameters B, a, b are constants. Constant B is equal to the intrinsic stress in the coating obtained at zero inert gas concentration. It can be seen from (13) that the intrinsic stress is the fractional-rational function of pressure P. The behavior of the fractional-rational function (13) with the change in the argument P depends on the ratio between its coefficients a and b. So, at zero concentration of the inert gas (at $P = 0$) we have $\sigma(0) = B, \quad \sigma'(0) = B(a-b)$. Thus, the slope of the stress curve is proportional to the difference *(a-b)* near the point $P = 0$. As the pressure P increases, the function $\sigma(P)$ tends to the asymptotics Ba/b.

Analysis of Eq. (11) shows that it can also be represented as the fractional-rational function of pressure P:

$$\sigma_1(P) = B_1\frac{1+a_1P}{1+b_1P}, \tag{18}$$

where

$$B_1(U) = \frac{AE_Y}{1-\Pi}\frac{\zeta_1(E_1(U))ft_p + \zeta_1(E_1(0))(1-ft_p)}{1+w_1(E_1(U))ft_p + w_1(E_1(0))(1-ft_p)}, \tag{19}$$

$$a_1(U) = \frac{\alpha\left[\zeta_2(E_2(U))ft_p + \zeta_2(E_2(0))(1-ft_p)\right]}{\zeta_1(E_1(U))ft_p + \zeta_1(E_1(0))(1-ft_p)}, \tag{20}$$

$$b_1(U) = \frac{\alpha\left[w_2(E_2(U))ft_p + w_2(E_2(0))(1-ft_p)\right]}{1+w_1(E_1(U))ft_p + w_1(E_1(0))(1-ft_p)}. \tag{21}$$

Dependence of intrinsic stress on the parameter αP for three different bias potentials is shown in Fig. 6. The solid curves correspond to the DC regime deposition whereas the dashed curves – to the pulse potential regime.
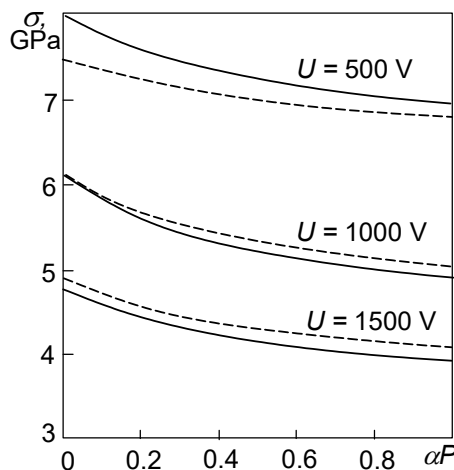
Figure 6. Dependence of intrinsic stress in the carbon coating on pressure of inert gas at different bias potentials on the substrate. The solid curves correspond to the DC regime ($ft_p = 1$), the dashed curves – to the pulse potential regime ($ft_p = 0.12$).

As can be seen from fig. 6, in the case under consideration, the condition is satisfied $a - b < 0$, since the intrinsic stress decreases with the increase in the pressure of the inert gas.

Note that the case of carbon coating deposition in the inert gas atmosphere differs from a similar case of deposition of the TiN coating, since in the latter case the increase in pressure led not to the decrease, but, on the contrary, to the increase in intrinsic stress in the TiN coating [14].

CONCLUSION

1. During the deposition of the carbon coating from the vacuum arc plasma in the argon atmosphere, the flow of particles, bombarding the deposited coating, consists of the mixture of C^+ and Ar^+ ions. The flux density of Ar^+ ions resulting from ionization loss of C^+ ions passing through the argon atmosphere is proportional to both the flux density of C^+ ions and the density (pressure) of argon.

2. Expressions are obtained for the intrinsic stresses in the deposited carbon coatings depending on the bias potential on the substrate for the modes of both the DC and the pulsed potential.

3. The analysis of the obtained expressions shows that the intrinsic stress in the case of deposition of the carbon coating in the argon atmosphere decreases with the increase of argon pressure P.

Alexandr I. Kalinichenko, https://orcid.org/0000-0002-5675-3947
Vladimir E. Strel'nitskij, https://orcid.org/0000-0001-6047-6981

REFERENCES

[1] Y. Lifshitz, Diamond Relat. Mater. **8**, 1659 (1999), https://doi.org/10.1016/S0925-9635(99)00087-4
[2] J. Robertson, Materials Science and Engineering, **R37**, 129 (2002). https://doi.org/10.1016/S0927-796X(02)00005-0
[3] A. Erdemir, and J.M. Martin. Superior wear resistance of diamond and DLC coatings, Current Opinion in Solid State and Materials Science, **22**(6), 243 (2018). https://doi.org/10.1016/j.cossms.2018.11.003
[4] A. Tyagi; R. Walia, Q. Murtaza, S.M. Pandey, P.K. Tyagi, and B. Bajaj, A critical review of diamond like carbon coating for wear resistance applications, Int. J. Refract. Met. Hard Mater. **78**, 107 (2019). https://doi.org/10.1016/j.ijrmhm.2018.09.006.
[5] R. Hauert, K. Thorwarth, and G. Thorwarth. An overview on diamond-like carbon coatings in medical applications, Surf. Coat. Technol. **233**, 119 (2013). https://doi.org/10.1016/j.surfcoat.2013.04.015.
[6] C.A. Davis. A simple model for the formation of compressive stress in thin films by ion bombardment, Thin Solid Films, **226**, 30 (1993). https://doi.org/10.1016/0040-6090(93)90201-Y.
[7] A.I. Kalinichenko, S.S. Perepelkin, and V.E. Strel'nitskij. Dependence of intrinsic stress and structure of ta-C film on ion energy and substrate temperature in model of the non-local thermoelastic peak, Diamond & Related Materials, **19**, 996 (2010). https://doi.org/10.1016/j.diamond.2010.03.001
[8] A.I. Kalinichenko, S.S. Perepelkin, and V.E. Strel'nitskij. Intrinsic stresses in DLC coatings deposited in modes of DC and pulse bias potentials, PAST, **1**(95), 252 (2015). http://dspace.nbuv.gov.ua/handle/123456789/82254
[9] A.I. Kalinichenko, S.S. Perepelkin, and V.E. Strel'nitskij, Calculation of intrinsic stresses in the diamond-like coatings produced by plasma ion deposition in modes of DC and pulse bias potentials, IOP Conf. Series: Materials Science and Engineering, **81**, 012049 (2015). https://doi.org/10.1088/1757-899X/81/1/012049
[10] A.I. Kalinichenko, S.S. Perepelkin, and V.E. Strel'nitskij, Thermodynamic conditions of ta-C formation at implantation of noble-gas ions in carbon, Diamond and Related Materials, **15**(2-3), 365 (2006). https://doi.org/10.1016/j.diamond.2005.10.022
[11] F. Ziegler, J. P. Biersack, U. Littmark. *The Stopping and Range of Ions in Solids*, (Pergamon Press, New York, 1996), pp. 297.
[12] L.D. Landau, and E.M. Lifshitz, *Statistical Physics, 3-rd Edition, Part 1*, (Nauka, Moscow, 1980), pp. 567.
[13] H. Windischmann, An intrinsic stress scaling law for polycrystalline thin films prepared by ion beam sputtering, J. Applied Physics, **62**(5), 1800 (1987). https://doi.org/10.1063/1.339560.
[14] V.V. Vasyliev, A.I. Kalinichenko, E.N. Reshetnyak, G. Taghavi Pourian Azad, M. Ürgen, and V.E. Strel'nitskij, Experimental and modeling study on the role of Ar addition to the working gas on the development of intrinsic stress in TiN coatings produced by filtered vacuum-arc plasma, Thin Solid Films, **642**, 207 (2017). https://doi.org/10.1016/j.tsf.2017.08.033.

ВПЛИВ ТИСКУ ІНЕРТНОГО ГАЗУ НА ВНУТРІШНІ НАПРУЖЕННЯ В АЛМАЗОПІДОБНОМУ ПОКРИТТІ, ЩО ОСАДЖУЄТЬСЯ З ВУГЛЕЦЕВОЇ ПЛАЗМИ ВАКУУМНОЇ ДУГИ
О.І. Калініченко, В.Є. Стрельницький
Національний науковий центр «Харківський фізико-технічний інститут»
61108, Україна, Харків, Академічна, 1

В рамках моделі нелокального термопружного піка низькоенергетичного іона теоретично досліджується виникнення внутрішніх напружень у вуглецевому покритті, що осаджується з плазми вакуумної дуги в аргоновій атмосфері. Показано, що потік часток, які бомбардують покриття, що осаджується, містить поряд з іонами C^+ також іони Ar^+, що беруть участь у формуванні внутрішніх напружень в покритті. Щільність потоку іонів Ar^+, що виникли в результаті іонізаційних втрат іонів C^+, що проходять через атмосферу аргону, пропорційна як щільності потоку іонів C^+, так і щільності (тиску) аргону. Отримані вираження для внутрішніх напружень в вуглецевому покритті, що осаджується, залежно від потенціалу зміщення на підкладці і тиску аргону для випадків як постійного, так і імпульсного потенціалів. Аналіз отриманих виразів показує, що внутрішні напруження у вуглецевому покритті зменшуються зі збільшенням тиску аргону.

Ключові слова: алмазоподібні вуглецеві покриття, плазмо-іонне осадження, вакуумна дуга, атмосфера аргону, теплові піки, внутрішня напруга, швидкість росту

SOLUTIONS OF THE SCHRÖDINGER EQUATION WITH HULTHÉN-SCREENED KRATZER POTENTIAL: APPLICATION TO DIATOMIC MOLECULES†

Etido P. Inyang[a,b]*, P.C. Iwuji[b], Joseph E. Ntibi[b], E.S. William[b], E.A. Ibanga[a]

a Department of Physics, National Open University of Nigeria, Jabi, Abuja, Nigeria
b Theoretical Physics Group, Department of Physics, University of Calabar, Calabar, P.M.B 1115, Nigeria
Corresponding author: etidophysics@gmail.com; einyang@noun.edu.ng

In this study, the Schrödinger equation with the Hulthén plus screened Kratzer potentials (HSKP) are solved via the Nikiforov-Uvarov (NU) and the series expansion methods. We obtained the energy equation and the wave function in closed form with Greene-Aldrich approximation via the NU method. The series expansion method was also used to obtain the energy equation of HSKP. Three distinct cases were obtained from the combined potentials. The energy eigenvalues of HSKP for HCl, LiH, H_2, and NO diatomic molecules were computed for various quantum states. To test the accuracy of our results, we computed the bound states energy of HCl and LiH, for a special case of Kratzer and screened Kratzer potentials, which are in excellent agreement with the report of other researchers.
Keywords: Schrödinger equation; Nikiforov-Uvarov method; series expansion method; Hulthén plus screened Kratzer Potentials; Diatomic molecules
PACS: 31.15.-p

The determination of the dynamics of non-relativistic particles in quantum mechanics such as, the thermodynamic properties of the system, mass spectra of mesons, among others, is possible through the solutions of the Schrödinger equation (SE) [1-5]. The solutions of the SE with dissimilar potential functions have been investigated by many authors [6-10]. Also, different methods have been employed in obtaining either exact or approximate solutions of the SE such as, Asymptotic iteration method (AIM) [11,12], Laplace transformation method [13,14], super symmetric quantum mechanics (SUSYQM) [15], the Nikiforov-Uvarov (NU) method [16-28], the Nikiforov-Uvarov-Functional Analysis (NUFA) method [29], the series expansion method (SEM) [30-34], the analytical exact iterative method (AEIM) [35], the WKB approximation method [36-41] and others [42,43].

Recently, many authors have devoted interest in investigating bound states energy of countless diatomic molecules (DMs) with a single potential function and a combined potential function [44-46]. For instance, Inyang et al., [47] combined Eckart and Hellmann potential function to study some selected DMs. Also, Obogo et al. [48], investigated some selected DMs through the solution of SE with a combined potential using the NU method. In addition, Edet and Ikot, [49] studied some DMs with the shifted Deng-Fan potential. Furthermore, Edet et al. [50] studied some DMs with Deng-Fan plus Eckart potentials. Motivated by the success of other researchers, we seek to combine Hulthén plus screened Kratzer potentials (HSKP) to study selected DMs through the solutions of the SE using the NU and series expansion methods. The Hulthén potential (HP) [51] is vital in exploring the interaction existing between two particles. It is useful in areas of nuclear and molecular physics, atomic physics, condensed matter physics, and chemical physics [52].

On the other hand, Ikot et al. [53] proposed the screened Kratzer potential (SKP), which finds application in molecular physics, and many authors have employed in literature [54-56].

The aim of this study is to obtain the solutions to the SE with the HSKP and apply it to study some selected DMs. The essence of combining at least two potential models is to have a better results, because potential with more fitting parameters tends to give a better results [57]. The combined potential is of the form:

$$V(p) = -\frac{Z_1 e^{-\vartheta p}}{1 - e^{-\vartheta p}} - \frac{Z_2 e^{-\vartheta p}}{p} + \frac{Z_3 e^{-\vartheta p}}{p^2}, \tag{1}$$

where Z_1 is the potential strength for Hulthén, ϑ is the screening parameter. The letter $Z_2 \equiv 2 D_e r_e$ and $Z_3 \equiv D_e r_e^2$, here D_e is dissociation energy and r_e is the equilibrium bond length.

THE SOLUTIONS OF THE SE WITH HSKP VIA THE NU METHOD

In this research, the NU method [58] and SEM [59] is adopted, which are based on solving the second-order differential equation. The details of the NU can be found in Ref. [58]. The SE characterized by a given potential $V(p)$ reads [60]:

$$\left(-\frac{\hbar^2}{2\mu}\nabla^2 + V(p)\right)\Psi_{nl}(p) = E_{nl}\Psi_{nl}(p), \tag{2}$$

where $\Psi_{nl}(p)$ is the Eigen functions, E_{nl} is the energy eigenvalues of the quantum system, μ is the reduced mass of the system, $\hbar$ is the reduced Planck's constant and p is radial distance from the origin.

Substituting Eq. (1) into Eq. (2) gives Eq. (3),

$$\frac{d^2\Psi_{nl}(p)}{dp^2} + \left[\frac{2\mu E_{nl}}{\hbar^2} + \frac{2\mu Z_1 e^{-\vartheta p}}{\hbar^2(1-e^{\vartheta p})} + \frac{2\mu Z_2 e^{-\vartheta p}}{\hbar^2 p} - \frac{2\mu Z_3 e^{-\vartheta p}}{\hbar^2 p^2} - \frac{l(l+1)}{p^2}\right]\Psi_{nl}(p) = 0 \tag{3}$$

To solve Eq. (3), the Greene-Aldrich approximation scheme [61] is introduce to deal with the centrifugal obstacle. This scheme is a good approximation to the centrifugal obstacle which is valid for $\vartheta \ll 1$, and its reads,

$$\frac{1}{p^2} \approx \frac{\vartheta^2}{\left(1-e^{-\vartheta p}\right)^2}. \tag{4}$$

Pluging Eq. (4), to Eq. (3), Eq.(5) is

$$\frac{d^2\psi_{nl}(p)}{dp^2} + \left[\frac{2\mu E_{nl}}{\hbar^2} + \frac{2\mu Z_1 e^{-\vartheta p}}{\hbar^2(1-e^{-\vartheta p})} + \frac{2\mu Z_2 \vartheta e^{-\vartheta p}}{\hbar^2(1-e^{-\vartheta p})} - \frac{2\mu Z_3 \vartheta^2 e^{-\vartheta p}}{\hbar^2(1-e^{-\vartheta p})^2} - \frac{\vartheta^2 l(l+1)}{(1-e^{-\vartheta p})^2}\right]\psi_{nl}(p) = 0 \tag{5}$$

We set

$$y = e^{-\vartheta p}. \tag{6}$$

Differentiating Eq. (6), we have Eq. (7) as,

$$\frac{d^2\Psi(p)}{dp^2} = \vartheta^2 y^2 \frac{d^2\Psi(y)}{dy^2} + \vartheta^2 y \frac{d\Psi(y)}{dy} \tag{7}$$

Putting Eqs. (6) and (7) into Eq. (5) and after some simplifications, we have:

$$\frac{d^2\Psi(y)}{dy^2} + \frac{1-y}{y(1-y)}\frac{d\Psi(y)}{dy} + \frac{1}{y^2(1-y)^2}\left[-(\varepsilon+\eta_0)y^2 + (2\varepsilon+\eta_0-\eta_1)y - (\varepsilon+\gamma)\right]\Psi(y) = 0, \tag{8}$$

where

$$-\varepsilon = \frac{2\mu E_{nl}}{\vartheta^2\hbar^2}, \quad \eta_0 = \frac{2\mu Z_1}{\vartheta^2\hbar^2} + \frac{2\mu Z_2}{\vartheta\hbar^2}, \quad \eta_1 = \frac{2\mu Z_3}{\hbar^2}, \quad \gamma = l(l+1)\Big\}. \tag{9}$$

Linking Eq. (8) and Eq. (1) of Ref. [58], we have:

$$\tilde{\tau}(y) = 1-y; \quad \sigma(y) = y(1-y); \quad \sigma'(y) = 1-2y, \quad \sigma''(y) = -2; \Big\}$$
$$\tilde{\sigma}(y) = -(\varepsilon+\eta_0)y^2 + (2\varepsilon+\eta_0-\eta_1)y - (\varepsilon+\gamma) \Big\} . \tag{10}$$

Inserting Eq. (10) into Eq. (11) of Ref. [58], gives:

$$\pi(y) = -\frac{y}{2} \pm \sqrt{(B_1-K)y^2 + (K+B_2)y + B_3}, \tag{11}$$

where

$$B_1 = \left(\frac{1}{4} + \varepsilon + \eta_0\right), \quad B_2 = -(2\varepsilon - \eta_0 - \eta_1), \quad B_3 = (\varepsilon + \gamma)\Big\}. \tag{12}$$

We take the discriminant of Eq. (11) under the square root sign and solve for K. Here, for bound state, the negative root is taken as:

$$K = -(B_2 + 2B_3) - 2\sqrt{B_3}\sqrt{B_3 + B_2 + B_1}. \tag{13}$$

Substituting Eq. (13) into Eq. (11), Eq. (14) is gotten as,

$$\pi(y) = -\frac{y}{2} - \left[\left(\sqrt{B_3} + \sqrt{B_3 + B_2 + B_1} \right) y - \sqrt{B_3} \right],$$ (14)

Using Eq. (10) and Eq. (13), we obtain $\tau(y)$ and $\tau'(y)$ as follows:

$$\tau(y) = 1 - 2y - 2\sqrt{B_3}\, y - 2\sqrt{B_3 + B_2 + B_1}\, y + 2\sqrt{B_3},$$ (15)

$$\tau'(y) = -2 \left[1 + \sqrt{B_3} + \sqrt{B_3 + B_2 + B_1} \right],$$ (16)

where $\tau'(y)$ is the first derivative of $\tau(y)$. Referring to Eq. (10) and Eq. (13) of Ref. [58], the following equations for λ_n and λ are as follows:

$$\lambda_n = n^2 + \left[1 + 2\sqrt{B_3} + 2\sqrt{B_3 + B_2 + B_1} \right] n, \quad (n = 0, 1, 2, ...),$$ (17)

$$\lambda = -\frac{1}{2} - \sqrt{B_3} - \sqrt{B_3 + B_2 + B_1} - (B_2 + 2B_3) - 2\sqrt{B_3}\sqrt{B_3 + B_2 + B_1},$$ (18)

When linking Eqs. (17) and (18) with the help of Eq. (9), we obtain the energy equation for the HSKP as:

$$E_{nl} = \frac{\vartheta^2 \hbar^2 l(l+1)}{2\mu} - \frac{\vartheta^2 \hbar^2}{8\mu} \left[\frac{\left(n + \frac{1}{2} + \sqrt{\left(l + \frac{1}{2} \right)^2 + \frac{2\mu D_e r_e^2}{\hbar^2}} \right)^2 - \frac{2\mu Z_1}{\vartheta^2 \hbar^2} + \frac{4\mu D_e r_e}{\hbar^2 \vartheta} + l(l+1)}{n + \frac{1}{2} + \sqrt{\left(l + \frac{1}{2} \right)^2 + \frac{2\mu D_e r_e^2}{\hbar^2}}} \right]^2.$$ (19)

The wave function $\phi(y)$ and weight function $\rho(y)$ is obtain by inserting the values of $\sigma(y)$, $\pi(y)$, and $\tau(y)$ given in Eqs. (10), (14) and (15), respectively, into Eq. (3) and Eq. (9) of Ref. [58] as follows:

$$\phi(y) = y^{\sqrt{B_3}} (1-y)^{\left(\frac{1}{2} + \sqrt{B_3 + B_2 + B_1} \right)},$$ (20)

$$\rho(y) = y^{2\sqrt{B_3}} (1-y)^{2\sqrt{B_3 + B_2 + B_1}}.$$ (21)

Putting Eqs. (10) and (21), into Eq. (2) of Ref. [66], the Rodrigues relation is written as

$$y_n = B_n y^{-2\sqrt{B_3}} (1-y)^{-2\sqrt{B_3 + B_2 + B_1}} \frac{d^n}{dy^n} \left[y^{n+2\sqrt{B_3}} (1-y)^{n+2\sqrt{B_3 + B_2 + B_1}} \right],$$ (22)

where B_n is the Jacobi polynomial. Hereafter, the wave function becomes

$$\psi_{nl}(y) = N_{nl} \, y^{\sqrt{B_3}} (1-y)^{\left(\frac{1}{2} + \sqrt{B_3 + B_2 + B_1} \right)} P_n^{\left(2\sqrt{B_3},\, 2\sqrt{B_3 + B_2 + B_1} \right)} (1-2y),$$ (23)

where N_{nl} is the normalization constant, with the condition, we obtain the normalization constant as follows:

$$\frac{N_{nl}^2}{\vartheta} \int_{-1}^{1} \left(\frac{1-y}{2} \right)^{2\sqrt{B_3}} \left(\frac{1+x}{2} \right)^{\varpi} \left[A_n^{\left(2\sqrt{B_3},\, 2\varpi-1 \right)} (x) \right]^2 dx = 1,$$ (24)

where

$$\left. \begin{array}{l} X = 1 + 2\sqrt{B_3 + B_2 + B_1}, \\ X - 1 = 2\sqrt{B_3 + B_2 + B_1} \end{array} \right\}.$$ (25)

Linking Eq. (26) with the usual integral of the form of Eq. (37) of Ref. [71],

$$\int_{-1}^{1} \left(\frac{1-A}{2} \right)^{u} \left(\frac{1+x}{2} \right)^{v} \left(A_n^{(2u, 2v-1)}(a) \right)^2 dp = \frac{2\Gamma(u+n+1)\Gamma(v+n+1)}{n! u \Gamma(u+v+n+1)}.$$ (26)

Hereafter, the normalization constant is

$$N_{nl} = \left[\frac{n!2\sqrt{B_3}\ \vartheta\ \Gamma\left(2\sqrt{B_3} + 2\sqrt{B_3 + B_2 + B_1} + n + 2\right)}{2\Gamma\left(2\sqrt{B_3} + n + 1\right)\Gamma\left(2\sqrt{B_3 + B_2 + B_1} + n + 2\right)} \right]^{\frac{1}{2}}. \tag{27}$$

THE SOLUTIONS OF THE SE WITH THE HSKP VIA THE SEM

In order to solve the SE with SEM. The SE of the form is considered [30],

$$\frac{d^2U(p)}{dp^2} + \frac{2}{p}\frac{dU(p)}{dp} + \left[\frac{2\mu}{\hbar^2}\left(E_{nl} - V(p)\right) - \frac{l(l+1)}{p^2} \right]U(p) = 0 \tag{28}$$

where l is angular quantum number, μ is the reduced mass, p is the inter-nuclear separation and E_{nl} is the energy eigenvalues.

Next, the Tylor series of the exponential terms in Eq. (1) up to order three is carried out, and then substitute back into Eq.(1), yields:

$$V(p) = -\frac{H_0}{p} + H_1 p + H_2 p^2 + \frac{H_3}{p^2} + H_4 \tag{29}$$

where

$$\left. \begin{array}{l} H_0 = -\dfrac{Z_1}{\vartheta} - Z_2 - \vartheta Z_3, \ H_1 = -\dfrac{Z_1\vartheta}{12} - \dfrac{\vartheta^2 Z_2}{2} - 1.33Z_3\vartheta^2 \\[3mm] H_2 = \dfrac{Z_2\vartheta^3}{6}, \ H_3 = Z_3, \ H_4 = \dfrac{Z_1}{2} + Z_2\vartheta + Z_3\vartheta^2 \end{array} \right\}. \tag{30}$$

By putting Eq. (29) into Eq. (28), we have,

$$\frac{d^2U(p)}{dp^2} + \frac{2}{p}\frac{dU(p)}{dp} + \left[\varepsilon + \frac{\kappa_1}{p} - \kappa_2 p - \kappa_3 p^2 - \frac{T(T+1)}{p^2} \right]U(p) = 0, \tag{31}$$

where

$$\left. \begin{array}{l} \varepsilon = \dfrac{2\mu}{\hbar^2}\left(E_{nl} - H_4\right), \ \kappa_1 = \dfrac{2\mu H_0}{\hbar^2} \\[3mm] \kappa_2 = \dfrac{2\mu H_1}{\hbar^2}, \ \kappa_3 = \dfrac{2\mu H_2}{\hbar^2} \end{array} \right\}, \tag{32}$$

$$T(T+1) = \frac{2\mu H_3}{\hbar^2} + l(l+1). \tag{33}$$

From Eq. (33), we have

$$T = -\frac{1}{2} + \frac{1}{2}\sqrt{(2l+1)^2 + \frac{8\mu H_3}{\hbar^2}} \tag{34}$$

The ansatz wave function is of the form [59],

$$U(p) = e^{-\sigma p^2 - \rho p}S(p), \tag{35}$$

where σ and ρ are constant.
Differentiating Eq. (35), Eqs. (36) and (37) are obtain,

$$U'(p) = S'(p)e^{-\sigma p^2 - \rho p} + S(p)\left(-2\sigma p - \rho\right)e^{-\sigma p^2 - \rho p}, \tag{36}$$

$$\begin{array}{l} U''(p) = S''(p)e^{-\sigma p^2 - \rho p} + S'(p)\left(-2\sigma p - \rho\right)e^{-\sigma p^2 - \rho p} \\[2mm] \qquad + \left[(-2\sigma) + (-2\sigma p - \rho)(-2\sigma p - \rho) \right]S(p)e^{-\sigma p^2 - \rho p} \end{array}. \tag{37}$$

Upon the substitution of Eqs. (35), (36) and (37) into Eq. (31) and subsequent division by $e^{-\sigma p^2 - \rho p}$, Eq. (38) is obtained:

$$S''(p) + \left[-4\sigma p - 2\rho + \frac{2}{p} \right] S'(p) + \left[\begin{array}{l} \left(4\sigma^2 - \kappa_3\right) p^2 + \left(4\sigma\rho - \kappa_2\right) p \\ + \left(\kappa_1 - 2\rho\right) \dfrac{1}{p} - \dfrac{T(T+1)}{p^2} + \left(\varepsilon + \rho^2 - 6\sigma\right) \end{array} \right] S(p) = 0. \tag{38}$$

The function $S(p)$ is considered as a series of the form [59]

$$S(p) = \sum_{n=0}^{\infty} a_n p^{2n+T}. \tag{39}$$

Taking the first and second derivatives of Eq. (39) gives,

$$S'(p) = \sum_{n=0}^{\infty} (2n+T) a_n p^{2n+T-1}. \tag{40}$$

$$S''(p) = \sum_{n=0}^{\infty} (2n+T)(2n+T-1) a_n p^{2n+T-2}. \tag{41}$$

Substituting Eqs. (39), (40) and (41) into Eq. (38), we get

$$\sum_{n=0}^{\infty} (2n+T)(2n+T-1) a_n p^{2n+T-2} + \left[-4\sigma p - 2\rho + \frac{2}{p} \right] \sum_{n=0}^{\infty} (2n+T) a_n p^{2n+T-1}$$

$$+ \left[\left(4\sigma^2 - \kappa_3\right) p^2 + \left(4\sigma\rho - \kappa_2\right) p + \frac{\left(\kappa_1 - 2\rho\right)}{p} - \frac{T(T+1)}{p^2} + \left(\varepsilon + \rho^2 - 6\sigma\right) \right] \sum_{n=0}^{\infty} a_n p^{2n+T} = 0 \tag{42}$$

Collecting powers of p in Eq. (42) gives,

$$\sum_{n=0}^{\infty} a_n \left\{ \begin{array}{l} \left[(2n+T)(2n+T-1) + 2(2n+T) - T(T+1) \right] p^{2n+T-2} \\ + \left[-2\rho(2n+T) + (\kappa_1 - 2\rho) \right] p^{2n+T-1} \\ + \left[-4\sigma(2n+T) + \varepsilon + \rho^2 - 6\sigma \right] p^{2n+T} \\ + \left[4\alpha\beta - \xi_2 \right] r^{2n+L+1} + \left[4\alpha^2 - \xi_3 \right] r^{2n+L+2} \end{array} \right\} = 0. \tag{43}$$

Equation (43) is linearly independent, noting that p is a non-zero function; consequently, it is the coefficient of P that is zero. With this, we have,

$$(2n+T)(2n+T-1) + 2(2n+T) - T(T+1) = 0, \tag{44}$$

$$-2\rho(2n+T) + \kappa_1 - 2\rho = 0, \tag{45}$$

$$-4\sigma(2n+T) + \varepsilon + \rho^2 - 6\sigma = 0, \tag{46}$$

$$4\sigma\rho - \kappa_2 = 0, \tag{47}$$

$$4\sigma^2 - \kappa_3 = 0. \tag{48}$$

From Eqs. (45) and (48) we have

$$\rho = \frac{\kappa_1}{2(2n+T+1)}. \tag{49}$$

$$\sigma = \frac{\sqrt{\kappa_3}}{2}. \tag{50}$$

We proceed to obtaining the energy equation using Eq. (46) and have

$$\varepsilon = 2\sigma(4n+2T+3) - \rho^2. \tag{51}$$

By substituting Eqs. (32), (34), (49) and (34) into Eq. (51) and simplifying we obtain

$$E_{nl} = \sqrt{\frac{\hbar^2 H_2}{2\mu}\left(4n+2+\sqrt{(2l+1)^2+\frac{8\mu H_3}{\hbar^2}}\right) - \frac{2\mu H_0^2}{\hbar^2}\left(4n+1+\sqrt{(2l+1)^2+\frac{8\mu H_3}{\hbar^2}}\right)^{-2} + H_4} \,. \tag{52}$$

Upon substituting Eq. (30) into Eq. (52) we obtain the energy eigenvalues of the HSKP as,

$$E_{nl} = \sqrt{\frac{\hbar^2 D_e r_e \vartheta^3}{6\mu}\left(4n+2+\sqrt{(2l+1)^2+\frac{8\mu D_e r_e^2}{\hbar^2}}\right)}$$
$$-\frac{2\mu}{\hbar^2}\left(-\frac{Z_1}{\vartheta}-2D_e r_e - \vartheta D_e r_e^2\right)^2 \left(4n+1+\sqrt{(2l+1)^2+\frac{8\mu D_e r_e^2}{\hbar^2}}\right)^{-2} + \frac{Z_1}{2} + 2D_e r_e \vartheta + D_e r_e^2 \vartheta^2 \,. \tag{53}$$

Special cases of the HSKP

1. In the case $Z_2 = Z_3 = 0$ we have the HP of Eq. (54) and its energy equation of Eq. (55)

$$V(p) = -\frac{Z_1 e^{-\vartheta p}}{1 - e^{-\vartheta p}} \,, \tag{54}$$

$$E_{nl} = \frac{\vartheta^2 \hbar^2 l(l+1)}{2\mu} - \frac{\vartheta^2 \hbar^2}{8\mu}\left[\frac{(n+l+1)^2 - \frac{2\mu Z_1}{\vartheta^2 \hbar^2} + l(l+1)}{n+l+1}\right]^2 \,. \tag{55}$$

Equation (55) is in agreement with Eq. (32) of [8] and Eq. (37) of [6].

2. By setting $Z_1 = 0$ we have the SKP of Eq. (56) and its energy equation of Eq. (57)

$$V(p) = -\frac{Z_2 e^{-\vartheta p}}{p} + \frac{Z_3 e^{-\vartheta p}}{p^2} \,, \tag{56}$$

$$E_{nl} = \frac{\vartheta^2 \hbar^2 l(l+1)}{2\mu} - \frac{\vartheta^2 \hbar^2}{8\mu}\left[\frac{\left(n+\frac{1}{2}+\sqrt{\left(l+\frac{1}{2}\right)^2+\frac{2\mu D_e r_e^2}{\hbar^2}}\right)^2 + \frac{4\mu D_e r_e}{\hbar^2 \vartheta} + l(l+1)}{n+\frac{1}{2}+\sqrt{\left(l+\frac{1}{2}\right)^2+\frac{2\mu D_e r_e^2}{\hbar^2}}}\right]^2 \,. \tag{57}$$

Equation (57) agrees with Eq. (29) of [53].

3. By setting $Z_1 = \vartheta = 0$ we have the Kratzer potential (KP) of Eq.(58) and its energy equation of Eq. (59)

$$V(p) = -\frac{Z_2}{p} + \frac{Z_3}{p^2} \,, \tag{58}$$

$$E_{nl} = -\frac{2\mu D_e^2 r_e^2}{\hbar^2 \left(n+\frac{1}{2}+\sqrt{\left(l+\frac{1}{2}\right)^2+\frac{2\mu D_e r_e^2}{\hbar^2}}\right)^2} \,. \tag{59}$$

Equation (59) agrees with Eq. (46) of [53];

RESULTS AND DISCUSSION

In the present study, we use Eqs. (19) and (53) to study the energy spectra of four selected diatomic molecules. The spectroscopic parameters of these molecules are given in Table 1 and taken from [62]. We used the following conversions factors: $\hbar c = 1973.29$ eV Å and $1\,amu$ $931.5 \times 10^6 eV(\overset{\circ}{A})^{-1}$ for all computations [62]. The numerical computation of the energy eigenvalues of the HSKP for HCl, LiH, H_2 and NO DMs are given in Tables 2 and 3. It is observed that for each vibrational quantum number, the energy increase with increase in the rotational quantum number, for each of the selected DMs. To validate our results, we deduce Kratzer and screened Kratzer potentials from the proposed potential to compute the energy spectra for HCl and LiH DMs. It is seen that our results are in excellent agreement with the report of

Ref. [30] and Ref. [53] as shown in Tables 4 and 5. We plotted the energy eigenvalues of HSKP for selected molecules with different rotational quantum number (RQN). The plot of the energy eigenvalues of HCl and NO with different values of l is shown in Fig. 1 and Fig. 2. It depicts a monotonic decrease as the principal quantum number increases and all converges together.

Table 1. Spectroscopic parameters of selected DMs [62]

Molecules	$D_e(eV)$	$\alpha = \vartheta\left(\overset{\circ}{A}^{-1}\right)$	$r_e\left(\mathring{A}\right)$	$\mu(MeV)$
HCl	4.6190309050	1.86770	1.2746	0.09129614886
LiH	2.5152672118	1.12800	1.5956	0.08198284801
H_2	4.7446000000	1.94260	0.7416	0.05021684305
NO	8.0437300000	1.86430	1.1508	5.91053826200

Table 2. Bound state energy spectra $E_{nl}(eV)$ of HSKP for HCl, LiH, H_2 and NO DMs with the NU method

n	l	E_{nl}(eV) of HCl	E_{nl}(eV) of LiH	E_{nl}(eV) of H_2	E_{nl}(eV) of NO
0	0	-22.17032494	-9.044861721	-13.92974441	-34.53518839
0	1	-22.17022128	-9.044847651	-13.93464244	-34.53518812
0	2	-22.17001432	-9.044819582	-13.94456401	-34.53518756
0	3	-22.16970474	-9.044777634	-13.94456401	-34.53518674
0	4	-22.16929354	-9.044722014	-13.98060726	-34.53518565
0	5	-22.16878209	-9.044652964	-13.98060745	-34.53518429
1	0	-22.24690799	-9.033844252	-13.79739618	-34.53969898
1	1	-22.24679078	-9.033836790	-13.80084636	-34.53969869
1	2	-22.24655670	-9.033821914	-13.80786295	-34.53969812
1	3	-22.24620649	-9.033799708	-13.81867833	-34.53969726
1	4	-22.24574126	-9.033770284	-13.83364106	-34.53969611
1	5	-22.24516244	-9.033733821	-13.85321597	-34.53969468
2	0	-22.33432382	-9.029306244	-13.70661022	-34.54441426
2	1	-22.33419477	-9.029304880	-13.70872277	-34.54441398
2	2	-22.33393705	-9.029302176	-13.71305549	-34.54441337
2	3	-22.33355145	-9.029298171	-13.71982357	-34.54441248
2	4	-22.33303911	-9.029292928	-13.72934979	-34.54441128
2	5	-22.33240157	-9.029286529	-13.74206457	-34.54440980
3	0	-22.43212310	-9.030892408	-13.65662021	-34.54933324
3	1	-22.43198398	-9.030896786	-13.65749846	-34.5433292
3	2	-22.43198398	-9.030905540	-13.65935463	-34.54933232
3	3	-22.43129039	-9.030918685	-13.66238806	-34.54933137
3	4	-22.43073793	-9.030936216	-13.66689774	-34.54933014
3	5	-22.43005037	-9.030958150	-13.67328236	-34.54932858
4	0	-22.53989148	-9.038278642	-13.64667365	-34.54932858
4	1	-22.53974404	-9.038288540	-13.64641418	-34.55445454
4	2	-22.53944960	-9.038308324	-13.64598762	-34.55445388
4	3	-22.53900894	-9.038337960	-13.64557866	-34.55445292
4	4	-22.53842333	-9.038377402	-13.64546438	-34.5544162
4	5	-22.53769441	-9.038426596	-13.64601419	-34.55445003

Table 3. Bound state energy spectra $E_{nl}(eV)$ of HSKP for HCl, LiH LiH, H_2 and NO DMs with the S,EM

n	l	E_{nl}(eV) of HCl	E_{nl}(eV) of LiH	E_{nl}(eV) of H_2	E_{nl}(eV) of NO
0	0	-22.17032454	-9.044861731	-13.92974451	-34.53518830
0	1	-22.17022118	-9.044847641	-13.93464234	-34.53518813
0	2	-22.17001422	-9.044819562	-13.94456411	-34.53518757
0	3	-22.16970464	-9.044777654	-13.94456411	-34.53518674
0	4	-22.16929344	-9.044722034	-13.98060736	-34.53518566
0	5	-22.16878219	-9.044652954	-13.98060725	-34.53518420
1	0	-22.24690789	-9.033844242	-13.79739638	-34.53969899
1	1	-22.24679018	-9.033836760	-13.80084646	-34.53969865
1	2	-22.24655660	-9.033821954	-13.80786285	-34.53969813
1	3	-22.24620659	-9.033799718	-13.81867843	-34.53969726
1	4	-22.24574136	-9.033770264	-13.83364116	-34.53969612
1	5	-22.24516234	-9.033733831	-13.85321587	-34.53969469
2	0	-22.33432372	-9.029306254	-13.70661032	-34.54441427
2	1	-22.33419467	-9.029304830	-13.70872287	-34.54441399
2	2	-22.33393704	-9.029302156	-13.71305559	-34.54441338
2	3	-22.33355135	-9.029298181	-13.71982367	-34.54441249

n	l	$E_{nl}(\text{eV})$ of HCl	$E_{nl}(\text{eV})$ of LiH	$E_{nl}(\text{eV})$ of H$_2$	$E_{nl}(\text{eV})$ of NO
2	4	-22.33303921	-9.029292928	-13.72934989	-34.54441129
2	5	-22.33240117	-9.029286539	-13.74206467	-34.54440981
3	0	-22.43212300	-9.030892418	-13.65662031	-34.54933325
3	1	-22.43198318	-9.030896796	-13.65749856	-34.54332920
3	2	-22.43198328	-9.030905443	-13.65935443	-34.54933233
3	3	-22.43129039	-9.030918675	-13.66238816	-34.54933138
3	4	-22.43073743	-9.030936226	-13.66689784	-34.54933015
3	5	-22.43005027	-9.030958110	-13.67328246	-34.54932859
4	0	-22.53989138	-9.038278642	-13.64667375	-34.54932859
4	1	-22.53974414	-9.038288550	-13.64641428	-34.55445455
4	2	-22.53944950	-9.038308344	-13.64598772	-34.55445389
4	3	-22.53900884	-9.038337930	-13.64557886	-34.55445293
4	4	-22.53842323	-9.038377412	-13.64546408	-34.55441620
4	5	-22.53769451	-9.038426586	-13.64601429	-34.55445000

Table 4. Assessment of the Energy eigenvalues $E_{nl}(eV)$ of the KP for HCl and LiH

n	l	Present work for energy (eV) of HCl	Energy (eV) of HCl Ref. [38]	Energy (eV) of HCl Ref. [60]	Present work for energy (eV) of LiH	Energy (eV) of LiH Ref. [38]	Energy (eV) of LiH Ref. [60]
0	0	-4.54184821	-4.574322886	-4.541847882	-2.46731030	-2.467293680	-2.467293778
1	0	-4.39372795	-4.402122552	-4.393727024	-2.37581921	-2.380989203	-2.375802636
	1	-4.39129385	-4.401308521	-4.391292904	-2.37410797	-2.380416619	-2.374091378
2	0	-4.25273711	-4.239466022	-4.252735636	-2.28932426	-2.281213703	-2.289307674
	1	-4.25041920	-4.238696688	-4.250417718	-2.28770560	-2.280676728	-2.287688996
	2	-4.24579105	-4.237158875	-4.245789526	-2.28447521	-2.279603547	-2.284458584
3	0	-4.11842537	-4.085660853	-4.118423404	-2.20746820	-2.187580925	-2.207451626
	1	-4.11621638	-4.084933001	-4.116214408	-2.20593555	-2.187076666	-2.205918968
	2	-4.11180563	-4.083478096	-4.111803616	-2.20287674	-2.186068862	-2.202860140
	3	-4.10520744	-4.081297704	-4.105205380	-2.19830467	-2.184558925	-2.198288040
4	0	-3.99037742	-3.940076275	-3.990375014	-2.12992512	-2.099596786	-2.129908602
	1	-3.98827064	-3.939386976	-3.988268222	-2.12847251	-2.099122640	-2.128455976
	2	-3.98406387	-3.938009125	-3.984061424	-2.12557335	-2.098175007	-2.125556792
	3	-3.97777065	-3.935944185	-3.977768152	-2.12123970	-2.096755197	-2.121223116
	4	-3.96941113	-3.933194375	-3.969408570	-2.11548950	-2.094865172	-2.115472884
5	0	-3.86820974	-3.802136724	-3.868206938	-2.05639728	-2.016815899	-2.056380834
	1	-3.86619896	-3.801483303	-3.866196140	-2.05501922	-2.016369515	-2.055002762
	2	-3.86218380	-3.800177161	-3.862180950	-2.05226878	-2.015477357	-2.052252304
	3	-3.85617703	-3.798219664	-3.856174134	-2.04815726	-2.014140642	-2.048140758
	4	-3.84819767	-3.795612890	-3.848194720	-2.04270146	-2.012361189	-2.042684928
	5	-3.83827087	-3.792359570	-3.838267840	-2.03592352	-2.010141421	-2.035906942

Table 5. Assessment of the Energy eigenvalues $E_{nl}(eV)$ of the SKP for HCl and LIH

n	l	Present work for energy of $E_{nl}(eV)$ LiH	Present work for energy of $E_{nl}(eV)$ HCl	Energy (eV) of LiH Ref. [60]	Energy (eV) of HCl Ref. [60]
0	0	-9.070968134	-22.19329052	-9.070968135	-22.19329052
1	0	-9.059446115	-22.26953722	-9.059446120	-22.26953722
	1	-9.047056120	-22.24266011	-9.047056120	-22.24266011
2	0	-9.054431116	-22.35663288	-9.054431115	-22.35663288
	1	-9.042278085	-22.33012521	-9.042278085	-22.33012521
	2	-9.017997940	-22.27714784	-9.017997940	-22.27714784
3	0	-9.055565865	-22.45412720	-9.055565865	-22.45412720
	1	-9.043637070	-22.42797265	-9.043637070	-22.42797265
	2	-9.019803985	-22.37569979	-9.019803985	-22.37569979
	3	-8.984115355	-22.29738072	-8.984115355	-22.29738072
4	0	-9.062524470	-22.56160484	-9.062524470	-22.56160484
	1	-9.050808170	-22.53578825	-9.050808170	-22.53578825
	2	-9.027398770	-22.48418965	-9.027398770	-22.48418965
	3	-8.992342455	-22.40687787	-8.992342455	-22.40687787
	4	-8.945707875	-22.30395550	-8.945707875	-22.30395550
5	0	-9.075009170	-22.67868230	-9.075009170	-22.67868230
	1	-9.063494530	-22.65318950	-9.063494530	-22.65318950
	2	-9.040487255	-22.60223694	-9.040487255	-22.60223694
	3	-9.006031120	-22.52589037	-9.006031120	-22.52589037
	4	-8.960191210	-22.42424781	-8.960191210	-22.42424781
	5	-8.903053285	-22.29743871	-8.903053285	-22.29743871
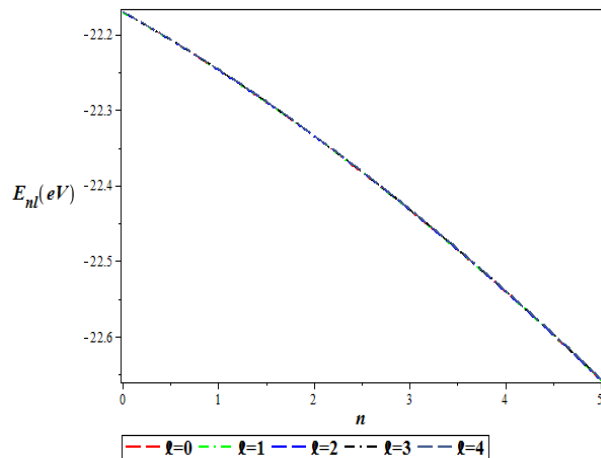
Figure 1. The plot of the energy spectra for various l versus n for HCl Diatomic molecules
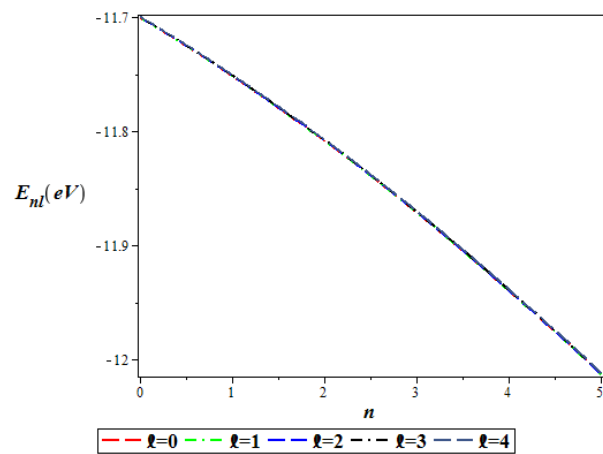
Figure 2. The plot of the energy spectra for various l versus n for NO Diatomic molecules

CONCLUSION

In this research, we solved the SE with the HSKP using the NU and series expansion methods. The energy equation and the normalized wave function were obtained. We then applied the energy equation to study four DMs. The results show that the energy spectra of these DMs increase as various quantum numbers n and l increase. To test the accuracy of our results, we computed the bound state energy of two DMs for KP and SKP, which were found to agree with the report of other researchers. Variation of the energies with respect to principal quantum number was plotted.

ORCID IDs
Etido P. Inyang, https://orcid.org/0000-0002-5031-3297; **Joseph Ntibi,** https://orcid.org/0000-0002-7908-2840

REFERENCES

[1] E.P. Inyang, J.E. Ntibi, E.A. Ibanga, F. Ayedun, E.P. Inyang, E.E. Ibekwe, E.S. William, and I.O. Akpan, "Thermodynamic properties and mass spectra of a quarkonium system with Ultra Generalized Exponential- Hyperbolic potential", Communication in Physical Science, **7**, 97 **(**2021), https://journalcps.com/index.php/volumes/article/download/196/172

[2] H. Mutuk, "Mass Spectra and Decay constants of Heavy-light Mesons: A case study of QCD sum Rules and Quark model", Advances in High Energy Physics, **20**, 8095653 (2018), https://doi.org/10.1155/2018/8095653

[3] M. Allosh, Y. Mustafa, N.K. Ahmed, and A.S. Mustafa, "Ground and Excited state mass spectra and properties of heavy-light mesons", Few-Body System, **62**, 26 (2021), https://doi.org/10.1007/s00601-021-01608-1

[4] M. Abu-Shady, C.O. Edet, and A.N. Ikot, "Non-relativistic Quark model under external magnetic and Aharanov-Bohm (AB) fields in the presence of Temperature-Dependent confined Cornell potential", Canadian Journal of Physics, **99**(11), (2021) https://doi.org/10.11139/cjp-2020-0101

[5] U.S. Okorie, C.O. Edet, A.N. Ikot, G.J. Rampho, and R. Sever, "Thermodynamic function for diatomic molecules with modified Kratzer plus screened Coulomb potential", Indian Journal Physics, **159**, 411 (2020), https://doi.org/10.1007/s12648-019-01670-w

[6] I.B. Okon, and O. Popoola, "Bound-State solution of Schrodinger equation with Hulthen plus generalized exponential Coulomb potential using Nikiforov-Uvarov method", International Journal of Recent Advances in Physics, **4**(3), 1 (2015), http://dx.doi.org/10.14810/ijrap.2015.4301

[7] C.A. Onate, M.C. Onyeaju, E. Omugbe, I.B. Okon, and O.E. Osafile, "Bound-state solutions and thermal properties of the modifed Tietz–Hua potential", Scientific Report, **11**, 2129 (2021), https://doi.org/10.1038/s41598-021-81428-9

[8] O. Bayrak, G. Kocak, and I. Boztosun, "Any l-state solutions of the Hulth´en potential by the asymptotic iteration method", Journal of Physics A, **39**, 11521 (2006), https://doi.org/10.1088/0305-4470/39/37/012

[9] P. Aspoukeh, and S.M. Hamad, "Bound state solution of the Klein-Gordon equation for vector and scalar Hellmann plus modified Kratzer potentials", Chinese Journal of Physics, **68**, 224 (2020), https://doi.org/10.1016/j.cjph.2020.09.002

[10] C.O. Edet, and P.O. Okoi, "Any l-state solutions of the Schrodinger equation for q-deformed Hulthen plus generalized inverse quadratic Yukawa potential in arbitrary dimensions", Revista Mexicana De Fisica, **65**, 333 (2019), https://doi.org/10.31349/RevMexFis.65.333

[11] R. Rani, S. B. Bhardwaj, and F. Chand, "Mass spectra of heavy and light mesons using asymptotic iteration method", Communication of Theoretical Physics **70**, 179 (2018), https://doi.org/10.1088/0253-6102/70/2/179

[12] H. Ciftci, and H.F. Kisoglu, "Non-relativistic Arbitary l -states of Quarkonium through Asymptotic interation method", Pramana Journal of Physics, **56**, 467 (2018), https://doi.org/10.1155/2018/4549705

[13] M. Abu-Shady, and E.M. Khokha, "Heavy-Light mesons in the non-relativistic Quark model using Laplace Transformation method with the Generalized Cornell potential", Advances in High Energy Physics. **12**, 345 (2018), https://doi.org/10.1155/2018/7032041

[14] M. Abu-Shady, T.A. Abdel-Karim, and E.M. Khokha, "Exact solution of the N-dimensional Radial Schrödinger Equation via Laplace Transformation method with the Generalized Cornell potential", Journal of Quantum Physics, **45**, 587 (2018), https://doi.org/10.48550/arXiv.1802.02092

[15] M. Abu-Shady, and A.N. Ikot, "Analytic solution of multi-dimensional Schrödinger equation in hot and dense QCD media using the SUSYQM method", The European Physical Journal Plus, **134,** 321 (2019), https://doi.org/10.1140/epjp/i2019-12685-y

[16] J.E. Ntibi, E.P. Inyang, E.P. Inyang, and E.S. William, "Relativistic Treatment of D-Dimensional Klien-Gordon equation with Yukawa potential", International Journal Innovative Science and Engineering, **7**(11), (2020), http://ijiset.com/vol7/v7s11/IJISET_V7_I11_04.pdf

[17] E.S. William, J.A. Obu, I.O. Akpan, E.A. Thompson, and E.P. Inyang, "Analytical Investigation of the Single-particle energy spectrum in Magic Nuclei of ^{56}Ni and ^{116}Sn. European Journal of Applied Physics, **2**, 28 (2020). http://dx.doi.org/10.24018/ejphysics.2020.2.6.28

[18] E.P. Inyang, E.S. William, and J.A. Obu, "Eigensolutions of the N-dimensional Schrödinger equation` interacting with Varshni-Hulthen potential model", Revista Mexicana De Fisica, **67**, 193 (2021). https://doi.org/10.31349/RevMexFis.67.193

[19] C.O. Edet, P.O. Okoi, A.S. Yusuf, P.O. Ushie, and P.O. Amadi, "Bound state solutions of the generalized shifted Hulthen potential". Indian Journal of physics, **95**, 471 (2020), https://doi.org/10.1007/s12648-019-01650-0

[20] E.P. Inyang, J. E. Ntibi, E.P. Inyang, E.S. William, and C.C. Ekechukwu, "Any L-state solutions of the Schrödinger equation interacting with class of Yukawa-Eckart potentials", International Journal of Innovative Science, Engineering & Technology, **11**(7), 2432 (2020), http://ijiset.com/vol7/v7s11/IJISET_V7_I11_05.pdf

[21] E.P. Inyang, J.E. Ntibi, E.P. Inyang, F. Ayedun, E.A. Ibanga, E.E. Ibekwe, and E.S. William, "Applicability of Varshni potential to predict the mass spectra of heavy mesons and its thermodynamic properties", Applied Journal of Physical Science, **3**, 92 (2021), https://integrityresjournals.org/journal/AJPS/article-full-text-pdf/7CDCA96D1

[22] C.O. Edet, P.O. Amadi, M.C. Onyeaju, U.S. Okorie, R. Sever, and G.J. Rampho, "Thermal properties and magnetic susceptibility of Hellmann potential in Aharonov-Bohm (AB) Flux and magnetic fields at Zero and Finite temperature", Journal of Low Temperature Physics, **202**, 83 (2021), https://doi.org/10.1007/s10909-020-02533-z

[23] I.O. Akpan, E.P. Inyang, E.P. Inyang, and E.S. William, "Approximate solutions of the Schrödinger equation with Hulthen-Hellmann Potentials for a Quarkonium system", Revista Mexica De Fisica, **67**(3), 482 (2021), https://doi.org/10.31349/RevMexFis.67.482

[24] E.S. William, E.P. Inyang, and E.A. Thompson, "Arbitrary ℓ - solutions of the Schrödinger equation interacting with Hulthén-Hellmann potential model", Revista Mexicana Fisica, **66**, 730 (2020), https://doi.org/10.31349/RevMexFis.66.730

[25] E.P. Inyang, B.I. Ita, and E.P. Inyang, "Relativistic treatment of Quantum mechanical Gravitational-Harmonic Oscillator potential". European Journal of Applied Physics, **3**(3), 42 (2021), https://dx.doi.org/10.24018/ejphysics.2021.3.3.83

[26] M. Abu-Shady, T.A. Abdel-Karim, and Y. Ezz-Alarab, "Masses and thermodynamic properties of heavy mesons in the non-relativistic quark model using the Nikiforov-Uvarov method", Journal of Egyptian Mathematical Society, **23**, 155 (2019), https://doi.org/10.1186/s42787-019-0014-0

[27] E.P. Inyang, E.P. Inyang, J.E. Ntibi, E.E. Ibekwe, and E.S. William, **"**Approximate solutions of D-dimensional Klein-Gordon equation with Yukawa potential via Nikiforov-Uvarov method", Indian Journal of Physics, **95**, 2733 (2021), https://doi.org/10.1007/s12648-020-01933-x

[28] G.J. Rampho, A.N. Ikot, C.O. Edet, and U.S. Okorie, "Energy spectra and thermal properties of diatomic molecules in the presence of magnatic and AB fields with improved Kratzer potential", Molecular Physics, **17** (2020), http://dx.doi.org/10.1080/00268976.2020.1821922

[29] A.N. Ikot, U.S. Okorie, P.O. Amadi, C.O. Edet, G.J. Rampho, and R. Sever, "The Nikiforov-Uvarov –Functional Analysis (NUFA) Method: A new approach for solving exponential – Type potentials", Few-Body System, **62**, 9 (2021), https://doi.org/10.1007/s00601-021-021-01593-5

[30] E.E. Ibekwe, U.S. Okorie, J.B. Emah, E.P. Inyang, and S.A. Ekong, "Mass spectrum of heavy quarkonium for screened Kratzer potential (SKP) using series expansion method", European Physics Journal Plus, **87**, 136 (2021), https://doi.org/10.1140/epjp/s13360-021-01090-y

[31] E.P. Inyang, E.P. Inyang, I.O. Akpan, J.E. Ntibi, and E.S. William, "Analytical solutions of the Schrödinger equation with class of Yukawa potential for a quarkonium system via series expansion method", European Journal of Applied Physics, **2**, 26 (2020), http://dx.doi.org/10.24018/ejphysics.2020.2.6.26

[32] E.E. Ibekwe, A.T. Ngiangia, U.S. Okorie, A.N. Ikot, and H.Y. Abdullah, A.N. Ikot, and N.Y. Abdullah, "Bound state solution of radial Schrödinger equation for the quark-antiquark interaction potential", Iran Journal of Science and Technology, **44**, 1191 (2020), https://doi.org/10.1007/s40995-020-00913-4

[33] E.P. Inyang, E.P. Inyang, J. Kamiliyus, J.E. Ntibi, and E.S. William, Diatomic molecules and mass spectrum of Heavy Quarkonium system with Kratzer-screened Coulomb potential (KSCP) through the solutions of the Schrodinger equation. European Journal of Applied Physics, **3**, 55 (2021), https://doi.org/10.24018/ejphysics.2021.3.2.61

[34] M. Abu-Shady, and H.M. Fath-Allah, "The effect of extended Cornell potential on heavy and heavy-light meson masses using series method", Journal of the Egyptian mathematical society, **23**, 156 (2019), https://arXiv:1908.09131

[35] E.M. Khokha, M. Abushady, and T.A. Abdel-Karim, "Quarkonium masses in the N-dimensional space using the Analytical Exact Iteration method", International Journal of Theoretical and Applied. Mathematics, **2**, 86 (2016), http://article.sciencepublishinggroup.com/pdf/10.11648.j.ijtam.20160202.19.pdf

[36] E. Omugbe, O.E. Osafile, M.C. Onyeajh, "Mass spectrum of mesons via WKB Approximation method". Advances in High Energy Physics, **10**, 1143 (2020), https://doi.org/10.1155/2020/5901464

[37] E. Omugbe, O.E. Osafile, E.P. Inyang, and A. Jahanshir, "Bound state solutions of the hyper-radial Klein-Gordon equation under the Deng-Fan potential by WKB and SWKB methods", Physica Scripta, **96**, 125408 (2021), https://doi.org/10.1088/1402-4896/ac38d4

[38] E. Omugbe, O.E. Osafile, I.B. Okon, E.P. Inyang, E.S. William, and A. Jahanshir, "Any L-state energy of the spinless Salpeter equation under the Cornell potential by the WKB Approximation method: An Application to mass spectra of mesons", Few-Body Systems **63**, 6 (2022), https://link.springer.com/article/10.1007%2Fs00601-021-01705-1

[39] E. Omugbe, "Approximate non-relativistic energy expression and the rotational-vibrational constants of the Tietz-Hua potential: A semi classical approach", Canadian Journal of Chemistry, **98**, 683 (2020), https://doi.org/10.1139/cjc-2020-0140

[40] E. Omugbe, "Non-relativistic energy spectrum of the Deng-Fan Oscillator via the WKB Approximation method", Asian Journal of Physical and Chemical Sciences, **8**(1), 26 (2020), https://doi.org/10.9734/ajopacs/2020/v8i130107

[41] L. Hitler, B.I .Ita, N. Nzeata-Ibe, I. Joseph, O. Ivan, T, and O. Magu, "WKB Solutions for Inversely Quadratic Yukawa plus Inversely Quadratic Hellmann Potential, World Journal of Applied Physics, **2**(4), 109 (2017), https://article.sciencepublishinggroup.com/pdf/10.11648.j.wjap.20170204.13.pdf

[42] M.S. Ali, G.S. Hassan, A.M. Abdelmonem, S.K. Elshamndy, F. Elmasry, and A.M. Yasser, "The spectrum of charmed quarkonium in non-relativistic quark model using matrix Numerov's method", J. Rad. Research and Applied Sciences, **13**, 233 (2020), https://doi.org/10.1080/16878507.2020.1723949

[43] H. Mutuk, "Cornell potential: A Neural Network approach", Advances in High Energy Physics, **2019**, 3105373 (2019), https://doi.org/10.1155/2019/3105373

[44] I.B.Okon, O.O. Popoola, E. Omugbe, A.D. Antia, C.N. Isonguyo, and E.E. Ituen, "Thermodynamic properties and Bound state solutions of Schrodinger equation with Mobius square plus screened-Kratzer potential using Nikiforov-Uvarov method", Computational and Theoretical Chemistry, **1196**, 113132 (2020) https://doi.org/10.1016/j.comptc.2020.113132

[45] C.O. Edet, U.S. Okorie, A.T. Ngiangia, and A.N. Ikot, "Bound state solutions of the Schrödinger equation for the modified Kratzer plus screened Coulomb potential". Indian Journal of Physics, **94**, 425 (2019), https://doi.org/10.1007/s12648-019-01477-9

[46] P. Nwabuzor, C. Edet, A. Ndemikot, U. Okorie, M. Ramantswana, R. Horchani, A. Abdel-Aty, and G. Rampho, "Analyzing the effects of Topological defect(TD) on the Energy Spectra and Thermal Properties of LiH,TiC and I_2 Diatomic molecules". Entropy **23**, 1060 (2021). https://doi.org/10.3390/e23081060

[47] E.P. Inyang, E.S. William, J.O. Obu, B.I. Ita, E.P. Inyang, and I.O. Akpan, "Energy spectra and expectation values of selected diatomic molecules through the solutions of Klein-Gordon equation with Eckart-Hellmann potential model", Molecular Physics. **119**, e1956615 (2021), https://doi.org/10.1080/00268976.2021.1956615

[48] U.P. Obogo, O.E. Ubi, C.O. Edet, and A.N. Ikot, "Effect of the deformation parameter on the nonrelativistic energy spectra of the q-deformed Hulthen-quadratic exponential-type potential", Ecletica Quimica Journal, **46**, 73 (2021), https://doi.org/10.26850/1678-4618eqj.v46.4.2021.p60-73

[49] C.O. Edet, and A.N. Ikot, "Superstatistics of Diatomic molecules with the shifted Deng-Fan potential model", Biointerface Research in Applied Chemistry, **12**(3), (2022) 4139, https://doi.org/10.33263/BRIAC123.41264139

[50] C.O. Edet, U.S. Okorie, G. Osobonye, A.N. Ikot, G.J. Rampho, and R. Sever, "Thermal properties of Deng-Fan-Eckart potential model using Poisson summation approach", Journal Mathematical Chemistry, **12**, 25 (2020), https://doi.org/10.1007/s10910-020-01107-4

[51] L. Hulthen, "Über die eigenlosunger der Schrödinger-Gleichung des deuterons", Ark. Mat. Astron. Fys. A, **28**, 5 (1942).

[52] I.B. Okon, E. Omugbe, A.D. Antia, C.A. Onate, L.E. Akpabio, and O.E. Osafile, "Spin and pseudospin solutions to Dirac equation and its thermodynamic properties using hyperbolic Hulthen plus hyperbolic exponential inversely quadratic potential", Scientific Reports, **11**, 892 (2021), https://doi.org/10.1038/s41598-020-77756-x

[53] A.N. Ikot, U.S. Okorie, R. Sever, and G.J. Rampho. "Eigensolution, expectation values and thermodynamic properties of the screened Kratzer potential", European Physical Journal Plus, **134**, 386 (2019), https://doi.org/10.1140/epjp/i2019-12783-x

[54] A.N. Ikot, C.O. Edet, P.O. Amadi, U.S. Okorie, G.J. Rampho, and H.Y. Abdullah, "Thermodynamic properties of Aharanov-Bohm (AB) and magnetic fields with screened Kratzer potential", European Physical Journal D, **74**, 159 (2020), https://doi.org/10.1140/epjd/e2020-10084-9

[55] A.N. Ikot, U.S. Okorie, A.T. Ngiangia, C.A. Onate, C.O. Edet, I.O. Akpan, and P.O. Amadi, "Bound state solutions of the Schrodinger equation with energy-dependent molecular Kratzer potential via asymptotic iteration method", Ecletica Quimica Journal, **45**(1), 45 (2020), https://doi.org/10.26850/1678-4618eqj.v45.1.2020.p65-77

[56] C.O. Edet, A.N. Ikot, M.C. Onyeaju, U.S. Okorie, G.J. Rampho, M.L. Lekala, and S. Kaya. "Thermo-magnetic properties of the screened Kratzer potential with spatially varying mass under the influence of Aharanov-Bohm (AB) and position-dependent magnetic fields", Physica E: Low-dimensional System and nanostructures. **131**, 114710 (2021), https://doi.org/10.1016/j.physe.2021.114710

[57] E.P. Inyang, E.P. Inyang, I.O. Akpan, J.E. Ntibi, and E.S. William, "Masses and thermodynamic properties of a Quarkonium system", Canadian Journal Physics, **99**(11), 990 (2021), https://doi.org/10.1139/cjp-2020-0578

[58] S.K. Nikiforov, and V.B. Uvarov, *Special functions of Mathematical Physics*, (Birkhauser, Basel, 1988)

[59] R. Rani, S.B. Bhardwaj, and F. Chand, "Bound state solutions to the Schrodinger equation for some diatomic molecules" Pramana-Journal of Physical, **91**, 46 (2018), https://doi.org/10.1007/s12043-018-1622-1

[60] E.P. Inyang, E.P. Inyang, E.S. William, and E.E. Ibekwe, "Study on the applicability of Varshni potential to predict the mass-spectra of the Quark-Antiquark systems in a non-relativistic framework", https://arxiv.org/abs/2101.00333

[61] R.L. Greene, and C. Aldrich, "Variational wave functions for a screened Coulomb potential", Physical Review A, **14** (1976) 2363, https://doi.org/10.1103/PhysRevA.14.2363

[62] O.J. Oluwadere, and K.J. Oyewumi, "Energy spectra and the expectation values of diatomic molecules confined by the shifted Deng-Fan potential", European Physical Journal plus, **133**, 422 (2018), https://doi.org/10.1140/epjp/i2018-12210-0

РОЗВ'ЯЗАННЯ РІВНЯННЯ ШРЕДІНГЕРА З ХУЛЬТЕН-ЕКРАНОВАНИМ КРАТЦЕР ПОТЕНЦІАЛОМ: ЗАСТОСУВАННЯ ДО ДВОХАТОМНИХ МОЛЕКУЛ

Етідо П. Ін'янг[a,b], П.С. Івуджі[b], Йозеф Е. Нтібі[b], Е.С. Вільям[b], Є.А. Ібанга[a]
[a]Фізичний факультет, Національний відкритий університет Нігерії, Джабі, Абуджа, Нігерія
[b]Група теоретичної фізики, факультет фізики, Університет Калабар, Калабар, Р.М.В 1115, Нігерія

У цьому дослідженні рівняння Шредінгера з екранованими потенціалами Хультена-плюс екрановані потенціали Кратцера (HSKP) розв'язуються за допомогою методів Нікіфорова-Уварова (НУ) і розкладання в ряд. Методом NU отримано рівняння енергії та хвильова функція в закритому вигляді з наближенням Гріна-Олдріча. Метод розкладання в ряд також був використаний для отримання рівняння енергії HSKP. З об'єднаних потенціалів було отримано три різні випадки. Для різних квантових станів розраховано власні значення енергії HSKP для HCl, LiH, H_2, і NO двоатомних молекул. Щоб перевірити

точність наших результатів, ми обчислили енергію зв'язаних станів HCl і LiH, для окремого випадку потенціалу Кратцера та екранованого потенціалу Кратцера, які чудово узгоджуються з результатами інших дослідників.

Ключові слова: рівняння Шредінгера; метод Нікіфорова-Уварова; метод розширення рядів; потенціал Кратцера плюс екранований Hulthén потенціал; двоатомні молекули

GENERAL ANALYSIS OF THE REACTION $e^+ + e^- \to N + \bar{N} + \pi^0$ †

Gennadiy I. Gakh[a], Mykhailo I. Konchatnij[a]*, Nikolay P. Merenkov[a], Egle Tomasi-Gustafsson[b]

[a]NSC "Kharkiv Institute of Physics and Technology"
Akademicheskaya, 1, 61108, Kharkiv, Ukraine
[b]IRFU, CEA, Université Paris-Saclay, 91191 Gif-sur-Yvette, France
*Corresponding Author: konchatnij@gmail.com

The general analysis of the reaction $e^+ + e^- \to N + \bar{N} + \pi^0$, in the case of longitudinally polarized electron beam, has been performed in the one-photon-annihilation approximation, accounting for the polarization states of the final nucleon. This analysis is useful for the description of the continuum (non-resonant) and resonant (with different possible vector mesons or excited baryons in the intermediate virtual states of the Feynman diagrams) contributions. The conservation of the hadron electromagnetic currents and P-invariance of the hadron electromagnetic interaction were used to express the matrix element in terms of the six complex independent invariant amplitudes. The general structure of the hadronic tensor for the case of unpolarized final hadrons and polarized nucleon has been derived. The spin-independent part of the hadronic tensor is determined by five structure functions and the spin-dependent one by 13 structure functions. The transversal, longitudinal and normal components of the nucleon polarization four-vector are expressed by means of the four-vectors of the particle momenta. The five independent invariant variables which describe the reaction have been introduced. The limits of the changing of these variables have been considered. The kinematical double invariant variables regions are given in the figure. The kinematics, suitable to study the invariant mass distributions, is investigated.
Keywords: polarization phenomena, electron, invariant amplitudes, hadronic tensor, kinematics
PACS: 12.20.-m, 13.40.-f, 13.60.-Hb, 13.88.+e

About 20 years ago, the BES started a baryon resonance program [1] at Beijing Electron-Positron Collider (BEPC) [2,3]. The major experimental results on N^* resonances from e^+e^- annihilations for last 20 years and some of their interesting phenomenological implications are reviewed in [1].

The measurements of time-like region electromagnetic form factors of hadrons can be done in the electron-positron annihilation process, which provides a key to understanding quantum chromodynamics effects in bound states. For example, there is great progress in the study of baryon electromagnetic form factors in the time like regions, both on the experimental [4–6] and theoretical sides [7–9]. The measurement of the e^+e^- reactions permits to study also the excited hyperon states, such as Λ^*, Σ^* and Ξ^* [10,12]. Up to now, the N^* production from e^+e^- annihilations has been studied only around charmonium region.

The reaction $e^+ + e^- \to p + \bar{p} + \pi^0$, where N^* resonances can manifest themselves as intermediate states of corresponding Feynman diagrams, was measured with BESIII detector at the BEPCII collider. In the experiment [13], this reaction has been studied in the vicinity of the $\psi(3770)$ resonance. The Born cross section of $e^+ + e^- \to \psi(3770) \to p + \bar{p} + \pi^0$ has been extracted allowing the continuum production amplitude to interfere with the resonance production amplitude. Later, the measurement of this reaction was performed at higher energies [14], namely at 13 center of mass energies, $\sqrt{s}$, from 4.008 to 4.600 GeV (in the vicinity of the $Y(4260)$ resonance).

Some interesting results on the $N^{*,}$s production have been obtained. The $N^*(1440)$ peak was observed, for the first time, directly from πN invariant mass spectrum (due to the absence of the strong Δ peak). Besides several well known N^* resonances around $1520 MeV$ and $1670 MeV$, three new N^* resonances above $2 GeV$ were found using partial wave analyses. The measurement of the $\psi(2S) \to \bar{p} p \pi^0$ channel (by CLEO Collaboration) found a similar strong $N^*(1440)$ peak [15]. There is no obvious $N^*(1440)$ peak for $e^+e^- \to \bar{p} p \pi^0$ in the vicinity of the $\psi(3770)$ [13].

The time-like region became accessible with the advent of high-precision, high-intensity e^+e^- colliders at intermediate energies. New data from BESIII, collected in a high-precision energy scan in 2015, will offer improved precision over a large q^2 range. The coming upgrade of the BEPCII collider up to c.m.s. energies of $4.9 GeV$ will alow to study more details of the N^* production. The topics which planned to study at BESIII in the near future can be found in [16].

This paper opens the series of works devoted to the general analysis, in the one-photon-annihilation approximation, of the differential cross section and polarization observables in the process $e^+ + e^- \to N + \bar{N} + \pi^0$, where $N(\bar{N})$ is proton (antiproton) or neutron (antineutron). We intend to account for the continuum (non-resonant) and resonance (with different possible vector mesons or excited baryons in intermediate virtual states of Feynman diagrams) contributions. Here we concentrate on the detailed analysis of the hadronic tensor and kinematics suitable to calculate invariant variables distributions.

FORMALISM

We study the reaction

$$e^-(k_1) + e^+(k_2) \to N(p_1) + \bar{N}(p_2) + \pi^0(k), \tag{1}$$

where the notation of the particle four-momenta is indicated in the parenthesis. In one-photon annihilation approximation $q = k_1 + k_2 = p_1 + p_2 + k$ is the four-momentum of the virtual photon.

The matrix element, in this approximation, can be written down as an contraction of the leptonic (el_μ) and hadronic (eJ_μ) currents

$$M = \frac{e^2}{q^2} l^\mu J_\mu, \quad l^\mu = \bar{v}(k_2)\gamma^\mu u(k_1), \tag{2}$$

where $k^2 = m^2$, $p_1^2 = p_2^2 = M^2$, $m(M)$ is the pion (nucleon) mass. Further, we neglect the electron mass where it is possible.

Then, the square of the matrix element can be written as

$$|M|^2 = \frac{16\pi^2\alpha^2}{q^4} L^{\mu\nu} H_{\mu\nu}, \quad L^{\mu\nu} = l^\mu l^{\nu*}, \quad H_{\mu\nu} = J_\mu J_\nu^*. \tag{3}$$

The structure of the hadronic tensor

The hadronic tensor $H_{\mu\nu}$ has the following general form for the case when the polarizations of the final particles are not measured

$$H_{\mu\nu}(0) = H_1 \tilde{g}_{\mu\nu} + H_2 \tilde{k}_\mu \tilde{k}_\nu + H_3 \tilde{p}_\mu \tilde{p}_\nu + H_4 (\tilde{p}_\mu \tilde{k}_\nu + \tilde{p}_\nu \tilde{k}_\mu) + iH_5 (\tilde{p}_\mu \tilde{k}_\nu - \tilde{p}_\nu \tilde{k}_\mu), \tag{4}$$

where $\tilde{g}_{\mu\nu} = g_{\mu\nu} - q_\mu q_\nu / q^2$, $\tilde{k}_\mu = k_\mu - (k \cdot q / q^2) q_\mu$ and $\tilde{p}_\mu = p_\mu - (p.q / q^2) q_\mu$, $p = p_1 - p_2$. $H_i (i = 1 - 5)$ are the so-called structure functions depending on three invariant variables s_1, s_2 and $s \equiv q^2$ (see below).

The leptonic tensor $L_{\mu\nu}$ has the following form in the case when electron beam is polarized

$$L_{\mu\nu} = -q^2 g_{\mu\nu} + 2(k_{1\mu} k_{2\nu} + k_{1\nu} k_{2\mu}) + 2im_e(\mu\nu\eta q), \tag{5}$$

where $(\mu\nu ab) = \epsilon_{\mu\nu\rho\sigma} a^\rho b^\sigma$ and η_μ is the spin four-vector of the electron (we chose $\epsilon^{0123} = -\epsilon_{0123} = +1$), m_e is the electron mass.

At chosen normalization, the differential cross section of the process (1), in terms of the leptonic and hadronic tensors, has the following form (we neglect the electron mass for the initial particles leptonic current)

$$d\sigma = \frac{\alpha^2}{8\pi^3 q^6} L^{\mu\nu} H_{\mu\nu} dR_3, \quad dR_3 = \frac{d^3 p_1}{2E_1} \frac{d^3 p_2}{2E_2} \frac{d^3 k}{2E} \delta(k_1 + k_2 - p_1 - p_2 - k), \tag{6}$$

where $E_1(E_2)$ is the nucleon (antinucleon) energy and E is the pion one.

In the case when the nucleon polarization is measured, we can use the following form of the hadronic tensor

$$H_{\mu\nu} = \frac{1}{2} H_{\mu\nu}(0) + T_{\mu\nu},$$

where the tensor $T_{\mu\nu}$ depends on the nucleon polarization 4-vector S^μ and it can be written as the sum of the symmetrical $T_{\mu\nu}^{(s)}$ and antisymmetrical $T_{\mu\nu}^{(a)}$ parts.

The symmetrical part can be written as follows

$$T_{\mu\nu}^{(s)}(S) = Im\{T_{kk}\,\tilde{k}_k^{\mu\nu} + T_{kp}\,\tilde{k}_p^{\mu\nu} + T_{pk}\,\tilde{p}_k^{\mu\nu} + T_{pp}\,\tilde{p}_p^{\mu\nu} + T_G\,\tilde{G}^{\mu\nu} + T_K\,\tilde{K}^{\mu\nu} + T_P\,\tilde{P}^{\mu\nu} + T_{KP}\,KP^{\mu\nu}\},\tag{7}$$

where

$$\tilde{k}_k^{\mu\nu} = \tilde{k}(\nu kqS) + \tilde{k}(\mu kqS),\ \ \tilde{k}_p^{\mu\nu} = \tilde{k}(\nu pqS) + \tilde{k}(\mu pqS),$$

$$\tilde{p}_k^{\mu\nu} = \tilde{p}^\mu(\nu kqS) + \tilde{p}^\nu(\mu kqS),\ \ \tilde{p}_p^{\mu\nu} = \tilde{p}^\mu(\nu pqS) + \tilde{p}^\nu(\mu pqS),$$

$$\tilde{G}^{\mu\nu} = \tilde{g}^{\mu\nu}(kpqS),\ \ \tilde{K}^{\mu\nu} = \tilde{k}^\mu\tilde{k}^\nu(kpqS),\ \ \tilde{P}^{\mu\nu} = \tilde{p}^\mu\tilde{p}^\nu(kpqS),$$

$$KP^{\mu\nu} = [\tilde{k}^\mu\tilde{p}^\nu + \tilde{p}^\mu\tilde{k}^\nu](kpqS),\ \ (\mu abc) = {}_{\mu\nu\ \sigma}a^\nu b\ c^\sigma,\ \ (abcd) = {}_{\mu\nu\ \sigma}a^\mu b^\nu c\ d^\sigma.$$

The antisymmetrical part is

$$T_{\mu\nu}^{(a)}(S) = i\,Re\{T_s\,(\mu\nu qS) + T_{pps}\,(pS)(\mu\nu pq) + T_{pqs}\,(qS)(\mu\nu pq) + T_{kps}\,(pS)(\mu\nu kq) + T_{kqs}\,(qS)(\mu\nu kq)\}.\tag{8}$$

The invariant amplitudes

The general form of the matrix element (2) can be chosen by analogy with the process of the pion electroproduction on the nucleons [17]. If the gauge invariance and the space parity conservation take place, we have

$$M = \frac{e^2}{q^2}\,\varphi_\pi^+\,\Sigma_{i=1}^6\,\bar{u}(p_1)\,\gamma_5\,M_i\,v(p_2)\,A_i,\ \ \gamma_5 = i\gamma^0\gamma^1\gamma^2\gamma^3,\tag{9}$$

where φ_π is the pion wave function and the M_i structures have the following form

$$M_1 = \frac{1}{2}\gamma^\mu\gamma^\nu F_{\mu\nu},\ M_2 = p^\mu k^\nu F_{\mu\nu},\ M_3 = \gamma^\mu k^\nu F_{\mu\nu},\ M_4 = (\gamma^\mu p^\nu - 2M\gamma^\mu\gamma^\nu)F_{\mu\nu},\tag{10}$$

$$M_5 = q^\mu k^\nu F_{\mu\nu},\ M_6 = q^\mu\gamma^\nu F_{\mu\nu},\ F_{\mu\nu} = l_\mu q_\nu - l_\nu q_\mu.$$

The invariant amplitudes $A_i\,(i = 1-6)$ are the complex functions of three independent variables: for example, q^2 − the square of the total invariant mass of the final hadrons, and $s_{1,2} = (p_{1,2} + k)^2$ -the square of the invariant masses of the $N\pi^0$ and $\bar{N}\pi^0$ systems.

Equations (9) and (10) mean that, in general case, J_μ can be written as follows

$$J_\mu = \varphi_\pi^+\,\bar{u}(p_1)\,\gamma_5\hat{O}_\mu\,v(p_2),\tag{11}$$

where the matrix $\hat{O}_\mu$ has the form

$$\hat{O}_\mu = (k\cdot q\,p_\mu - p\cdot q\,k_\mu)A_2 - q^2\tilde{k}_\mu A_5 + (k\cdot q\,A_3 + p\cdot q\,A_4 - q^2\,A_6)\gamma_\mu +\tag{12}$$

$$+(A_6\,q_\mu - A_4\,p_\mu - A_3\,k_\mu)\hat{q} + (A_1 - 4M\,A_4)(\gamma_\mu\,\hat{q} - q_\mu).$$

The hadronic structure functions in Eq. (4), which are independent on the nucleon polarization states, can be written, in general case, in terms of the invariant amplitudes as follows

$$H_1 = 2\{[m^2q^2 + (p\cdot q)^2 - (k\cdot q)^2]\,|\,A_{14}\,|^2 + p^2\,|\,k\cdot q\,A_3 + p\cdot q\,A_4 - q^2\,A_6\,|^2 +$$

$$+4Mp\cdot q\,Re[k\cdot q\,A_3 + p\cdot q\,A_4 - q^2\,A_6]A_{14}^*\,\},\ A_{14} = A_1 - 4MA_4,\tag{13}$$

$$H_2 = 2\{(p\cdot q)^2\,|\,A_4\,|^2 + [q^2(p^2 + q^2) - (p\cdot q)^2]\,|\,A_3\,|^2 + (q-k)^2[(p\cdot q)^2\,|\,A_2\,|^2 + q^4\,|\,A_5\,|^2]$$

$$+q^2(q^2\,|\,A_6\,|^2 - |\,A_{14}\,|^2)\} + 4\,Re\{-p\cdot q\,(p\cdot q\,A_2 + q^2\,A_5)A_{14}^* + p\cdot q\,(q^2\,A_3 - 2Mp\cdot q\,A_2)A_4^* +$$

$$+q^2[2M(p\cdot q\,A_2 + q^2\,A_5) - q^2\,A_3 - p\cdot q\,A_4]A_6^* - 2Mq^2\,p\cdot q\,A_2\,A_3^* + q^2[p\cdot q(q-k)^2\,A_2 - 2M(q^2\,A_3 + p\cdot q\,A_4)]A_5^*\}, \quad (14)$$

$$H_3 = 2\{(k\cdot q)^2[(q-k)^2\,|A_2|^2 - |A_3|^2] + q^2\,|A_{14}|^2 - q^4\,|A_6|^2 + [(k\cdot q - q^2)^2 + q^2\,p^2]|A_4|^2\} +$$

$$+4Re\{k\cdot q(q^2 - k\cdot q)A_2(A_{14}^* + 2MA_4^*) + q^2(2MA_4\,A_{14}^* + k\cdot q\,A_3\,A_6^*)\}, \quad (15)$$

$$H_4 = 2\{k\cdot q\,p\cdot q(|A_3|^2 - (q-k)^2\,|A_2|^2) + p\cdot q(q^2 - k\cdot q)|A_4|^2\} + 2Re\{2Mq^2 k\cdot q\,A_2\,A_3^* +$$

$$+[p\cdot q(2k\cdot q - q^2)A_2 + 2Mq^2\,A_3 - q^2(q^2 - k\cdot q)A_5]A_{14}^* + q^2[(k\cdot q - q^2)A_4 - 2Mk\cdot q\,A_2 - p\cdot q\,A_3]A_6^* +$$

$$+q^2[-k\cdot q(q-k)^2\,A_2 + 2M(k\cdot q - q^2)A_4]A_5^* + [2Mp\cdot q(2k\cdot q - q^2)A_2 + q^2(q^2 + p^2 - k\cdot q)A_3]A_4^*\}, \quad (16)$$

$$H_5 = -2q^2\,Im\{[2M\,A_3 - q\cdot p\,A_2 - (q^2 - k\cdot q)A_5]A_{14}^* + [-2Mk\cdot q\,A_2 + q\cdot p\,A_6 -$$

$$-(p^2 + q^2 - k\cdot q)A_4]A_3^* + [k\cdot q(q-k)^2\,A_2 - 2M(k\cdot q - q^2)A_4]A_5^* + [(q^2 - k\cdot q)A_4 + 2Mk\cdot q\,A_2]A_6^* - 2Mq\cdot p\,A_2\,A_4^*\}. \quad (17)$$

The relations between the invariant amplitudes and the hadronic structure functions in Eqs. (7) and (8), which depend on the nucleon polarization states, are more complicated and read

$$T_{kk} = [p\cdot q(A_4 - 2MA_2) - q^2(2MA_5 + A_6) + \frac{1}{2q\cdot p_1}[q^2(p^2 + q^2 - k\cdot q) + p\cdot q(k\cdot q - p\cdot q)]A_3]A_{14}^*$$

$$+\frac{p^2}{2q\cdot p_1}(k\cdot q\,A_3 + p\cdot q\,A_4 - q^2\,A_6)(p\cdot q\,A_2^* + q^2\,A_5^*), \quad (18)$$

$$T_{kp} = [q^2\,A_6 - p\cdot q\,A_4 + \frac{(p\cdot q)^2 + m^2 q^2 - k\cdot q(p\cdot q + q^2)}{2q\cdot p_1}A_3]A_{14}^* +$$

$$2M(p\cdot q\,A_3\,A_4^* - q^2\,A_3\,A_6^*) + \frac{(p_1 + p_2)^2}{2q\cdot p_1}(k\cdot q\,A_3 + p\cdot q\,A_4 - q^2\,A_6)(p\cdot q\,A_2^* + q^2\,A_5^*), \quad (19)$$

$$T_{pk} = [k\cdot q(2MA_2 + A_3) - q^2\,A_6 - (k\cdot q - q^2 - \frac{p^2 q^2}{2q\cdot p_1})A_4]A_{14}^* - \frac{k\cdot q\,p^2}{2q\cdot p_1}(k\cdot q\,A_3 + p\cdot q\,A_4 - q^2\,A_6)A_2^*, \quad (20)$$

$$T_{pp} = [q^2\,A_6 - k\cdot q\,A_3 - [p\cdot q - \frac{(p\cdot q)^2 + q^2 m^2 - (k\cdot q)^2}{2q\cdot p_1}]A_4]A_{14}^* +$$

$$2M(q^2\,A_6 - k\cdot q\,A_3)A_4^* - \frac{k\cdot q(p_1 + p_2)^2}{2q\cdot p_1}(k\cdot q\,A_3 + p\cdot q\,A_4 - q^2\,A_6)A_2^*, \quad (21)$$

$$T_K = \frac{1}{q\cdot p_1}\{[q^2\,A_6 - p\cdot q\,A_4 - (p\cdot q + q^2)A_3](p\cdot q\,A_2^* + q^2\,A_5^*) - q^2\,A_3\,A_{14}^*\}, \quad (22)$$

$$T_P = \frac{1}{q\cdot p_1}\{k\cdot q[q^2\,A_6 - (k\cdot q - q^2)A_4 - k\cdot q\,A_3]A_2^* + q^2\,A_4\,A_{14}^*\}, \quad (23)$$

$$T_{KP} = -\frac{1}{2q\cdot p_1}\{[q^2(p\cdot q + k\cdot q)A_6 - k\cdot q(2p\cdot q + q^2)A_3 - p\cdot q(2k\cdot q - q^2)A_4]A_2^* +$$

$$q^2(A_4 - A_3)A_{14}^* + q^2[q^2\,A_6 - k\cdot q\,A_3 + (q^2 - k\cdot q)A_4]A_5^*\}, \quad (24)$$

$$T_G = 2(k\cdot q\,A_3 + p\cdot q\,A_4 - q^2\,A_6)A_{14}^*, \quad (25)$$

$$T_s = 2Mp\cdot q(k\cdot q\,|A_3|^2 + p^2\,|A_4|^2 + q^2\,|A_6|^2 + |A_{14}|^2) +$$

$$[2Mp\cdot q(k\cdot q - m^2)A_2 + [k\cdot q(p^2 - k\cdot q) + (p\cdot q)^2 + m^2 q^2]A_3 + p\cdot q(4M^2 + p^2)A_4 +$$

$$2M[(k \cdot q)^2 - m^2 q^2] A_5 + [(k \cdot q - q^2)^2 - (p \cdot q)^2 - 4M^2 q^2] A_6] A_{14}^* +$$

$$[[(4M^2 - p^2)(p \cdot q)^2 + p^2 k \cdot q (k \cdot q - q^2)] A_2 - 2M[p \cdot q (k \cdot q + q^2) A_3 + ((p \cdot q)^2 + p^2 q^2) A_4] +$$

$$(4M^2 - p^2) p \cdot q q^2 A_5] A_6^* + [-(4M^2 - p^2) p \cdot q k \cdot q A_3 + p^2 [(k \cdot q)^2 - m^2 q^2] A_4] A_5^* +$$

$$[p^2 p \cdot q (k \cdot q - m^2) A_2 + 2M[p^2 k \cdot q + (p \cdot q)^2] A_3] A_4^* + p^2 k \cdot q (k \cdot q - m^2) A_2 A_3^*, \quad (26)$$

$$T_{pps} = 2M(k \cdot q |A_3|^2 + p \cdot q |A_4|^2) + p \cdot q (A_3 + A_4) A_{14}^* +$$

$$[(k \cdot q - p \cdot q)(k \cdot q - q^2) A_2 - 2M q^2 (A_3 + A_4)] A_6^* + [(k \cdot q)^2 - m^2 q^2] A_4 A_5^* +$$

$$[(k \cdot q - m^2) p \cdot q A_2 + 2M(k \cdot q + p \cdot q) A_3] A_4^* + (k \cdot q - m^2) k \cdot q A_2 A_3^* + (k \cdot q - q^2)(k \cdot q A_3 - q^2 A_6) A_5^*, \quad (27)$$

$$T_{pqs} = 2M(k \cdot q |A_3|^2 + q^2 |A_6|^2 + p \cdot q A_3 A_4^*) + 2(q \cdot p_2 A_6 - k \cdot p_2 A_3) A_{14}^* +$$

$$[(4M^2 - p^2)(p \cdot q A_2 + q^2 A_5) - 2M[(k \cdot q + q^2) A_3 + p \cdot q A_4]] A_6^* - (4M^2 - p^2) k \cdot q A_3 A_5^*, \quad (28)$$

$$T_{kps} = [2M[(k \cdot q - p \cdot q) A_2 - q^2 A_5] + (q^2 - k \cdot q)(A_3 + A_4)] A_{14}^* +$$

$$p \cdot q[(p \cdot q - k \cdot q) A_2 + q^2 A_5] A_6^* + (p \cdot q - p^2)(k \cdot q A_2 A_3^* + p \cdot q A_2 A_4^*) +$$

$$[-k \cdot q p \cdot q A_3 + [-k \cdot q p \cdot q + q^2 (p \cdot q - p^2)] A_4] A_5^*, \quad (29)$$

$$T_{kqs} = -2M |A_{14}|^2 + [2M[(k \cdot q - q^2) A_5 - p \cdot q A_2] + 2q \cdot p_2 (A_3 - A_6) - p^2 A_4] A_{14}^* +$$

$$p^2 [k \cdot q (A_2 A_6^* - A_2 A_3^*) - p \cdot q A_2 A_4^* + (k \cdot q - q^2) A_4 A_5^*]. \quad (30)$$

The nucleon polarization 4-vector

In the rest frame of the nucleon $(\mathbf{p}_1 = 0)$ its polarization four-vector has the form $S_r^\mu = (0, \mathbf{n})$, $\mathbf{n}^2 = 1$, and, in general case, 3-vector $\mathbf{n}$ has three independent components: two in the plane $(\mathbf{q}, \mathbf{k})$ and one along 3-vector $[\mathbf{k} \times \mathbf{q}]$. It means that in arbitrary Lorentz system 4-vector S^μ can be expressed by means of 4-vectors of the particle momenta and expanded by three independent 4-vectors: longitudinal S_L^μ, transversal S_T^μ and normal S_N^μ.

Let us choose the longitudinal polarization such that in the rest frame $\mathbf{n} = -\mathbf{q}/|\mathbf{q}|$. It can be expressed in terms of 4-vectors p_1^μ and q^μ, and has the following form

$$S_L^\mu = \frac{q \cdot p_1 p_1^\mu - M^2 q^\mu}{M K}, \quad K = \sqrt{(q \cdot p_1)^2 - q^2 M^2}, \quad S_L \cdot p_1 = 0, \quad S_L^2 = -1. \quad (31)$$

Note also that in c. m. s. of the process (1), where $\mathbf{q} = 0$,

$$S_L^\mu = \left(\frac{|\mathbf{p}_1|}{M}, \frac{E_1 \mathbf{p}_1}{M |\mathbf{p}_1|} \right).$$

The transversal polarization was chosen to be orthogonal to the longitudinal one, that is

$$S_T^\mu \cdot S_L^\mu = 0, \to S_T \cdot p_1 = 0, \quad S_T \cdot q = 0, \quad S_T^2 = -1.$$

The relation $S_T \cdot q = 0$ indicates that the polarization 4-vector S_T^μ is expressed in terms of the 4-vectors $\tilde{p}_1$, $\tilde{p}_2$ and $\tilde{k}$. Only two 4-vectors are independent since we have the following relation $\tilde{p}_1 + \tilde{p}_2 + \tilde{k} = 0$. Choosing $\tilde{p}_1$ and $\tilde{k}$ one can obtain

$$S_T^\mu = \frac{(q^2 \, k \cdot p_1 - q \cdot p_1 \, k \cdot q) \, \tilde{p}_1^\mu + [(q \cdot p_1)^2 - q^2 M^2] \tilde{k}^\mu}{K \, N}, \tag{32}$$

where

$$N = \sqrt{-(\mu k p_1 q)(\mu k p_1 q)}, \ N^2 = 2 k \cdot q \, k \cdot p_1 \, q \cdot p_1 - q^2 \, (k \cdot p_1)^2) - M^2 (k \cdot q)^2 - m^2 (q \cdot p_1)^2 + q^2 M^2 m^2 .$$

In both coordinate system (the rest system and c. m. s.) the 4-vector S_T^μ has not the time component and its space component is

$$\frac{[\mathbf{q} \times [\mathbf{k} \times \mathbf{q}]]}{|[\mathbf{q} \times [\mathbf{k} \times \mathbf{q}]]|}, \ \frac{[\mathbf{p}_1 \times [\mathbf{k} \times \mathbf{p}_1]]}{|[\mathbf{p}_1 \times [\mathbf{k} \times \mathbf{p}_1]]|}$$

in the rest frame and the c. m. s., correspondingly.

It is clear that the normal polarization is

$$S_N^\mu = \frac{(\mu k p_1 q)}{N} = (0, \frac{[\mathbf{k} \times \mathbf{p}_1]}{|[\mathbf{k} \times \mathbf{p}_1]|}) \, (in \, the \, c.m.s.) = (0, \frac{[\mathbf{q} \times \mathbf{k}]}{|[\mathbf{q} \times \mathbf{k}]|}) \, (in \, the \, rest) . \tag{33}$$

KINEMATICS

We define five independent invariant variables as follows

$$s = (k_1 + k_2)^2 = (p_1 + p_2 + k)^2, \ s_1 = (p_1 + k)^2 = (k_1 + k_2 - p_2)^2, \tag{34}$$

$$s_2 = (p_2 + k)^2 = (k_1 + k_2 - p_1)^2, \ t_1 = (k_1 - p_1)^2 = (p_2 + k - k_2)^2, \ t_2 = (k_2 - p_2)^2 = (p_1 + k - k_1)^2 .$$

The scalar products of the 4-momenta in the process can be written in terms of these invariants as

$$2 k_1 \cdot p_2 = s - s_1 + t_2 - m_e^2, \ 2 k_2 \cdot p_1 = s - s_2 + t_1 - m_e^2, \ 2 k_1 \cdot k = s_1 + t_1 - t_2 - M^2, \tag{35}$$

$$2 k_2 \cdot k = s_2 + t_2 - t_1 - M^2, \ 2 p_1 \cdot p_2 = s - s_1 - s_2 + m^2, \ 2 k_1 \cdot k_2 = s - 2 m_e^2,$$

$$2 k_2 \cdot p_2 = M^2 + m_e^2 - t_2, \ 2 k_1 \cdot p_1 = M^2 + m_e^2 - t_1, \ 2 k \cdot p_1 = s_1 - M^2 - m^2, \ 2 k \cdot p_2 = s_2 - M^2 - m^2 .$$

The limits of the changing of the invariant variables can be obtained from the condition of positivity of the quantity $(-\Delta) = (k_1 k_2 p_1 p_2)^2$, where Δ is the Gramian determinant. It has a form

$$\Delta = \frac{1}{16} \begin{vmatrix} 2 m_e^2 & s - 2 m_e^2 & M^2 + m_e^2 - t_1 & s - s_1 + t_2 - m_e^2 \\ s - 2 m_e^2 & 2 m_e^2 & s - s_2 + t_1 - m_e^2 & M^2 + m_e^2 - t_2 \\ M^2 + m_e^2 - t_1 & s - s_2 + t_1 - m_e^2 & 2 M^2 & s - s_1 - s_2 + m^2 \\ s - s_1 + t_2 - m_e^2 & M^2 + m_e^2 - t_2 & s - s_1 - s_2 + m^2 & 2 M^2 \end{vmatrix} .$$

Taking into account the azimuthal symmetry relative to the line of the colliding electron-positron beams, the phase space of the final particles can be written as [18]

$$d R_3 = \frac{\pi}{16(s - 2 m_e^2)} \frac{d t_1 \, d t_2 \, d s_1 \, d s_2}{\sqrt{-\Delta}}, \tag{36}$$

Note, that we can neglect, with the very high accuracy, the electron mass in our calculations.

All the scalar products in hadronic part depend on the variables s, s_1 and s_2

$$q^2 \equiv s, \, p^2 = 2M^2 - m^2 + s_1 + s_2 - s, \, q \cdot p = k \cdot p = \frac{s_1 - s_2}{2}, \, k \cdot q = \frac{s_1 + s_2}{2} - M^2, \, d_1 = s_2 - M^2, \, d_2 = s_1 - M^2.$$

In further works we are going to concentrate on the double differential distributions. To study the (s_1, t_2) or (s_2, t_1)-distributions, it is enough to measure the 4-momentum p_1 or p_2, respectively. To investigate the $(s_1, s_2), (s_1, t_1), (s_2, t_2), (t_1, t_2)$-ones, we have to measure both p_1 and p_2.

Let us consider the ranges of the invariant variables to study the (s_1, s_2) distribution. In this case, it is necessary to integrate over t_1 and t_2. From the positivity of the quantity $(-\Delta)$, we conclude

$$t_{1-} \leq t_1 \leq t_{1+}, \quad t_{1\pm} = \frac{A(s, s_1, s_2, t_2) \pm 2\sqrt{B(s, s_1, s_2) C(s, s_1, t_2)}}{(s + s_1 - M^2)^2 - 4ss_1}, \tag{37}$$

$$A(s, s_1, s_2, t_2) = m_e^2 [2M^4 - M^2(3s_1 + s_2) + ss_2 - 2m^2 s - s_1(s - s_1 - s_2)]$$

$$-M^2[m^2 s + s_1(s_2 - 2s - t_2) + t_2(2s - s_2)] - t_2[s(s_1 + s_2 - s - 2m^2) + s_1 s_2] + m^2 s(s - s_1) + M^6 - M^4(s + s_1 + t_2) - s_1 s_2(s - s_1),$$

$$B(s, s_1, s_2) = s_1 s_2(s_1 + s_2 - s) + 2M^6 - M^4(s + s_1 + s_2 + m^2)$$

$$+M^2[ss_2 + s_1(s - 2s_2) + m^2(s_1 + s_2 - 2s)] + m^4 s + m^2[s(s - s_1 - s_2) - s_1 s_2],$$

$$C(s, s_1, t_2) = s[t_2(s - s_1 + t_2 - M^2) + M^2 s_1] + m_e^2[M^4 - M^2(s + 2s_1) - s(s_1 + 2t_2) + s_1^2 + m_e^4 s].$$

The expression under the square root in Eq. (37) factorizes, and the limits on the variable $t_2(s_2)$ can be found from the condition $C(s, s_1, t_2) \geq 0$, $(B(s, s_1, s_2) \geq 0)$. For the variable t_2 they read

$$t_{2-} \leq t_2 \leq t_{2+}, \, t_{2\pm} = \frac{1}{2}\left[M^2 + 2m_e^2 - s + s_1 \pm \sqrt{\left(1 - \frac{4m_e^2}{s}\right)\left[(s + s_1 - M^2)^2 - 4ss_1\right]} \right] \tag{38}$$

As concerns the s_2 limits, we have

$$s_{2-} \leq s_2 \leq s_{2+}, \, s_{2\pm} = \frac{1}{2s_1}\left(D(s, s_1) \pm \sqrt{F(s, s_1) G(s, s_1)} \right), \tag{39}$$

$$D(s, s_1) = M^4 - M^2(s - 2s_1 + m^2) + m^2(s + s_1) + s_1(s - s_1),$$

$$F(s, s_1) = (s + s_1 - M^2)^2 - 4ss_1, \, G(s, s_1) = (s_1 + m^2 - M^2)^2 - 4m^2 s_1.$$

Both expressions $F(s, s_1)$ and $G(s, s_1)$ have not to be negative, and we obtain

$$(m + M)^2 \leq s_1 \leq (\sqrt{s} - M)^2. \tag{40}$$

It is clear that the inequalities (38), (39) and (40) define the regions (s_1, s_2) and (s_1, t_2) which are plotted in Figs. 1 a) and 1 b), correspondingly. Because of the symmetry of the Gramian determinant at $(s_1 \quad s_2, t_1 \quad t_2)$-permutation one can use the above inequalities to obtain also the region (s_2, t_1).

It is interesting to investigate the distribution over the nucleon-antinucleon invariant mass squared $s_{12} = (p_1 + p_2)^2 = 2M^2 + m^2 + s - s_1 - s_2$. For this goal, we define firstly the region (s_1, s_{12}) and use the inequality (see Eq.(37))

$$B(s, s_1, s_2 = 2M^2 + m^2 + s - s_1 - s_{12}) \geq 0$$

to obtain the limits on the variable s_1 at fixed values of the variable s_{12}

$$s_{1-} \leq s_1 \leq s_{1+}, s_{1\pm} = \frac{1}{2}[2M^2 + m^2 + s - s_{12} \pm \sqrt{(1 - \frac{4M^2}{s_{12}})[(s + m^2 - s_{12})^2 - 4m^2 s]}]. \tag{41}$$
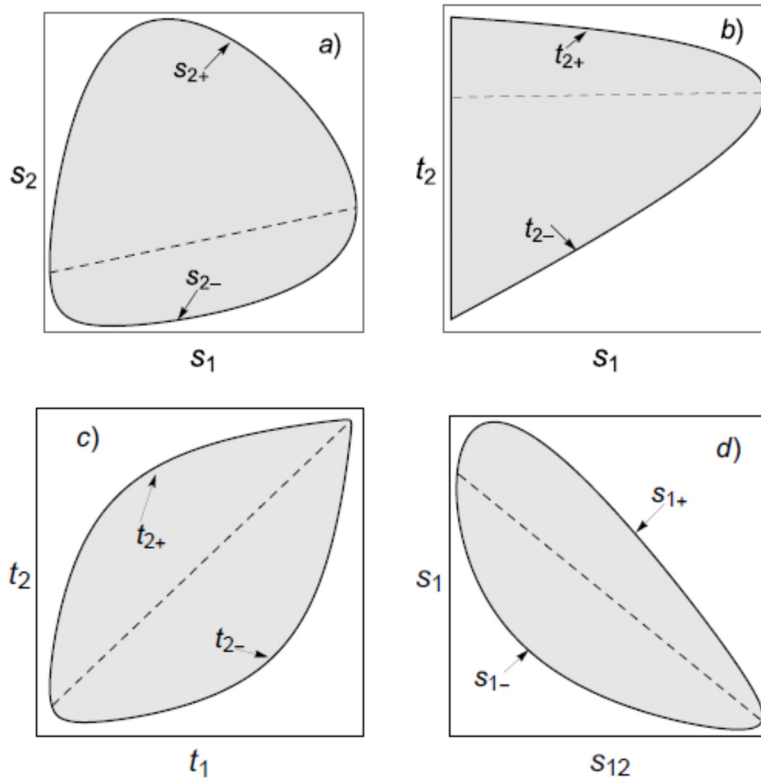
Figure 1. The kinematical double invariant variables regions calculated at $s = 10\,GeV^2$
(a) $-(s_1, s_2)$, (b) $-(s_1, t_2)$, (c) $-(t_1, t_2)$ and (d) $-(s_{12}, s_1)$.

Taking into account that the expression under square root in Eq.(41) has not to be negative, one finds the limits on the variable s_{12}

$$4M^2 \leq s_{12} \leq (\sqrt{s} - m)^2.$$

As concerns the region (t_1, t_2), the corresponding boundaries are more complicated and the analytical expressions for them require additional short notation. We introduce

$$G(x, y, z, u, v, w) = -\frac{1}{2} \begin{vmatrix} 2u & u - v + x & u + w - y \\ u - v + x & 2x & w + x - z \\ u + w - y & w + x - z & 2w \end{vmatrix},$$

$$s_{1-} < s_1 < s_{1+},$$

$$s_{1\pm} = \frac{(a \pm b)}{(m_e^2 - s_2^+)^2 - 4t_1 s_2}, b = 2\sqrt{G(s, t_1, s_2, m_e^2, m_e^2, M^2) G(t_2, s_2, t_1, M^2, m_e^2, m^2)},$$

$$a = s_2^- \left[s(t_1 - m^2) + M^2(t_+ - M^2) - s_2 t_2 \right] + s(t_2 s_2^+ - 2M^2 t_1) + m_e^2 \left[m_e^2(s - 2M^2) + \right.$$

$$+ m^2(s - 2M^2 + 2s_2) + M^2(M^2 + t_+ + 2s_2^+) + st_- - s_2(t_+ + s_2) \bigg],$$

$$\frac{-\lambda_{12}\lambda_2 + a_1}{2t_2} < s_2 < \frac{\lambda_s \lambda_1 + b_1}{2m_e^2},$$

where

$$a_1 = t_-(t_2 - m_e^2) + m^2(-M^2 + m_e^2 + t_2) + M^2 t_+, \; b_1 = s(t_1 - M^2) + m_e^2(s + 2M^2),$$

$$s_2^\pm = s_2 \pm t_1, \; t_\pm = t_1 \pm t_2, \; \lambda(x,y,z) = x^2 - 2xy - 2xz + y^2 - 2yz + z^2,$$

$$\lambda_{1,2} = \sqrt{\lambda\left(t_{1,2}, m_e^2, M^2\right)}, \; \lambda_{12} = \sqrt{\lambda\left(t_1, t_2, m^2\right)}, \; \lambda_s = \sqrt{\lambda\left(s, m_e^2, m_e^2\right)}.$$

The boundaries of the region (t_1, t_2) are determined by the equation

$$\frac{-\lambda_{12}\lambda_2 + a_1}{2t_2} = \frac{\lambda_s \lambda_1 + b_1}{2m_e^2}. \tag{42}$$

It is clear that, at such high energies, the electron mass cannot influence the kinematics, and to simplify following calculations we go to the limit $m_e - > 0.$ The Eq.(42), in this limiting case, reads

$$\frac{t_1\left(M^2 - s - t_1\right)}{M^2 - t_1} = \frac{(t_2 - M^2)(\lambda_{12} + m^2) + t_2 t_- + M^2 t_+}{2t_2},$$

and gives

$$t_2^- < t_2 < t_2^+$$

$$t_2^\pm = \frac{a_2 \pm b_2}{2\left(M^2 - t_1\right)\left(M^2 - s - t_1\right)}, \; a_2 = M^2[2t_1(s + t_1) - m^2 s + 2M^4 - M^2(s + 4t_1)] +$$

$$+ st_1(m^2 - s - t_1), \; b_2 = s\{M^4[M^4 + 4t_1(t_1 - M^2) + 2t_1(s + t_1)] +$$

$$+ t_1^2(s + t_1)(s + t_1 - 4M^2) + m^2(t_1 - M^2)[m^2(t_1 - M^2) + 2M^4 - 2t_1(s + t_1)]\}^{\frac{1}{2}},$$

$$\frac{a_3 - b_3}{2} \le t_1 \le \frac{a_3 + b_3}{2}, \; a_3 = 2M(M + m) + m^2 - s, \; b_3 = \sqrt{s - m^2}\sqrt{s - (m + 2M)^2}.$$

The regions (t_2, t_1) and (s_1, s_{12}) are plotted in the lower row in Fig. 1.

In addition, the dependence on the invariant mass of the $N\bar{N}$-system is also of the great interest. It is evident, that to study this dependence, it is enough to measure the pion 4-momentum k only. This ensures, at least, investigations of the double distributions over invariants $\bar{t}_1 = (k_1 - k)^2$, $s_{12} = (p_1 + p_2)^2$ or $\bar{t}_2 = (k_2 - k)^2, s_{12}$. To perform the corresponding calculations, it is necessary to investigate the Gramian determinant using $\bar{t}_1$ (or $\bar{t}_2$) and s_{12} variable of five independent invariant variables. In present paper such kind of distributions are not considered but we hope to study them in the next publications.

The matrix element squared of the process (1), as well as the differential cross section, are defined by the convolution of the leptonic and hadronic tensors (see Eq. (6)), that can be expressed in terms of the invariant amplitudes and chosen invariant variables. To calculate the contribution of any dynamical mechanism to the cross section, it is enough to know only the corresponding invariant amplitudes and this simplification is an essential advantage of the developed here formalism.

ORCID IDs
Mykhailo I. Konchatnij, https://orcid.org/0000-0002-9972-5348; **Nikolay P. Merenkov**, https://orcid.org/0000-0002-9743-3827
Egle Tomasi-Gustafsson, https://orcid.org/0000-0002-5263-3948

REFERENCES
[1] Bing-Song Zou, arXiv:1801.098221v1 [hep-ph], https://doi.org/10.48550/arXiv.1801.09822
[2] H. Li, BES Collaboration, H.C. Chiang, G.X. Peng, and B.S. Zou, Nucl. Phys. **A675**, 189 (2000), https://doi.org/10.1016/S0375-9474(00)00243-8.
[3] BES Collaboration, B.S.Zou et al., Excited Nucleons and Hadronic Structure, in: Proc. of NSTAR 2000 Conference at JLab, edited by V.D. Burkert, L. Elouadrhiri, J.J. Kelly, and R.C. Minehart, (World Scientific, 2001), pp. 155, https://doi.org/10.1142/4591.

[4]   M. Ablikim et al. [BESIII Collaboration], Phys. Rev. Lett. 124, 042001 (2020), https://doi.org/10.1103/PhysRevLett.124.042001.

[5]   M. Ablikim et al. [BESIII], Phys. Lett. **B814**, 136110 (2021), https://doi.org/10.1016/j.physletb.2021.136110.

[6]   M. Ablikim et al. [BESIII], Phys. Lett. **B817**, 136328 (2021), https://doi.org/10.1016/j.physletb.2021.136328.

[7]   J. Haidenbauer, U. G.Meißner and L. Y. Dai, Phys. Rev. **D103**, 014028 (2021), https://doi.org/10.1103/PhysRevD.103.014028.

[8]   E. Tomasi-Gustafsson, A. Bianconi and S. Pacetti, Phys. Rev. **C103**, 035203 (2021), https://doi.org/10.1103/PhysRevC.103.035203.

[9]   Y. M. Bystritskiy, Phys. Rev. **D103**, 116029 (2021), https://doi.org/10.1103/PhysRevD.103.116029.

[10] B.S. Zou, Nucl. Phys. **A684**, 330 (2001), https://doi.org/10.1016/S0375-9474(01)00433-X;

[11] Nucl. Phys. **A675**, 167 (2000), https://doi.org/10.1103/PhysRevD.66.054020

[12] D.M. Asner et al., Int. J. Mod. Phys. A, **24**, S1 (2009) [arXiv:0809.1869 [hep-ex]], https://doi.org/10.48550/arXiv.0809.1869.

[13] M. Ablikim et al. (BESIII Collaboration), Phys. Rev. **D90**, 032007 (2014), arXiv:1406.2486v1 [hep-ex], https://doi.org/10.1103/PhysRevD.90.032007

[14] M. Ablikim et al., Phys.Lett. **B771**, arXiv:1701.04198v1 [hep-ex], https://doi.org/10.1016/j.physletb.2017.05.033.

[15] J.P. Alexander et al. [CLEO Collaboration], Phys. Rev. **D82**, 092002 (2010), [arXiv:1007.2886 [hep-ex]], https://doi.org/10.1103/PhysRevD.82.092002

[16] IHEP-Physics-Report-BESIII-2019-12-13, arXiv:1912.05983v1 [hep-ex], https://doi.org/10.48550/arXiv.1912.05893

[17] S. Adler, Ann. Phys. **50**, 189 (1968), https://doi.org/10.1016/0003-4916(68)90278-9

[18] E. Byckling, and K. Kajantie, *Particle Kinematics* (Wiley, London, New York, Sydney, Toronto, 1973)

ЗАГАЛЬНИЙ АНАЛІЗ РЕАКЦІЇ $e^+ + e^- \to N + \bar{N} + \pi^0$

Г.І. Гах[a], М.І. Кончатний[a], М.П. Меренков[a], Егле Томасі-Густафссон[b]

[a]Національний науковий центр «Харківський фізико-технічний інститут»
вул. Академічна, 1, 61108, м. Харків, Україна
[b]IRFU, CEA, Університет Париж-Сакле, 91191, Жів-сюр-Іветт, Франція

У наближенні однофотонної анігіляції виконано загальний аналіз реакції $e^+ + e^- \to N + \bar{N} + \pi^0$ у випадку поздовжньо поляризованого пучка електронів з врахуванням поляризаційних станів кінцевого нуклона. Цей аналіз є корисним для опису внесків континума (не резонасний) та резонансного (з різними можливими векторними мезонами або збудженими баріонами у проміжних віртуальних станах діаграм Фейнмана). Для виразу матричного елемента у термінах шести комплексних незалежних інваріантних амплітуд було використано збереження електромагнітних струмів адронів та P-інваріантність електромагнітної взаємодії адронів. Була визначена загальна структура адронного тензора у випадку неполяризованих кінцевих адронів і поляризованого нуклона. Спіннезалежна частина адронного тензора визначається п'ятьма структурними функціями, а спінзалежна – 13 структурними функціями. Поперечна, повздовжня та нормальна компоненти нуклонного чотиривектора поляризації виражені у термінах чотиривекторів імпульсів частинок. Застосовані п'ять незалежних інваріантних змінних що описують реакцію. Досліджені межі існування цих змінних. Кінематичні області подвійних інваріантних змінних приведені на рисунку. Досліджена кінематика яка зручна для дослідження розподілів по інваріантній масі.

Ключові слова: поляризаційні явища, електрон, іваріантні амплітуди, адронний тензор, кінематика.

SPECIFIC FEATURES OF THE SIMULATION OF THE PARTICLE DIFFUSION PROCESSES IN SPATIALLY PERIODIC FIELDS†

Viktoriia Yu. Aksenova[a,b]*, Ivan G. Marchenko[a,b&], Igor I. Marchenko[c#]

aV.N. Karazin Kharkiv National University
4 Svobody Square, Kharkiv, 61022, Ukraine
bNational Science Center «Kharkiv Institute of Physics and Technology»
1 Akademichna Street, Kharkiv, 61108, Ukraine
cNTU «Kharkiv Polytechnic Institute», Kharkiv, Ukraine
*Corresponding Author: nzarkevich@gmail.com, +380989079101, +4915128359513
&E-mail: marchkipt@gmail.com, #E-mail: igor.marchenko@hotmail.com
Received May 9, 2022; accepted May 23, 2022

This paper is devoted to the studies of the specific features of the simulation of the particle diffusion processes in space – periodic potentials using Langevin equations. Different methods used for the presetting of initial conditions and their effect on the obtained solutions have been analyzed. It is shown that the system is nonequilibrium for all the methods of the presetting of initial conditions during a certain time interval of t_{trm}. This interval is increased as $1/\gamma$ with a decrease in the friction coefficient. A reasonable description of the transient processes of particle transport and diffusion requires a preliminary system thermalization procedure. A new method of the presetting of initial conditions that provides the most accurate description of equilibrium system has been suggested. It consists in the generation of the initial particle coordinates and velocities that correspond to the equilibrium distribution of harmonic oscillators with a specified temperature. The use of such initial conditions enables the computations with a good accuracy using no thermalization procedure at $T < 0.1$. The classic method of the determination of diffusion coefficients D as a limit $\lim_{t \to \infty}(\sigma^2/2t)$ has been analyzed. It was shown that the use of it for computer-aided calculations is limited by the restricted computational time. It results in that the computation of D under certain conditions becomes impossible. A new method was suggested for the determination of the diffusion coefficient using the linear approximation of the dependence of dispersion on time. This approximation can only be possible after the kinetic temperature attains its stationary value. The suggested method requires several orders of magnitude less time in comparison to the classic method. As a result, it enables the computation of the diffusion coefficient even in the cases of total previous failure. The obtained data are of great importance for correct simulation computations of diffusion processes and for the appropriate physical interpretations of obtained data.
Keywords: diffusion, computer simulation, Langevin equations, initial conditions, external fields.
PACS: 05.40.-a, 02.50.Ey, 68.43.Jk, 66.30.J-

Particle transport and diffusion processes in periodic potentials that are exposed to the action of external fields play an important role for different phenomena peculiar for physics, chemistry and biology [1-2]. For example, Josephson junctions [3], superionic conductors [4], Josephson Vortex [5], charge density waves [6], magnetic ratchets [7], granular gas [8], surface diffusion [9], optic vortexes [10] and the membrane permeability [11], actually it is by far incomplete list of mentioned phenomena.

Recently, a substantial progress was achieved in the analytical studies of the particle transport and diffusion in the overdamped state [12-13]. At the same time, the developed methods are poorly acceptable for low dissipation systems. In this connection, the methods of computer simulation were intensively used along with analytical computations. In particular, the numerical solution of Langevin equations [14-18] has intensively been used.

Numerical solution of stochastic equations has the specific features of its own that are relating both to the presetting of initial conditions and the limited simulation time. The temporal dynamics of the obtained values of the diffusion coefficient and the particle mobility in the transient state depend to a great extent on the type of initial conditions. And the time limitation has an effect on the correct definition of such values as the mobility and the diffusion coefficient.

The purpose of this scientific paper was to evaluate already available methods and develop new efficient methods for the presetting of initial conditions and analyzing the solutions of stochastic Langevin equations.

BASIC RATIOS AND SIMULATION METHODS

The Langevin equation is usually used for the simulation of the motion of Brownian particles in the periodic potential exposed to the action of external fields:

$$m\ddot{X} = -\frac{d}{dx}U(X) - g\dot{X} + F(\tau) + \xi(\tau),$$ (1)

where X is the particle coordinate, m is the particle mass, τ is the time, g is the friction coefficient, and $F(\tau)$ is the external force. The dot on top denotes the time differentiation. The term $\xi(t)$ describes thermal fluctuations. The noise is a white Gaussian noise and accordingly the ratio of

$$\langle \xi(t)\xi(t') \rangle = 2gk\Theta\delta(\tau - \tau'), \tag{2}$$

where k is the Boltzmann constant and Θ is the temperature.

For the potential particle energy in the periodic potential with period L the relation of

$$U(X + L) = U(X). \tag{3}$$

is true. Henceforth, we will make use of the most frequently used type of the periodic potential, in particular

$$U(X) = -\frac{U_0}{2}\cos\left(\frac{2\pi}{L}X\right) \tag{4}$$

where U_0 is the potential barrier height.

The moving particle is exposed to the action of the periodic force exerted by the lattice F_{lat}:

$$F_{lat} = -\frac{dU}{dx} = F_0\sin\left(\frac{2\pi}{L}X\right). \tag{5}$$

The period of low natural vibrations in such a potential is equal to $\tau_0 = L(2m/U_0)^{1/2}$.

It is convenient to change over to dimensionless values to analyze the simulation data [1,19]. Let's apply the transformations:

$$x = \frac{2\pi}{L}X \quad, \quad t = \frac{\tau}{\tau_0} \quad. \tag{6}$$

By selecting mass units $m = 1$, $k = 1$, we obtain a maximum simple type of the equation (1):

$$\begin{aligned} \ddot{x} &= -\sin x - \gamma \dot{x} + f(t) + \zeta(t), \\ \langle \zeta(t)\zeta(t') \rangle &= 2\gamma T\delta(t - t'), \end{aligned} \tag{7}$$

Dimensionless units are relating to the force through the friction coefficient and temperature as follows:

$$\gamma = G\frac{\tau_0}{2\pi m} \quad, \quad f(t) = \frac{F(t)}{F_0} \quad, \quad T = \frac{2k\Theta}{U_0} \tag{8}$$

To evaluate the extent of the thermal equilibrium of the system described by equations (7) we will use the kinetic temperature that is often used by the nonequilibrium statistical physics [20]:

$$T_{kin} = \frac{m}{k}\left\langle \Delta v^2 \right\rangle \tag{9}$$

Here, the brackets denote the ensemble averaging and $\left\langle \Delta v^2 \right\rangle = \left\langle (v - \langle v \rangle)^2 \right\rangle$ denotes the velocity variances. In the state of thermal equilibrium the kinetic temperature of the system is equal to the thermostat temperature of $T_{kin} = T$.

The particle transport will be characterized by the value of the average velocity of the particle ensemble:

$$\langle v \rangle = \int_{-\infty}^{\infty} vn(v)dv \tag{10}$$

where $n(v)$ is the normalized function of the particle velocity distribution.

To analyze diffusion processes we will use the dispersion for the particle coordinate distribution:

$$\sigma^2(t) = \left\langle \left(x(t) - \langle x(t) \rangle \right)^2 \right\rangle \tag{11}$$

Stochastic equation (7) was solved numerically for each particle using stochastic Heun algorithm [21]. The time step was equal to 0.01. The statistical ensemble averaging was carried out for the particle number of at least $N = 5 \cdot 10^4$.

ANALYZING INITIAL CONDITIONS

In order to solve equation (7) we need to preset appropriate initial conditions. These conditions should conform to the described physical situation. When exposing the particles to the action of different external fields we usually assume that these are in thermal equilibrium with the thermostat. It allows us to get rid of wrong physical inferences due to the superposition of two different processes, in particular thermalization and the external field action.

Let's consider different boundary conditions for the simplest case of $f(t) = 0$ when the external force is unavailable. The condition of

$$x(0) = 0; v(0) = 0, \tag{12}$$

is realized in the easiest way and it was used, for example, in paper [22]. In this case, curve 1 in Fig. 1 shows a change in T_{kin} in time. The diagram shows that the kinetic temperature at initial times is considerably lower than T. The system comes to the thermal equilibrium during the thermalization period. It can be seen in Fig. 2 that the drop in temperature has no strong effect on this phenomenon. Hence, after the time $t > t_{trm}$ thermalization processes will have no effect on the behavior of the particle ensemble exposed to the external force action. However, at $t < t_{trm}$ the system is artificially cooled and it fails to comply with the condition of thermal equilibrium.

Figure 1. The dependences of the kinetic temperature T_{kin} as a function of time for different initial conditions. T = 0.5 1 – initial conditions (12), 2 – initial conditions (14), 3 - initial conditions (24). $\gamma = 3 \cdot 10^{-2}$.

Figure 2. The dependences of the kinetic temperature T_{kin} as a function of time for different initial conditions. T = 0.1 1 – initial conditions (12), 2 – initial conditions (14), 3 - initial conditions (24). $\gamma = 3 \cdot 10^{-2}$.

The conditions that are frequently used are the presetting of initial velocities and the coordinates that are distributed in some physical space domain [23-24] independently of the thermostat temperature. Fig. 3 shows a change of T_{kin} in time for the case when the initial coordinates and velocities are uniformly distributed as:

$$\begin{aligned} x(0) &= Unif(0, 2\pi), \\ v(0) &= Unif(-1.0, 1.0), \end{aligned} \tag{13}$$

where $Unif(a,b)$ is the uniformly distributed random value in the interval from a to b.

The curves 1 and 2 correspond to the thermostat temperatures of $T = 0.1$ and $T = 0.5$, accordingly. The Figure shows that in both cases T_{kin} exceeds the thermostat temperature by several times at $t < t_{trm} \approx 30\tau$. The lower the thermostat temperature the more T_{kin} exceeds T. Hence, before the time $t < t_{trm}$ we deal with the substantially overheated system.
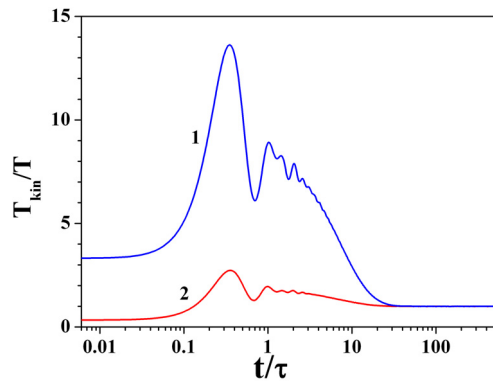
Figure 3. The dependences of the kinetic temperature T_{kin} as a function of time for initial conditions (13). $\gamma = 0.03$.
1 – T = 0.5, 2 – T = 0.1.

Most frequently, initial conditions are preset in the following manner: all the particles are organized at the origin of coordinates $x(0) = 0$, and then these are imparted initial velocities that correspond to the equilibrium Maxwell velocity distribution [25]:

$$x(0) = 0,$$
$$p(v) = \chi \exp\left(-mv^2 / (2kT)\right),$$
(14)

where χ is the normalization coefficient. In this case, in spite of the fact that the particle velocity distribution function really corresponds to the equilibrium function, the equilibrium particle coordinate distribution has not been realized. Curve 2 in Fig 1 demonstrates this fact. The value of T_{kin} is below the thermostat temperature and it oscillates with a higher amplitude before the time of t_{trm} is achieved. Fig. 2 shows that a drop in T_{kin} results in an increased oscillation amplitude of T_{kin} / T. Hence, using the initial conditions specified in (14) we also deal with the "frozen" system that is far from the equilibrium state.

It can be seen from the above that all available methods result in the strong deviation of the system from the equilibrium within t_{trm}. Hence, the use of the boundary conditions (12)-(14) requires the conduction of the thermalization procedure during the studies of transient processes when the system is exposed to the action of external fields, as it was done, for example, in scientific paper [26].

To put things right, we suggest new initial conditions that are the closest to the equilibrium for the particles in the spatially periodic potential. Under these conditions, we suggest to view the initial particle ensemble as the system of harmonic oscillators that is in the thermal equilibrium with the thermostat. Assuming that these are small-amplitude oscillations observed near the potential well bottom the harmonic oscillator motion equation can be written as:

$$\ddot{x} + \omega_0^2 x = 0 ,$$
(15)

where $\omega_0 =$ is the natural frequency of small-amplitude oscillations:

$$\omega_0^2 = \alpha ,$$
(16)

and $\alpha = \dfrac{1}{2} \dfrac{d^2 U(x)}{dx^2}$ corresponds to the potential "stiffness".

It is a well-known fact that the equation (14) has the solution

$$x(t) = A \sin\left(\omega_0 t + \varphi\right),$$
$$v(t) = \dot{x} = A\omega_0 \cos\left(\omega_0 t + \varphi\right),$$
(17)

where A is the oscillation amplitude of the oscillator. The oscillator energy is equal to

$$E = \alpha A^2 / 2.$$
(18)

In the state of heat equilibrium the particle energy distribution has the Boltzmann distribution form:

$$p(\varepsilon) = \beta \exp\left(-\frac{\varepsilon}{kT}\right), \tag{19}$$

where β is the normalization factor derived from the statement that

$$\int_0^\infty p(\varepsilon)d\varepsilon = 1, \tag{20}$$

To obtain initial particle coordinate and velocity distributions the following algorithm should be realized:
1) Using the distribution (19) we find a random energy ε for each particle that obeys the exponential distribution with the mathematical expectation equal to kT:

$$\varepsilon = -kTLn(r_1), \tag{21}$$

where r_1 is a random number uniformly distributed in the interval of $[0,1]$.
2) Using (18), we compute the oscillation amplitude value A:

$$A = \sqrt{\frac{2\varepsilon}{\alpha}}, \tag{22}$$

3) phase φ is considered equivalent to the random number r_2 that is uniformly distributed in the interval ranging from 0 to 2π:

$$\varphi = r_2, \tag{23}$$

4) Using the expression (17) at the initial moment of $t = 0$ we compute initial particle coordinate and velocity values:

$$\begin{aligned}
x(0) &= A\sin(\varphi), \\
v(0) &= A\omega_0 \cos(\varphi).
\end{aligned} \tag{24}$$

In Fig. 1-2, the curves 3 correspond to initial conditions (24). The diagrams show that initial conditions (24) are the closest to thermal system equilibrium conditions. In other words, it is preferable to use initial conditions (24) for the analysis of the systems in which the particles were in the heat equilibrium state. Fig. 4 shows the deviation from the heat equilibrium under these initial conditions for different temperatures. The Figure shows that in contrast to other initial conditions a drop in temperature results in the lessening of the deviation from the equilibrium distribution. At $T \leq 0.1$, the kinetic temperature T_{kin} differs from the thermostat temperature within 4%.
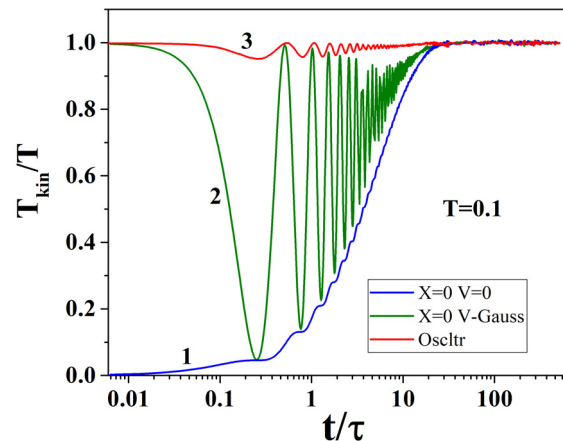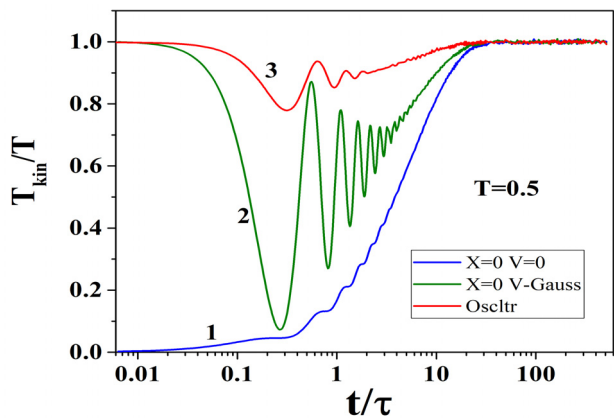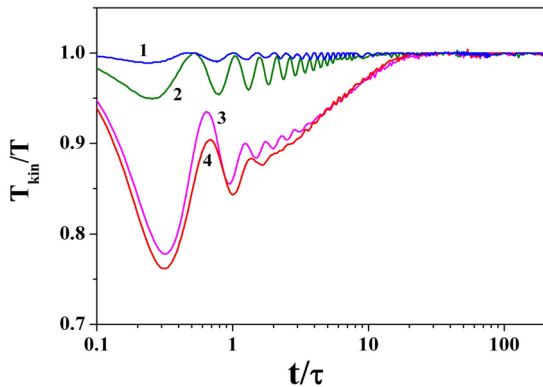

Figure 4. The dependences of the kinetic temperature T_{kin} as a function of time for different T values. Initial conditions (24). $\gamma = 0.03$. 1– T = 0.01, 2 – T = 0.1, 3 – T = 0.5, 4 – T = 1.0.
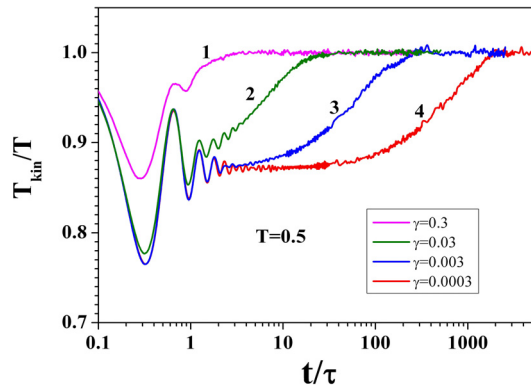
Figure 5. The dependences of the kinetic temperature T_{kin} as a function of time for different γ values. Initial conditions (24). T = 0.5. 1– $\gamma = 0.3$, 2 – $\gamma = 0.03$, 3 – $\gamma = 0.003$, 4 – $\gamma = 0.0003$.

Let's consider a change in t_{trm} depending on the dissipative properties of the system. Based on the above, since initial conditions (24) are the closest to equilibrium conditions we will confine ourselves to their studies. Fig. 5 gives a change in the value of T/T_{kin} for different values of γ. The Figure shows that the thermalization time is linearly increased with a decrease in γ. While for $\gamma = 0.3$ it is equal to $t_{trm} \approx 3$, for $\gamma = 0.0003$ it is increased to $t_{trm} \approx 3000$. Hence, the value of t_{trm} is increased as $1/\gamma$ with a decrease in the friction coefficient. The use of initial conditions (24) enables high accuracy computations using no thermalization procedure at temperatures of $T < 0.1$. Under other conditions it is recommended to carry out the thermalization procedure.

CALCULATING THE DIFFUSION COEFFICIENT

The correct computation of the diffusion coefficient D is a vital problem for many investigations. A classic method of the determination of D for computer-aided calculations consists in the direct use of the definition of the diffusion coefficient as [27-28]:

$$D = \lim_{t \to \infty} D_{ef}(t) = \lim_{t \to \infty} \frac{\sigma^2}{2t} = \lim_{t \to \infty} \frac{\left\langle \left(x - \langle x \rangle\right)^2 \right\rangle}{2t}. \tag{25}$$

A key question put in the papers highlighting computer simulations is what estimated time we should confine to? Usually, the time is selected so that the clear-cut linear dependence of $\sigma^2(t) = 2Dt$ is observed in the log-log scale, for example as for t > 10^6 in Fig. 6. This Figure gives the example of a change in the dispersion value with time under the action of the constant force [29]. Fig. 7 gives curve 2 that corresponds to the dependence of $\sigma^2(t)/t$.
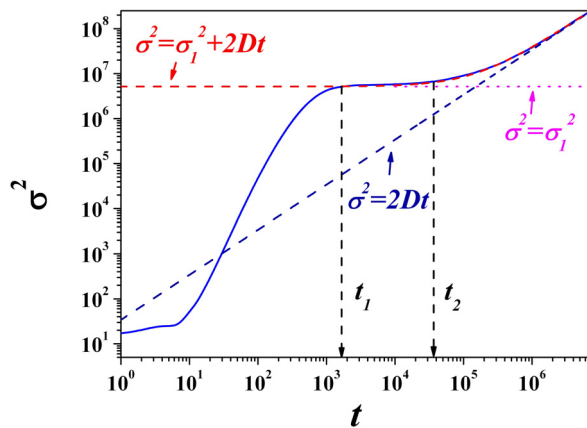
Figure 6. The dependence of the dispersion on time under the action of constant force $f = 0.25$. $\gamma = 0.3$, T = 0.5. The solid line is the simulation data. The dash-dotted line is $\sigma^2 = 2Dt$ asymptote, the dashed line shows the approximation $\sigma^2 = 2Dt + \sigma_1^2$, and the dotted line shows constant σ_1^2. The arrows show the starting and the ending time of the "dispersionless" phase.
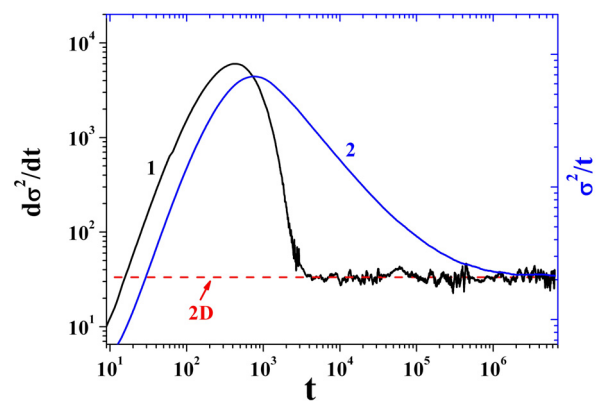
Figure 7. The dependence of $d\sigma^2 / dt$ (curve 1) and σ^2 / t (curve 2) on time. The dashed line shows the value of $2D$. $f = 0.25$, $\gamma = 0.3$, T = 0.5.

Apparently, to obtain the right value of D using the formula (25) we need time t > 10^6. As is seen from Fig. 6 the dependence of $\sigma^2(t)$ shows the presence of the horizontal "plateau" between the times t_1 and t_2. It is the so-called phase of the "dispersionless" transport [30]. With a drop in temperature the duration of it is exponentially increased [29]. It makes impossible to derive D from formula (25) during a reasonable computational time in many cases. Specifically, in paper [31] the authors failed to define the value of D in the force interval of F = 0.2-0.9. However, as is shown in [29] in spite of the formation of the exponential particle coordinate distribution in the phase of the "dispersionless" transport this phase is characterized by the ordinary diffusion with $\sigma^2(t) \propto t$. To make it more apparent, let's appeal to Fig. 7.

The Figure shows the time dependence of $d\sigma^2 / dt$. It appears that if we use the differential definition of the time-dependent diffusion coefficient $D(t)$ [32-33]

$$D(t) = \frac{1}{2} \frac{d\sigma^2}{dt}, \tag{26}$$

the mean value of $D(t)$ don't change at $t > t_1$. Only thermal fluctuations are observed near the mean value. It means that at $t > t_1$ we deal with the ordinary diffusion. For the sake of clarity let's venture into Fig. 8.

It gives the diagrams of the time dependence $\sigma^2(t)$, $T_{kin}(t)$ and $\langle v \rangle(t)$. It can be seen that the superdiffusion phase is ended at $t \approx t_1$ and the ordinary diffusion phase with $\sigma^2(t) = \sigma_1^2 + 2Dt$ is originated. As was shown in [29], the value of σ_1^2 is defined by the duration of the superdiffusion phase. The end of the superdiffusion phase is characterized by

the establishment of the stationary value $T_{kin}(t)$. In addition, a stationary distribution of $\langle v \rangle(t)$ is established at $t > t_1$. As is seen in Fig. 7 the dependence of $d\sigma^2 / dt = const$ is established at the same time. Hence, the establishment of the stationary value $T_{kin}(t)$ is indicative of the beginning of the phase of ordinary diffusion with $\sigma^2(t) \propto t$.
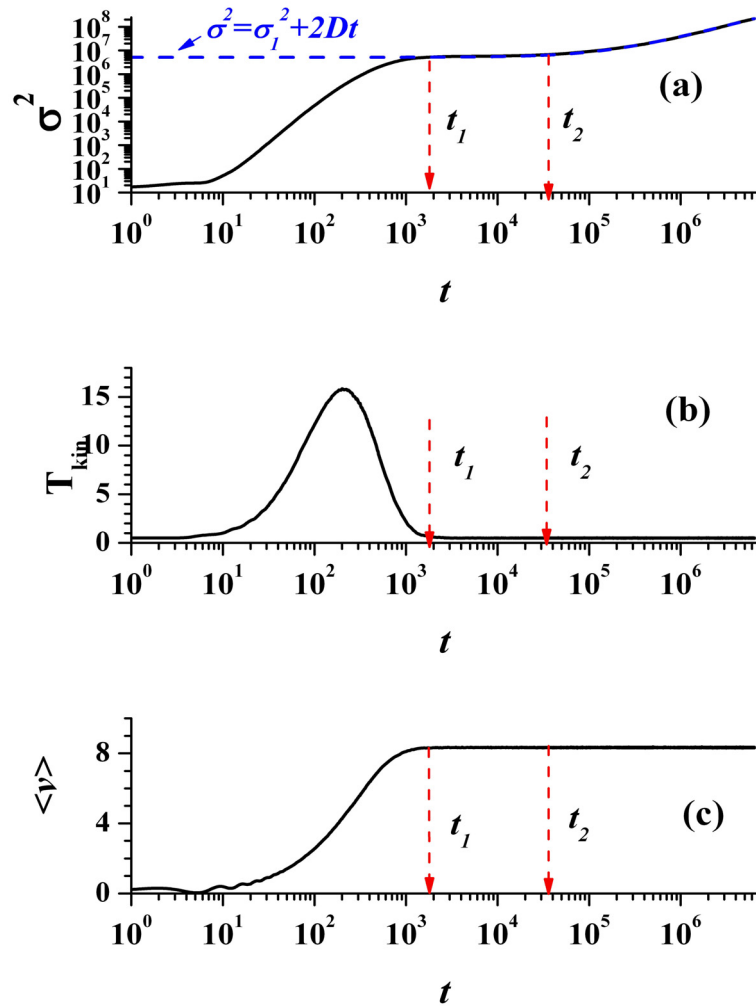
Figure 8. The dependence on time versus a) dispersion; b) the kinetic temperature; c) average velocity under the action of the constant force $f = 0.25$. $\gamma = 0.3$, T = 0.5. The dashed line shows the approximation $\sigma^2 = 2Dt + \sigma_1^2$.

As is shown above, the diffusion factor can be calculated using the time-averaged value (26) at $t > t_1$. This method has its drawbacks relating both to numerical differentiation procedure complications and the use of this method for other situations in addition to $f(t) = const$. The integral method is more stable and it enables an easy computation of the diffusion factor already during the time of the "dispersion-free" transport. It follows from the consideration given above that after the attainment of time t_1

$$\sigma^2(t) = 2Dt + \sigma_1^2, \text{ at } (t > t_1),\tag{27}$$

It was shown in [29] that σ_1^2 is exponentially increasing with the drop in temperature. Therefore, the second term in (27) will dominate over the first term for a rather long time. However, in the case of the fitting of $\sigma^2(t)$ data by the dependence (27) with free σ_1^2 and D parameters using the least square method we can obtain the diffusion factor with a high accuracy already at short times.

Let's get back to Fig. 6. Using the relation (25) for time t = 6.4·10⁶ we obtain D = 17.30. With an increase in time by one order of magnitude we get D = 17.06 at t = 6.4·10⁷. In other words, it takes a rather long time to get the diffusion coefficient with a high accuracy. Taking into consideration the exponential growth of $\Delta t = t_2 - t_1$ with a drop in

temperature [29] we can draw a conclusion that it is impossible to derive D for lower temperatures during a reasonable computational time. However, using (27) we can approximate $\sigma^2(t)$ at a considerably shorter time interval, in particular t $=1.0 \cdot 10^4$ $-5 \cdot 10^4$. Providing the $\sigma^2(t)$ data fitting using the least square method we will see that in this case the dispersion is described by the linear dependence (27) with the correlation coefficient equal to 0.999.

Using the data in this limited time interval we will get the value of D = 17.03. In other words, the use of (27) results in the reduction of the computational time by the factor of 6000 to get the same value of D as proceeding from the expression (25) for time t = $6.4 \cdot 10^7$. With the drop in temperature the required estimated time lag between (25) and (27) will be growing exponentially. And the derivation of the value D proceeding from the expression (25) becomes unrealistic. However, using the data fitting (27) the diffusion factors can easily be derived even in the cases of total previous failure. This approach can also be applied to other systems that show a considerable dispersion growth in the initial phase. However, we must be careful and confident that all the transient processes have already been completed. As an example, let's give some data for the periodic force of the type

$$f(t) = a \sin(\omega t). \tag{28}$$

Fig. 9 gives the data for one of such computations. Fig. 9b shows that at $t > 400$ the system passes into the stationary state and the yield of the stationary value by the kinetic temperature is indicative of it.
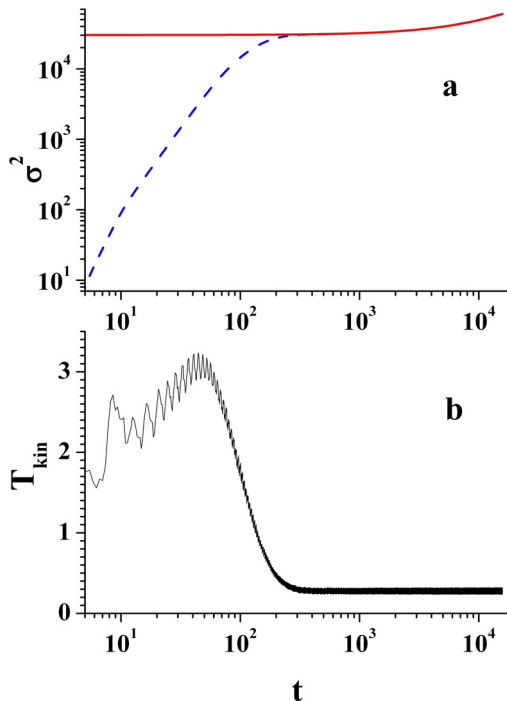
Figure 9. The dependence on time versus a) dispersion; b) the kinetic temperature under the action of periodic external force. The dashed line shows a) the simulation data, the solid line shows the linear approximation. $a = 10.0$, $\gamma = 0.318$, T = 0.2, $\omega = 1.59$.
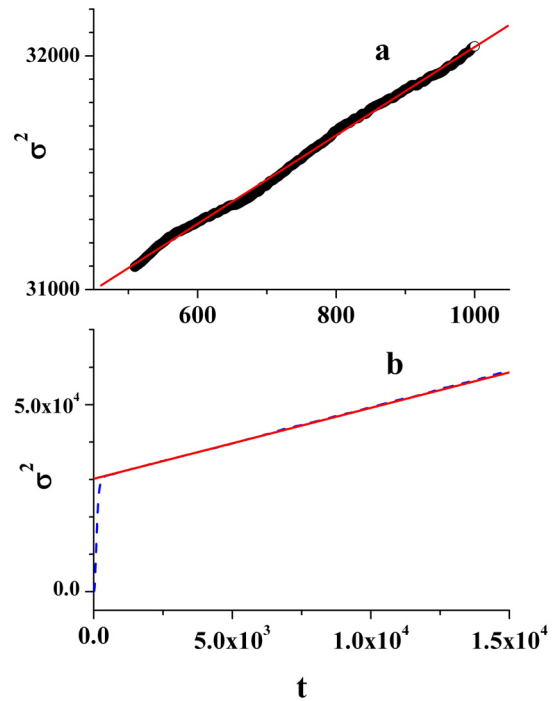
Figure 10. The dependence of σ^2 on time. a) the markers show the simulation data for the ensemble consisting of 50000 particles, the solid line is the linear approximation and the dashed line is the simulation data; b) the solid line is the linear approximation and the dashed line is the simulation data. $a = 10.0$, $\gamma = 0.318$, T = 0.2, $\omega = 1.59$.

Though, the dependence of $\sigma^2(t)$ in Fig. 9a looks like subdiffusion or "dispersionless" transport in these time intervals, however in reality the ordinary diffusion takes place at $t > 400$ as is well seen in Fig. 10b.

In Fig. 10a, the simulation data of the ensemble consisting of 50000 particles are shown by the markers. The solid line shows the linear approximation of these data. The least square method was used for the approximation [34]. Fig. 9a and Fig. 10b show that the linear approximation approximates well the dependence of $\sigma^2(t)$ at $t > 500$ in the limited linear section of Fig. 10a. Fitting the data in Fig.10a by using the linear regression method, we obtain the linear relationship with a correlation coefficient of 0.998. Using the data in the interval of $500 < t < 5000$ we increase the correlation coefficient value to 0.9998. It allows us to derive the diffusion coefficient with a high degree of confidence as 1/2 of the slope at a significantly reduced computational time in comparison to that spent using the classic method.

The abovementioned method used for the derivation of the diffusion coefficient was successfully used by us earlier [35-36]. Therefore, it can be recommended for a wide application by other systems.

CONCLUSIONS

This paper delves into the studies of the specific features of the simulation of the diffusion processes of particles in spatially periodic potentials using Langevin equations. Different methods used for the presetting of initial conditions and their effects on obtained solutions have been analyzed. It was shown that the system is nonequilibrium for all the methods used for the presetting of initial conditions during a certain time interval of t_{trm}. This interval in increased as $1/\gamma$ with a decrease in the friction coefficient. The kinetic temperature with regard to the methods used today for the presetting of initial conditions differs from the thermostat temperature by tens of percent. Hence, the adequate description of the transient particle transport and diffusion processes exposed to the action of external fields requires a preliminary system thermalization procedure during the time of at least t_{trm}.

A new method of the presetting of initial conditions under which the system is close to the thermal equilibrium has been suggested. It consists in the generation of the initial particle coordinates and velocities that correspond to the equilibrium distribution of harmonic oscillators at a specified temperature. The use of these initial conditions enables the computations using no thermalization procedure at the temperature of T < 0.1 with the error less than 4%.

A classic method of the computation of diffusion coefficients D as a limit $\lim_{t\to\infty}\left(\sigma^2/2t\right)$ has been analyzed. It was shown that the use of it for computer-aided calculations is limited by the restricted computational time. It makes the computation of D impossible under certain conditions. A new method was suggested for the determination of the diffusion coefficient through the linear approximation of the dispersion versus time dependence. This approximation is only possible after the kinetic temperature attains its stationary value. The proposed method requires several orders of magnitude less time in comparison to the classic method. As a result, it enables the computation of the diffusion coefficient even in the cases of total previous failure.

The obtained data are important for the proper simulation computations of diffusion processes and for the correct physical interpretation of obtained results.

ORCID IDs
Viktoriia Yu. Aksenova, https://orcid.org/0000-0003-4231-7463; **Ivan G. Marchenko**, https://orcid.org/0000-0003-1341-4950
Igor I. Marchenko, https://orcid.org/0000-0002-3071-9169

REFERENCES
[1]   H. Risken, *The Fokker-Planck Equation and Methods of Solution and Applications* (Springer, 1989), pp. 485.
[2]   P. Hänggi, F. Marchesoni, Rev. Mod. Phys. **81,** 287 (2009), https://doi.org/10.1103/RevModPhys.81.387
[3]   R.H. Koch, and D.J. Van Harlingen, J. Clarke, Phys. Rev. B **26**, 74 (1982), https://doi.org/10.1103/PhysRevB.26.74
[4]   K. Siraj, Past, International Journal of Nano and Material Sciences, **1**, 1 (2012), https://bit.ly/3rXzTO1
[5]   M. Beck, E. Goldobin, M. Neuhaus, M. Siegel, R. Kleiner, and D. Koelle, Phys. Rev. Lett. **95**, 090603 (2005), https://doi.org/10.1103/PhysRevLett.95.090603
[6]   G. Grüner, A. Zawadowski, and P.M. Chaikin, Phys. Rev. Lett. **46**, 511 (1981), https://doi.org/10.1103/PhysRevLett.46.511
[7]   P. Tierno, P. Reiman, T.H. Johansen, and F. Sagués, Phys. Rev. Let. **105**, 230602 (2010), https://doi.org/10.1103/PhysRevLett.105.230602
[8]   P. Eshuis, K. van der Weele, D. Lohse, and D. van der Meer, Phys. Rev. Let. **104**, 248001 (2010), https://doi.org/10.1103/PhysRevLett.104.248001
[9]   M. Zarshenas, V. Gervilla, D.G. Sangiovanni, and K. Sarakinos, Phys. Chem. Chem. Phys. **23**, 13087 (2021), https://doi.org/10.1039/D1CP00522G
[10]   S.-H. Lee, and D.G. Grier, Phys. Rev. Let. **96**, 190601 (2006), https://doi.org/10.1103/PhysRevLett.96.190601
[11]   S. Pagliara, C. Schwall, and U.F. Keyser, Advanc. Mat. **25**, 844 (2013), https://doi.org/10.1002/adma.201203500
[12]   P. Reimann, C. Van den Broeck, H. Linke, P. Hänggi, J.M. Rubí, and A. Pérez-Madrid, Phys. Rev. E **65**, 031104 (2002), https://doi.org/10.1103/PhysRevE.65.031104
[13]   R. Salgado-García, Phys. Rev. E **90**, 032105 (2014), https://doi.org/10.1103/PhysRevE.90.032105
[14]   G. Costantini, and F. Marchesoni, Europhys. Lett. **48**, 491 (1999), https://doi.org/10.1209/epl/i1999-00510-7
[15]   J.M. Sancho, A.M. Lacasta, K. Lindenberg, I.M. Sokolov, and A.H. Romero, Phys. Rev. Lett. **92**, 250601 (2004), https://doi.org/10.1103/PhysRevLett.92.250601
[16]   B. Lindner, and I.M. Sokolov, Phys. Rev. **E93**, 042106 (2016), https://doi.org/10.1103/PhysRevE.93.042106
[17]   J. Spiechowicz, and J. Łuczka, Phys. Rev. E **104**, 034104 (2021), https://doi.org/10.1103/PhysRevE.104.034104
[18]   I.G. Marchenko, I.I. Marchenko, and V.I. Tkachenko, JETP Letters **109** №**10**, 671 (2019), https://doi.org/10.1134/S0021364019100126
[19]   J. Spiechowicz, and J. Łuczka, Phys. Rev. E **101**, 032123 (2020), https://doi.org/10.1103/PhysRevE.101.032123
[20]   P. Siegle, I. Goychuk, and P. Hänggi Phys. Rev. Lett. **105,** 100602 (2010), https://doi.org/10.1103/PhysRevLett.105.100602
[21]   D. Garcia-Alvarez, arXiv:1102.4401v1 [physics.comp-ph] (2011), https://doi.org/10.48550/arXiv.1102.4401
[22]   A.M. Lacasta, J.M. Sancho, A.H. Romero, I.M. Sokolov, and K. Lindenberg, Phys. Rev. E **70**, 051104 (2004), https://doi.org/10.1103/PhysRevE.70.051104
[23]   J. Spiechowicz, P Talkner, P Hänggi, and J. Luczka, New J. Phys. **18,** 123029 (2016), https://doi.org/10.1088/1367-2630/aa529f

[24] J. Spiechowicz, M. Kostur, and J. Łuczka, Chaos **27**, 023111 (2017), https://doi.org/10.1063/1.4976586
[25] I. Goychuk, Phys. Rev. Lett. **123**, 180603 (2019), https://doi.org/10.1103/PhysRevLett.123.180603
[26] I.G. Marchenko, I.I. Marchenko, and A.V. Zhiglo, Phys. Rev. E **97,** 012121 (2018), https://doi.org/10.1103/PhysRevE.97.012121
[27] B. Lindner, M. Kostur, and L. Schimansky-Geier, Fluctuation and Noise Letters **01 №01**, R25 (2001), https://doi.org/10.1142/S0219477501000056
[28] D. Speer, R. Eichhorn, and P. Reimann, EPL **97**, 60004 (2012), https://doi.org/10.1209/0295-5075/97/60004
[29] I.G. Marchenko, V.Yu. Aksenova, I.I. Marchenko, and A.V. Zhiglo, J. Phys. A: Math. Theor. **55,** 155005 (2022), https://doi.org/10.1088/1751-8121/ac57d1
[30] K. Lindenberg, J.M. Sancho, A.M. Lacasta, and I.M. Sokolov, Phys. Rev. Lett. **98**, 020602 (2007), https://doi.org/10.1103/PhysRevLett.98.020602
[31] J.M. Sancho, and A.M. Lacasta, Eur. Phys. J. Special Topics **187**, 49 (2010), https://doi.org/10.1140/epjst/e2010-01270-7
[32] R.D.L. Hanes, M. Schmiedeberg, and S.U. Egelhaaf, Phys. Rev. E **88**, 062133 (2013), https://doi.org/10.1103/PhysRevE.88.062133
[33] F. Evers, C. Zunke, R.D.L. Hanes, J. Bewerunge, and I. Ladadwa, Phys. Rev. E **88**, 022125 (2013), https://doi.org/10.1103/PhysRevE.88.022125
[34] J. Wolberg, *Data Analysis Using the Method of Least Squares: Extracting the Most Information from Experiments* (Springer, 2005), p. 250.
[35] I.G. Marchenko, V.Yu. Aksenova, and I.I. Marchenko, East Eur. J. Phys. **3,** 27 (2021), https://doi.org/10.26565/2312-4334-2021-3-03
[36] I.G. Marchenko, I.I. Marchenko, and V.I. Tkachenko, JETP Letters **109** №10, 694 (2019), https://doi.org/10.1134/S0021364019100126

ОСОБЛИВОСТІ МОДЕЛЮВАННЯ ПРОЦЕСІВ ДИФУЗІЇ ЧАСТИНОК У ПРОСТОРОВО-ПЕРІОДИЧНИХ ПОЛЯХ

В.Ю. Аксенова[a,b]**, І.Г. Марченко**[a,b]**, І.І. Марченко**[c]
ᵃХарківський національний університет імені В.Н. Каразіна
м. Свободи 4, м. Харків, 61022, Україна
ᵇНаціональний науковий центр «Харківський фізико-технічний інститут»
вул. Академічна, 1, м. Харків 61108, Україна
ᶜНТУ «Харківський політехнічний інститут»
вул. Кирпичова, 2, м. Харків 61002, Україна

Робота присвячена дослідженню особливостей моделювання процесів дифузії частинок у просторово-періодичних потенціалах за допомогою рівнянь Ланжевена. Проаналізовані різні методи завдання початкових умов та їхній вплив на отримані рішення. Показано, що при всіх способах завдання початкових умов система є нерівноваженою протягом деякого интервалу часу t_{trm}. Цей інтервал збільшується зі зменшенням коефіцієнту тертя як $1/\gamma$. Для адекватного опису перехідних процесів дифузії та транспорту необхідно заздалегідь проводити процедуру термалізації системи. Запропоновано новий метод завдання початкових умов, який найбільш близько описує врівноважену систему. Він полягає в генерації початкових координат та швидкостей частинок, які відповідають врівноваженому розподілу гармонійних осциляторів із даною температурою. Використання таких початкових умов дозволяє з високою точністю проводити обчислення без використання процедури термалізації при температурах $T < 0.1$. Проаналізований класичний метод визначення коефіцієнтів дифузії D як границі $\lim_{t\to\infty}(\sigma^2/2t)$. Показано, що його застосування у комп'ютерних розрахунках лімітовано обмеженим часом розрахунків. Це призводить до неможливості обчислення D в деяких умовах. Запропоновано новий метод визначення коефіцієнта дифузії за лінійною апроксимацією залежності дисперсії від часу. Така апроксимація можлива тільки після того, як кінетична температура досягла свого стаціонарного значення. Запропонований метод потребує на декілька порядків менше розрахункового часу, ніж класичний метод. Внаслідок цього він дозволяє обчислювати коефіцієнт дифузії навіть у тих випадках, у яких раніше це не вдавалося. Отримані результати важливі для коректного проведення моделюючих розрахунків процесів дифузії та вірної фізичної інтерпретації отриманих результатів.
Ключові слова: дифузія, зовнішні поля, комп'ютерне моделюрування, початкові умови, рівняння Ланжевена.

QUARK-ANTIQUARK STUDY WITH INVERSELY QUADRATIC YUKAWA POTENTIAL USING THE NIKIFOROV-UVAROV-FUNCTIONAL-ANALYSIS METHOD†

Etido P. Inyang[a,b]*, Prince C. Iwuji[b], Joseph E. Ntibi[b], E. Omugbe[c],
Efiong A. Ibanga[a], Eddy S. William[b]

aDepartment of Physics, National Open University of Nigeria, Jabi-Abuja, Nigeria
bTheoretical Physics Group, Department of Physics, University of Calabar, P.M.B 1115 Calabar, Nigeria
cDepartment of Physics, Federal University of Petroleum Resources, Effurun, Delta State, Nigeria
**Corresponding Author: etidophysics@gmail.com, einyang@noun.edu.ng*

The solutions of the Schrödinger equation are obtained with an inversely quadratic Yukawa potential using the Nikiforov-Uvarov-Functional-analysis method. The energy spectrum and wave function were obtained in closed form. The energy equation was used to predict the masses of the heavy mesons such as charmonium ($c\bar{c}$) and bottomonium ($b\bar{b}$) for different quantum numbers. The results obtained agreed with other theoretical predictions and experimental data with a percentage error of 1.68 % and 0.50 % for charmonium ($c\bar{c}$) and bottomonium ($b\bar{b}$) respectively.
Keywords: Schrödinger equation; Nikiforov-Uvarov-Functional-analysis method; inversely quadratic Yukawa potential; heavy mesons
PACS: 12.39.Jh

The solutions of the Schrodinger equation (SE) with spherically symmetric potentials are of foremost concern in describing the mass spectra (MS) of the heavy mesons (HMs) such as bottomonium ($b\bar{b}$), and charmonium ($c\bar{c}$) [1-3]. In describing this system an interaction potential is used to simulate the system. The Cornell potential (CP) which includes a short-range Coulomb term and a linear confinement term is generally used [4]. More so, in solving this SE with any chosen potential, an analytical method is employed, such as, the Nikiforov-Uvarov (NU) method [5-8], the NU Functional Analysis (NUFA) method [9,10], the series expansion method (SEM) [11], Laplace transformation method (LTM) [12], WKB approximation method [13], exact quantization rule [14,15], proper quantization rule [16,17], group theory approach [18] and so on [19]. The study of MS with CP has gained remarkable attention and has attracted the attention of many scholars [20-23]. For instance, Kumar et al. [24] used the NUFA method to solve the SE with generalized Cornell potential. The result was used to determine the MS of the HMs. Using the vibrational method (VM) and supersymmetric quantum mechanics, Vega and Flores, [25] obtained the analytical solutions of the SE with CP. The eigenvalues were used to calculate the MS of the HMs. Also, Mutuk [26] solved the SE with CP using a neural network approach. The bottomonium, charmonium, and bottom-charmed spin-averaged spectra were calculated. Furthermore, Hassanabadi et al. [27], used the VM to solve the SE with CP. The eigenvalues were used to calculate the mesonic wave function. In recent times, the study of MS of the HMs with exponential-type potentials has aroused the interest of scholars [28,29]. Potential models such as Yukawa potential [30], Varshni [31], screened Kratzer potential [32], Hulthen plus Hellmann potential [33], and so on [34] have been used in the prediction of the MS of the HMs. For instance, Purohit et al [35] combined linear plus modified Yukawa potential to obtain the masses of the HMs. Also, Al-Jamel [36], studied the MS with Coulomb plus inverse quadratic term. It was found that the MS exhibit a saturation effect. Furthermore, in 2019 Al-Jamel, solved the SE with a combination of a cotangent with a square co-secant function using the NU method. The energy equation was used to predict the MS of heavy quarkonia [37].

The SE for most of the potentials with spin addition cannot be solved analytically; hence, numerical solutions such as Runge-Kutte approximation [38], Numerov matrix method [39], Fourier grid Hamiltonian method [40], and so on [41] are employed. Also, adding spin enables one to determine other properties of the mesons like decay properties and root mean square radii. However, we have considered our mesons as spinless particles for easiness [1, 25, 42-44]. The potential of interest is the inversely quadratic Yukawa potential (IQYP) suggested by Hamzavi et al [45]. The IQYP is a short-range potential, Onate [46] studied the Klein Gordon equation and SE with the IQYP. Since then, researchers have carried out many studies on relativistic and non-relativistic regimes with this potential [47-49]. The potential model is of the form [45]:

$$V(r) = -\frac{pe^{-2\theta r}}{r^2},\qquad(1)$$

where p is potential strength and θ is the screening parameter.

To the best of our knowledge, no report has been made in the literature using this potential to predict the MS of the HMs, hence this study.

This study aims to solve the SE with IQYP, using a newly proposed method called the NUFA method. The obtained energy equation will be used to predict the MS of the HMs. This paper is organized in the following order. In section 2, the solutions of the SE with the IQYP are presented. In section 3, the results and discussion are presented. Finally, the conclusion is presented in section 4.

THE SOLUTIONS OF THE SE WITH IQYP

The SE reads [50]

$$\frac{d^2\psi(r)}{dr^2} + \left[\frac{2\mu}{\hbar^2}\left(E_{nl} - V(r)\right) - \frac{l(l+1)}{r^2}\right]\psi(r) = 0,$$ (2)

where $\psi(r)$ is the eigenfunctions, E_{nl} is the energy eigenvalues, μ is the reduced mass of the system, $\hbar$ is the reduced Planck's constant and r is the inter-nuclear separation.

The exponential term in Eq. (1) is subjected to series expansion, to model the potential to interact in the quark-antiquark system, this yields:

$$V(r) = \frac{A}{r^2} - \frac{B}{r} + Cr - D.$$ (3)

where

$$\left.\begin{array}{l} A = -p, \ B = 2\theta p \\ C = -1.33p\theta^3, \ D = 2p\theta^2 \end{array}\right\}$$ (4)

Plugging Eq. (3) into Eq. (2) gives

$$\frac{d^2\psi(r)}{dr^2} + \left[\frac{2\mu}{\hbar^2}\left(E_{nl} - \frac{A}{r^2} + \frac{B}{r} - Cr + D\right) - \frac{l(l+1)}{r^2}\right]\psi(r) = 0.$$ (5)

To solve Eq. (5), we introduced the Greene-Aldrich approximation to deal with the inverse square term, valid for small screening parameter values [51-54].

$$\frac{1}{r^2} \approx \frac{\theta^2}{\left(1 - e^{-\theta r}\right)^2}.$$ (6)

Substituting Eqs. (6) into Eq.(5), gives Eq.(7) as

$$\frac{d^2\psi(r)}{dr^2} + \left[\frac{2\mu}{\hbar^2}\left(E_{nl} - \frac{A\theta^2}{\left(1-e^{-\theta r}\right)^2} + \frac{B\theta}{\left(1-e^{-\theta r}\right)} - C\frac{\left(1-e^{-\theta r}\right)}{\theta} - D\right) - \frac{l(l+1)\theta^2}{\left(1-e^{-\theta r}\right)^2}\right]\psi(r) = 0.$$ (7)

Transmuting the coordinate of Eq. (7), we set, $y = e^{-\theta r}$ and Eq. (7) is rewritten as follows:

$$\frac{d^2\psi(y)}{dy^2} + \frac{1-y}{y(1-y)}\frac{d\psi(y)}{dy} + \frac{1}{y^2(1-y)^2}\left[-\varepsilon(1-y)^2 - \chi_0 + \chi_1(1-y) - \chi_2(1-y)^3 - \gamma\right]\psi(y) = 0,$$ (8)

where

$$\left.\begin{array}{l} -\varepsilon = \dfrac{2\mu E_{nl}}{\theta^2\hbar^2} + \dfrac{2\mu D}{\theta^2\hbar^2}, \quad \chi_0 = \dfrac{2\mu A}{\hbar^2}, \\ \chi_1 = \dfrac{2\mu B}{\theta\hbar^2}, \quad \chi_2 = \dfrac{2\mu C}{\theta^3\hbar^2}, \quad \gamma = l(l+1) \end{array}\right\}.$$ (9)

Expanding Eq. (8) and neglecting higher degree polynomials of y greater than two [55], we have

$$\frac{d^2\psi(y)}{dy^2}+\frac{1-y}{y(1-y)}\frac{d\psi(y)}{dy}+\frac{1}{y^2(1-y)^2}\left[\begin{array}{c}-(\varepsilon+3\chi_2)y^2\\+(2\varepsilon-\chi_1+3\chi_2)y-(\varepsilon+\chi_0-\chi_1+\chi_2+\gamma)\end{array}\right]\psi(y)=0, \tag{10}$$

Linking Eq. (10) and Eq. (A2), gives the following:

$$\beta_1=\beta_2=\beta_3=1,\xi_1=\varepsilon+3\chi_2,\xi_2=2\varepsilon-\chi_1+3\chi_2,\xi_3=\varepsilon+\chi_0-\chi_1+\chi_2+\gamma\}. \tag{11}$$

Inserting Eq. (11) into Eqs. (A8) and (A9), gives

$$\lambda=\frac{1}{2}\sqrt{4(\varepsilon+\chi_0-\chi_1+\chi_2+\gamma)}, \tag{12}$$

and

$$v=\frac{1+\sqrt{1+4(\chi_0+\gamma)}}{2}. \tag{13}$$

Substituting Eqs. (4), (9), (12), and (13) in Eq. (A11), we obtain the energy spectrum of the IQYP as

$$E_{nl}=-2p\theta^2-\frac{4\mu p^2\theta^2/2\hbar^2}{\left[n+\frac{1}{2}+\sqrt{\left(l+\frac{1}{2}\right)^2-\frac{2\mu p}{\hbar^2}-\frac{2.66\mu p\theta^3}{\hbar^2}}\right]^2}. \tag{14}$$

Inserting Eq. (11) into Eq. (A12) the corresponding un-normalized wave function is given as

$$\psi(y)=N_y\frac{\sqrt{4(\varepsilon+\chi_0-\chi_1+\chi_2+\gamma)}}{2}(1-y)\frac{1+\sqrt{1+4(\chi_0+\gamma)}}{2}\,_2F_1(a,b,c;y), \tag{15}$$

where,

$$a=\frac{1}{2}\sqrt{4(\varepsilon+\chi_0-\chi_1+\chi_2+\gamma)}+\frac{1+\sqrt{1+4(\chi_0+\gamma)}}{2}+\sqrt{\varepsilon+3\chi_2}, \tag{16}$$

$$b=\frac{1}{2}\sqrt{4(\varepsilon+\chi_0-\chi_1+\chi_2+\gamma)}+\frac{1+\sqrt{1+4(\chi_0+\gamma)}}{2}-\sqrt{\varepsilon+3\chi_2}, \tag{17}$$

$$c=1+\sqrt{4(\varepsilon+\chi_0-\chi_1+\chi_2+\gamma)}. \tag{18}$$

RESULTS AND DISCUSSION

The prediction of the MS of bottomonium and charmonium is carried out using the relation [56,57]

$$M=2m+E_{nl} \tag{19}$$

where m is quark-antiquark mass and E_{nl} is eigenvalues.

Putting Eq. (14) into Eq. (19) gives

$$M=2m-2p\theta^2-\frac{4\mu p^2\theta^2/2\hbar^2}{\left[n+\frac{1}{2}+\sqrt{\left(l+\frac{1}{2}\right)^2-\frac{2\mu p}{\hbar^2}-\frac{2.66\mu p\theta^3}{\hbar^2}}\right]^2}. \tag{20}$$

The reduced mass (RM) is defined as $\mu=\frac{m}{2}$. For bottomonium and charmonium, the numerical values are

$m_b=4.823\,GeV$ and $m_c=1.209\,GeV$, and the corresponding RM is $\mu_b=2.4115\,GeV$ and $\mu_c=0.6045\,GeV$

correspondingly [58]. In other to obtain the potential parameters. Equation 20 is fitted with experimental data (ED). The ED is taken from Ref. [59].

We observed that the results obtained from the prediction of MS of charmonium and bottomonium for different quantum states are in agreement with ED and other theoretical predictions with different analytical methods as shown in Tables 1 and 2.

Table 1. Mass spectra of charmonium in (GeV) (m_c =1.209 GeV, μ = 0.6045 GeV, $\theta = 0.05$, p = - 234.2385 GeV, $\hbar = 1$)

State	Present work [NUFA]	AIM [1]	NU [57]	SEM [32]	Experiment [59]	Absolute Relative deviation (ARD)
1S	3.096	3.096	3.096	3.095922	3.096	0.000
2S	3.686	3.686	3.686	3.685893	3.686	0.000
1P	3.327	3.214	3.433	-	3.525	0.198
2P	3.774	3.773	3.910	3.756506	3.773	0.001
3S	4.140	4.275	3.984	4.322881	4.040	0.100
4S	4.364	4.865	4.150	4.989406	4.263	0.101
1D	3.761	3.412	3.767	-	3.770	0.009
2D	4.058	-	-	-	4.159	0.101

Table 2. Mass spectra of bottomonium in (GeV) (m_b = 4.823 GeV, μ = 2.4115 GeV, p = -333.87617, GeV, $\theta = 0.05$, $\hbar = 1$)

State	Present work[NUFA]	AIM [1]	NU[57]	SEM[32]	Experiment [59]	Absolute Relative deviation (ARD)
1S	9.460	9.460	9.460	9.515194	9.460	0.000
2S	10.023	10.023	10.023	10.01801	10.023	0.000
1P	9.841	9.492	9.840	-	9.899	0.058
2P	10.160	10.038	10.160	10.09446	10.260	0.100
3S	10.341	10.585	10.280	10.44142	10.355	0.014
4S	10.422	11.148	10.420	10.85777	10.580	0.158
1D	10.142	9.551	10.140	-	10.164	0.022

The absolute percentage deviation in the predicted results and ED is calculated using the following relation

$$\sigma = \frac{100}{N}\sum\left|\frac{T_P - T_{EXP.}}{T_{EXP.}}\right|,$$ (21)

where $T_{EXP.}$ is the ED, T_P is the predicted results and N is the number of ED and also the percentage error is computed with the given relation [60]

$$error = \frac{\sum ARD}{\sum T_{EXP.}} \times 100\%.$$ (22)

The absolute percentage deviation was calculated using Eq. (21) and the values for charmonium and bottomonium are 1.644 *GeV* and 0.487 *GeV* respectively. Also, the percentage error (PE) of the predicted results to the experimental data, was calculated using Eq. (22) and the results show that for charmonium we have 1.68 % while that of the bottomonium is 0.50 %.
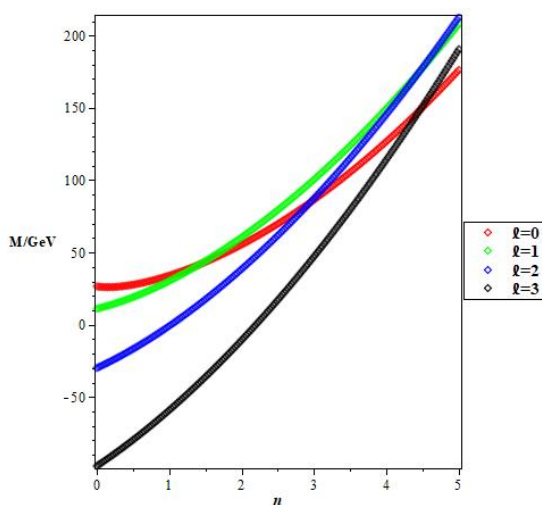

Figure 1. Mass spectra of bottomonium with a principal quantum number for a different angular quantum number
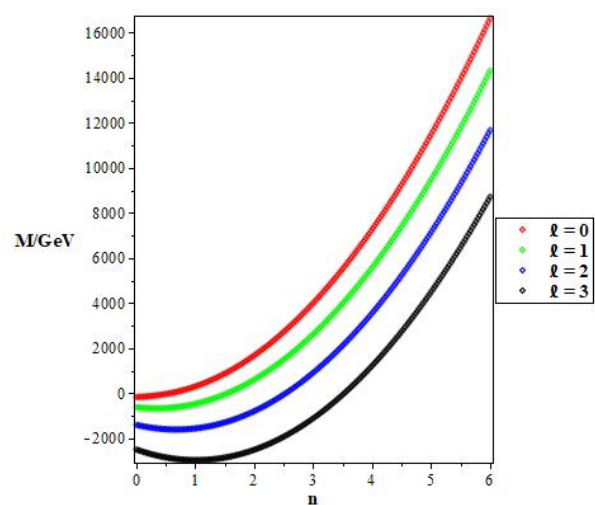
Figure 2. Mass spectra of charmonium with a principal quantum number for different angular quantum number

Figure 1 shows the variation of MS of bottomonium with a principal quantum number (PQN) for different angular quantum numbers (AQNs). It was observed that the MS increases with an increase in PQN for different AQNs which is in agreement with the ED. In Fig. 2, we plotted the MS of charmonium with PQN for different AQN. It was noticed that the MS increases as the PQN increase. This indicates that the binding energy increases with an increase in PQN.

CONCLUSION

In the present study, the solutions of the SE with IQYP using the NUFA method were solved. The energy spectrum and un-normalized wave function were obtained. The obtained energy equation was used to predict the MS of the HMs for different quantum numbers. The results obtained agreed with other predictions and with ED. The PE shows that the IQYP is fitted in the prediction of the MS of the HMs since the PE is less.

ORCID IDs

Etido P. Inyang, https://orcid.org/0000-0002-5031-3297; **Prince C. Iwuji,** https://orcid.org/0000-0001-5715-9336
Joseph E. Ntibi, https://orcid.org/0000-0002-7908-2840

REFERENCES

[1]   H. Ciftci & H.F. Kisoglu, "Nonrelativistic-Arbitrary l-states of quarkonium through Asymptotic Iteration method", Advances in High Energy Physics, **2018**, 4549705 (2018), https://doi.org/10.1155/2018/4549705

[2]   H. Mutuk, "Mass Spectra and Decay constants of Heavy-light Mesons: A case study of QCD sum Rules and Quark model", Advances in High Energy Physics, **2018,** 8095653 (2018), https://doi.org/10.1155/2018/8095653

[3]   M. Allosh, Y. Mustafa, N.K. Ahmed, and A.S. Mustafa, "Ground and Excited-state mass spectra and properties of heavy-light mesons", Few-Body Syst. **62**, 26 (2021), https://doi.org/10.1007/s00601-021-01608-1

[4]   E. Omugbe, O.E. Osafile, I.B. Okon, E.P. Inyang, E.S. William, and A. Jahanshir, "Any L-state energy of the spinless Salpeter equation under the Cornell potential by the WKB Approximation method: An Application to mass spectra of mesons", Few-Body Syst. **63**, 6 (2022), https://doi.org/10.1007/s00601-021-01705-1

[5]   C.O. Edet, P.O. Amadi, M.C. Onyeaju, U.S. Okorie, R. Sever, G.J. Rampho, H.Y. Abdullah, I.H. Salih, and A.N. Ikot, "Thermal properties and magnetic susceptibility of Hellmann potential in Aharonov-Bohm (AB) Flux and magnetic fields at Zero and Finite temperature", Journal of Low-Temperature Physics, **202**, 83 (2021), https://doi.org/10.1007/s10909-020-02533-z

[6]   E. Omugbe, "Non-relativistic eigensolutions of molecular and heavy quarkonia interacting potentials via the Nikiforov-Uvarov method", Canadian Journal of Physics, **98**, 1125 (2020), https://doi.org/10.1139/cjp-2020-0039

[7]   E.S. William, E.P. Inyang, I.O. Akpan, J.A. Obu, A.N. Nwachukwu, and E.P. Inyang, "Ro-vibrational energies and expectation values of selected diatomic molecules via Varshni plus modified Kratzer potential model", Indian Journal of Physics, (2022). https://doi.org/10.1007/s12648-0222-02308-0

[8]   M. Abu-Shady, T.A. Abdel-Karim, and Y. Ezz-Alarab, "Masses and thermodynamic properties of heavy mesons in the non-relativistic quark model using the Nikiforov-Uvarov method", Journal of Egyptian Mathematical Society, **27**, 14 (2019), https://doi.org/10.1186/s42787-019-0014-0

[9]   E.P. Inyang, E.S. William, E. Omugbe, E.P. Inyang, E.A. Ibanga, F. Ayedun, I.O. Akpan, and J.E. Ntibi, "Application of Eckart-Hellmann potential to study selected diatomic molecules using Nikiforov-Uvarov-Functional analysis method", Revista Mexicana de Fisica, **68**, 14 (2022), https://rmf.smf.mx/ojs/index.php/rmf/article/view/5931/6291

[10] A.N. Ikot, U.S. Okorie, P.O. Amadi, C.O. Edet, G.J. Rampho, and R. Sever, "The Nikiforov-Uvarov –Functional Analysis (NUFA) Method: A new approach for solving exponential – Type potentials" Few-Body Systems **62**, 9 (2021), https://doi.org/10.1007/s00601-021-021-01593-5

[11] E.P. Inyang, P.C. Iwuji, J.E. Ntibi, E.S. William, and E.A. Ibanga, "Solutions of the Schrodinger equation with Hulthen –screened Kratzer potential: Application to diatomic molecules" East European Journal of Physics, **1**, 11 (2022), https://doi.org/10.26565/2312-4334-2022-2-02

[12] M. Abu-Shady, T.A. Abdel-Karim, and E.M. Khokha, "Exact solution of the N-dimensional Radial Schrödinger Equation via Laplace Transformation method with the Generalized Cornell potential", https://arxiv.org/abs/1802.02092

[13] M. Abu-shady, C.O.Edet & A.N.Ikot, "Non-relativistic Quark model under external magnetic and Aharanov-Bohm (AB) fields in the presence of Temperature-Dependent confined Cornell potential" Canadian Journal of Physics (2021), https://doi.org/10.11139/cjp-2020-0101

[14] R. Kumar, and F. Chand. "Asymptotic study to the N-dimensional Radial Schrodinger Equation for the quark-antiquark system", Communication in Theoretical Physics, **59**, 528 (2013), https://doi.org/10.1088/0253-6102/59/5/02

[15] J.P. Prasanth, K. Sebastian, and V.M. Bannur, "Revisiting Cornell potential model of the Quark-Gluon plasma", Physica A: Statistical Mechanics and its Applications, **558**, 124921 (2020), https://doi.org/10.1016/j.physa.2020.124921

[16] H.S. Chung, J. Lee, and D. Kang, "Cornel potential parameters for S-wave heavy quarkonia", Journal of the Korean physical society, **52**, 1151 (2008), https://doi.org/10.3938/jkps.52.1151

[17] R. Kumar, R.M. Singh, S.B. Bhahardivaj, R. Rani, and F. Chand, "Analytical solutions to the Schrodinger equation for generalized Cornell potential and its application to diatomic molecules and heavy mesons", Modern Physics Letter A, **37**, 2250010 (2022), https://doi.org/10.1142/S0217732322500109

[18] A. Vega, and J. Flores, "Heavy quarkonium properties from Cornell potential using the variational method and supersymmetric quantum mechanics", Pramana Journal of Physics, **87**, 73 (2016), https://doi.org/10.1007/s12043-016-1278-7

[19] H. Mutuk, "Cornell Potential: A Neural Network Approach", Advances in High Energy Physics, **22**, 3105373 (2019), https://doi.org/10.1155/2019/3105373

[20] H. Hassanabadi, M. Ghafourian, and S. Rahmani, "Study of the Heavy-Light mesons properties via the Variational method for Cornell interaction", Few-Body Systems, **57**, 249 (2016), https://doi.org/10.1007/s00601-015-1040-6

[21] M. Abu-Shady, and S.Y.Ezz-Alarab, "Trigonometric Rosen–Morse Potential as a Quark–Antiquark Interaction Potential for Meson Properties in the Non-relativistic Quark Model Using EAIM". Few-Body Systems, **60**, 66 (2019), https://doi.org/10.1007/s00601-019-1531-y

[22] M. Abu-shady, H.M. Mansour, and A.I. Ahmadov, "Dissociation of Quarkonium in Hot and Dense media in an Anisotropic plasma in the Non-relativistic Quark model", Advances in High Energy Physics, **2019**, 4785615 (2019), https://doi.org/10.1155/2019/4785615

[23] E.P. Inyang, E.P. Inyang, J. E. Ntibi, E.E. Ibekwe, and E.S. William, **"**Approximate solutions of D-dimensional Klein-Gordon equation with Yukawa potential via Nikiforov-Uvarov method", Indian Journal of Physics, 7, (2021), https://doi.org/10.1007/s12648-020-01933-x

[24] E.P. Inyang, E.P. Inyang, E.S. William, and E.E. Ibekwe, "Study on the applicability of Varshni potential to predict the mass-spectra of the Quark-Antiquark systems in a non-relativistic framework", Jordan Journal of Physics, **14**, 339 (2021), https://doi.org/10.47011/14.4.8

[25] E.E. Ibekwe, U.S. Okorie, J.B. Emah, E.P. Inyang, and S.A. Ekong, "Mass spectrum of heavy quarkonium for screened Kratzer potential (SKP) using series expansion method, European Physical Journal Plus, **87**, 11 (2021), https://doi.org/10.1140/epjp/s13360-021-01090-y

[26] E.P. Inyang, I.O. Akpan, E.P. Inyang, and E.S. William, "Approximate solutions of the Schrödinger equation with Hulthen-Hellmann Potentials for a Quarkonium system", Revista Mexicana de Física, **67**, 490 (2021), https://doi.org/10.31349/RevMexFis.67.482

[27] M. Abu-shady, and M. Rashdan, "Effect of a logarithmic mesonic potential on nucleon properties in the Coherent-pair approximation", Physical Review C, 81, 015203 (2010), https://doi.org/10.1103/PhysRevC.81.015203

[28] K.R. Purohit, P. Jakhad, and A.K. Rai, "Quarkonium spectroscopy of the linear plus modified Yukawa potential", Physica Scripta, **97**, 044002 (2022), https://doi.org/10.1088/1402-4896/ac5bc2

[29] A. Al-Jamel, "Saturation in heavy quarkonia spectra with energy-dependent confining potential in *N*-dimensional space", Modern Physics Letters, **33**, 1850185 (2018), https://doi.org/10.1142/S0217732318501857

[30] A. Al-Jamel, Heavy quarkonia properties from a hard-wall confinement potential model with conformal symmetry perturbing effects, Modern Physics Letters, **37**, 1950307 (2019), https://doi.org/10.1142/S0217732319503073

[31] S. Patel, P.C. Vinodkumar, and S. Bhatnagar," Decay rates of charmonia within a quark-antiquark confining potential", Chinese Physics C, **40**, 053102 (2016), https://doi.org/10.1088/1674-1137/40/5/053102

[32] V. Mateu, P.G. Ortega, D.R. Entem, and F. Fernandez, "Calibrating the naïve Cornell model with NRQCD", The European Physical Journal C, **79**, 323 (2019), https://doi.org/10.1140/epjc/s10052-019-6808-2

[33] F. Brau, and C. Sernay, "The three-dimensional Fourier grid Hamiltonian method", Journal of computational physics, **139**, 136 (1998), https://doi.org/10.1006/jcph.1997.5866

[34] A. Bhaghyesh, "Charmonium properties using the Discrete variable representation (DVR) method", Advances in High Energy Physics, **2021**, 9991152 (2021), https://doi.org//10.1155/2021/9991152

[35] S. Jacobs, M.G. Olsson, and C. Suchyta, "Comparing the Schrodinger and Spinless Salpeter equations for heavy-quark bound states", Physical Review D, **33**, 3348 (1986), https://doi.org/10.1103/PHYSREVD.33.3338

[36] B. Grinstein, "A modern introduction to quarkonium theory", International Journal of Modern Physics, **15**, 461 (2000), https://doi.org/10.1142/S0217751X00000227

[37] W. Lucha, F. Schoberl, and D. Gromes, "Bound states of quarks", Physics Reports, **200**, 127 (1991), https://doi.org/10.1016/0370-1573(91)90001-3

[38] M. Hamzavi, S.M. Ikhdair, and B.I. Ita, "Approximate spin and pseudospin solutions to the Dirac equation for the inversely quadratic Yukawa potential and Tensor interaction", Physica Scripta, **85**, 45 (2012), https://dx.doi.org/10.1088/0031-8949/85/04/045009

[39] C.A. Onate, "Relativistic and Non-relativistic solutions of the inversely Quadratic Yukawa potential", African Review Physics, **8**, 46 (2013), http://eprints.lmu.edu.ng/1595/1/ONATE%2033.pdf

[40] R. Horchani, H. Al-Aamri, N. Al-Kindi, A.N. Ikot, U.S. Okorie, G.J. Rampho, and H. Jelassi, "Energy spectra and magnetic properties of diatomic molecules in the presence of magnetic and AB fields with the inversely quadratic Yukawa potential", The European Physical Journal D, **75**, 36 (2021), https://doi.org/10.1140/epjd/s10053-021-00038-2

[41] L. Hitler, B.I. Ita, N. Nzeata-Ibe, I.Joseph, O. Ivan, and T.O. Magu, "WKB Solutions for Inversely Quadratic Yukawa plus Inversely Quadratic Hellmann Potential", World Journal of Applied Physics, **7**, 109 (2017), https://article.sciencepublishinggroup.com/pdf/10.11648.j.wjap.20170204.13.pdf

[42] C.O. Edet, and P.O. Okoi, "Any *l*-state solutions of the Schrodinger equation for *q*-deformed Hulthen plus generalized inverse quadratic Yukawa potential in arbitrary dimensions", Revista Mexicana De Física, **65**, 333 (2019), https://doi.org/10.31349/RevMexFis.65.333

[43] E.P. Inyang, E.S. William, and J.A .Obu, "Eigensolutions of the N-dimensional Schrödinger equation` interacting with Varshni-Hulthen potential model", Revista Mexicana De Física, **67**, 193 (2021), https://doi.org/10.31349/RevMexFis.67.193

[44] R.L. Greene, and C.Aldrich, "Variational wave functions for a screened Coulomb potential", Physical Review A, 14, 2363 (1976), https://doi.org/10.1103/PhysRevA.14.2363

[45] C.S. Jia, T. Chen, and S. He, "Bound state solutions of the Klein–Gordon equation with the improved expression of the Manning–Rosen potential energy model", Physics Letters A, **377**, 682 (2013), https://doi.org/10.1016/j.physleta.2013.01.016

[46] C.S. Jia, J.W. Dai, L.H. Zhang, J.Y. Liu, and X.L. Peng, "Relativistic energies for diatomic molecule nucleus motions with the spin symmetry", Physics Letter A, **379**, 137 (2015), https://doi.org/10.1016/j.physleta.2014.10.034

[47] X.T. Hu, L.H. Zhang, and C.S. Jia, "D-dimensional energies for Lithium dimer", Journal of Molecular Spectroscopy, **297**, 21 (2014), https://doi.org/10.1016/j.jms.2014.01.001

[48] V. Kumar, R.M. Singh, S.B. Bhardwaj, and F. Chand, "Spectrum analysis of mesons using Nikiforov-Uvarov Functional Analysis method", Materials Research Proceedings, **22**, 7 (2022), https://doi.org/10.21741/9781644901878-2

[49] E.P. Inyang, E.P. Inyang, I.O. Akpan, J.E. Ntibi, and E.S. William, "Masses and thermodynamic properties of a Quarkonium system", Canadian Journal Physics, **99**, 982 (2021), https://doi.org/10.1139/cjp-2020-0578

[50] M. Abu-Shady, "N-dimensional Schrödinger equation at finite temperature using the Nikiforov-Uvarov method", Journal of Egyptian Mathematical Society, **25**, 86 (2017), https://doi.org/10.1016/j.joems.2016.06.006

[51] R. Olive, et al (Particle Data Group), Chinese Physics C, **38**, 090001 (2014), https://doi.org/10.1088/1674-1137/38/9/090001

[52] M. Tanabashi, C.D. Carone, T.G. Trippe, and C.G. Wohl, "Particle Data Group", Physical Review D, **98**, 546 (2018), https://doi.org/10.1103/PhysRevD.98.030001

[53] C.A. Onate, G.O. Egharevba, and D.T. Bankole, "Eigensolution to Morse potential for Scandium and Nitrogen monoiodides", Journal of Nigeria Society Physical Science, **3**, 282 (2021), https://doi.org/10.46481/jnsps.2021.407

[54] S.K. Nikiforov, and V.B. Uvarov, *Special Functions of Mathematical Physics* (Birkhauser, Basel, 1988).

[55] C. Tezcan, and R. Sever, "A general approach for the exact solution of the Schrodinger equation", International Journal of Theoretical Physics, **48**, 337 (2009), https://doi.org/10.1007/s10773-008-9806-y

[56] S.H. Dong, *Factorization Method in Quantum Mechanics, Fundamental Theories in Physics* (Springer, 2007)

APPENDIX A: NUFA METHOD

The NUFA method proposed by Ikot et al. [10] is a simple and elegant method for solving a second-order differential equation. The method is a combination of the NU [61], parametric NU [62], and Factorization [63] methods. The NU is well-known for solving a second-order differential equation of the form:

$$\psi''(y) + \frac{\tilde{\tau}(y)}{\sigma(y)}\psi'(y) + \frac{\tilde{\sigma}(y)}{\sigma^2(y)}\psi(y) = 0, \tag{A1}$$

where $\tilde{\sigma}(y)$ and $\sigma(y)$ are polynomials of the maximum second degree and $\tilde{\tau}(y)$ is a polynomial of the maximum first degree? Tezcan and Sever [70] later introduced the parametric form of the NU method in the form

$$\psi'' + \frac{\beta_1 - \beta_2 y}{y(1 - \beta_3 y)}\psi' + \frac{1}{y^2(1 - \beta_3 y)^2}\left[-\xi_1 y^2 + \xi_2 y - \xi_3 \right]\psi(y) = 0, \tag{A2}$$

where β_i and $\xi_i (i = 1, 2, 3)$ are all parameters. It can be observed in Eq. (A2) that the differential equation has two singularities at $y \to 0$ and $y \to 1$, thus we take the wave function in the form,

$$\psi(y) = y^\lambda (1 - \beta_3 y)^\nu f(y). \tag{A3}$$

Replacing Eq. (4) with Eq. (3) leads to the Eq. (A4),

$$
\begin{aligned}
& y(1-\beta_3 y)f''(y) + \left[\beta_1 + 2\lambda - (2\lambda\beta_3 + 2\nu\beta_3 + \beta_2)y \right]f'(y) \\
& -\beta_3\left(\lambda + \nu + \frac{\beta_2}{\beta_3} - 1 + \sqrt{\left(\frac{\beta_2}{\beta_3}-1\right)^2 + \frac{\xi_1}{\beta_3}} \right) \\
& \left(\lambda + \nu + \frac{\beta_2}{\beta_3^2} - 1 + \sqrt{\left(\frac{\beta_2}{\beta_3}-1\right)^2 + \frac{\xi_1}{\beta_3^2}} \right)f(y) \\
& + \left[\frac{\lambda(\lambda-1) + \beta_1\lambda - \xi_3}{y} + \frac{\beta_2\nu - \beta_1\beta_3\nu + \nu(\nu-1)\beta_3 - \frac{\xi_1}{\beta_3} + \xi_2 - \xi_3\beta_3}{(1-\beta_3 y)} \right]f(y) = 0.
\end{aligned} \tag{A4}
$$

Equation (A4) can be reduced to a Gauss hypergeometric equation if and only if the following functions are gone,

$$\lambda(\lambda - 1) + \beta_1\lambda - \xi_3 = 0, \tag{A5}$$

and

$$\beta_2 v - \beta_1 \beta_3 v + v(v-1)\beta_3 - \frac{\xi_1}{\beta_3} + \xi_2 - \xi_3 \beta_3 = 0. \tag{A6}$$

Thus Eq. (A4) becomes

$$y(1-\beta_1 y)f''(y) + \left[\beta_1 + 2\lambda - (2\lambda\beta_3 + 2v\beta_3 + \beta_2)y \right] f'(y)$$

$$-\beta_3 \left(\lambda + v + \frac{\beta_2}{\beta_3} - 1 + \sqrt{\left(\frac{\beta_2}{\beta_3} - 1\right)^2 + \frac{\xi_1}{\beta_3}} \right) \left(\lambda + v + \frac{\beta_2}{\beta_3^2} - 1 + \sqrt{\left(\frac{\beta_2}{\beta_3} - 1\right)^2 + \frac{\xi_1}{\beta_3^2}} \right) f(y) = 0. \tag{A7}$$

Solving Eqs. (A5) and (A6) completely give,

$$\lambda = \frac{(1-\beta_1)}{2} \pm \frac{1}{2}\sqrt{(1-\beta_1)^2 + 4\xi_3}, \tag{A8}$$

$$v = \frac{(\beta_3 + \beta_1\beta_3 - \beta_2) \pm \sqrt{(\beta_3 + \beta_1\beta_3 - \beta_2)^2 + 4\left(\frac{\xi_1}{\beta_3} + \beta_3\xi_3 - \xi_2\right)}}{2}. \tag{A9}$$

Equation (A7) is the hypergeometric equation type of the form,

$$y(1-y)f''(y) + \left[c - (a+b+1)y \right] f'(y) - abf(y) = 0. \tag{A10}$$

The energy equation and the related wave equation for the NUFA method are obtained using Eqs. (A3), (A7) and (A10), as follows:

$$\lambda^2 + 2\lambda\left(v + \frac{\beta_2}{\beta_3} - 1 + \frac{n}{\sqrt{\beta_3}}\right) + \left(v + \frac{\beta_2}{\beta_3} - 1 + \frac{n}{\sqrt{\beta_3}}\right)^2 - \left(\frac{\beta_2}{\beta_3} - 1\right)^2 - \frac{\xi_1}{\beta_3^2} = 0, \tag{A11}$$

$$\psi(y) = Ny^{\frac{(1-\beta_1) + \sqrt{(1-\beta_1)^2 + 4\xi_3}}{2}}$$

$$(1-\beta_3 y)^{\frac{(\beta_3 + \beta_1\beta_3 - \beta_2) + \sqrt{(\beta_3 + \beta_1\beta_3 - \beta_2)^2 + \left(\frac{\xi_1}{\beta_3^2} + \beta_3\xi_3 - \xi_2\right)}}{2}} {}_2F_1(a,b,c;y), \tag{A12}$$

where $a, b,$ and c are given as follows;

$$a = \sqrt{\beta_3}\left(\lambda + v + \frac{\beta_2}{\beta_3} - 1 + \sqrt{\left(\frac{\beta_2}{\beta_3} - 1\right)^2 + \frac{\xi_1}{\beta_3}} \right), \tag{A13}$$

$$b = \sqrt{\beta_3}\left(\lambda + v + \frac{\beta_2}{\beta_3} - 1 - \sqrt{\left(\frac{\beta_2}{\beta_3} - 1\right)^2 + \frac{\xi_1}{\beta_3}} \right), \tag{A14}$$

$$c = \beta_1 + 2\lambda. \tag{A15}$$

**КВАРК-АНТИКВАРКОВЕ ДОСЛІДЖЕННЯ З ОБЕРНЕНО-КВАДРАТИЧНИМ ПОТЕНЦІАЛОМ ЮКАВИ
З ВИКОРИСТАННЯМ МЕТОДУ ФУНКЦІОНАЛЬНОГО АНАЛІЗУ НІКИФОРОВА-УВАРОВА**

**Етідо П. Іньянг[a,b], Прінс К. Івуджі[b], Джозеф Е. Нтібі[b], Е. Омугбе[c],
Ефіонг А. Ібанга[a], Едді С. Вільям[b]**

[a]Фізичний факультет, Національний відкритий університет Нігерії, Джабі-Абуджа, Нігерія
[b]Група теоретичної фізики, факультет фізики, Університет Калабара, Р.М.В 1115 Калабар, Нігерія
[c]Фізичний факультет, Федеральний університет нафтових ресурсів, Еффурун, штат Дельта, Нігерія

Методом функціонального аналізу Нікіфорова-Уварова отримано вирішення рівняння Шредінгера з обернено-квадратичним потенціалом Юкави. Енергетичний спектр і хвильова функція отримано в замкнутому вигляді. Рівняння енергії було використано для передбачення мас важких мезонів, таких як чармоній ($c\bar{c}$) і ботомоній ($b\bar{b}$) для різних квантових чисел. Отримані результати узгоджувалися з іншими теоретичними прогнозами та експериментальними даними з відсотковою похибкою 1,68 % та 0,50 % для чармонію ($c\bar{c}$) та ботомонію ($b\bar{b}$) відповідно.

Ключові слова: рівняння Шредінгера; метод функціонального аналізу Нікіфорова-Уварова; обернено квадратичний потенціал Юкави; важкі мезони

A NUMERICAL SIMULATION FOR EFFICIENCY ENHANCEMENT OF CZTS BASED THIN FILM SOLAR CELL USING SCAPS-1D†

Muhammad Aamir Shafi[a,e,f,*], **Sumayya Bibi**[b], **Muhammad Muneeb Khan**[c],
Haroon Sikandar[d], **Faisal Javed**[c], **Hanif Ullah**[e], **Laiq Khan**[a], **Bernabe Mari**[f]

[a]Department of Electrical and Computer Engineering, COMSATS University Islamabad, Pakistan
[b]Department of Electrical Engineering, Bahauddin Zakariya University Multan, Pakistan
[c]Department of Electrical Engineering, Pakistan Institute of Southern Punjab Mulatn, Pakistan
[d]CEME, College of Electrical and Mechanical engineering, Nust Islamabad, Pakistan
[e]Department of Electrical Engineering, Federal Urdu University of Arts Science and Technology, Islamabad, Pakistan
[f]Instituto de diseño y Fabricación (IDF), Universitat Politécnica de València (UPV), Spain
*Corresponding Author: aamirshafi@ymail.com

In this paper we proposed a solar cell having model "*Back Contact/CZTS/ZnCdS/ZnO/Front Contact*". CZTS is working as an absorber layer, ZnCdS as a buffer layer and ZnO as a window layer with back and front contacts. The Zn content was varied from 0% to 10% and bad gap was changed from 2.42 to 2.90 eV as described in the literature. The impact of this band gap variation has been observed on the performance of solar cell by using SCAPS-1D software. The efficiency was varied due to variation in bandgap of ZnCdS thin film layer. The simulation was carried out at 300 K under A.M. 1.5 G 1 Sun illumination. The energy bandgap diagram has been taken from SCAPS to explain the different parameters of solar cell. The effect of ZnCdS having different bandgap values was observed. Then the thickness of CZTS layer was varied to check its effect and hence at 3.0 μm gave the imporved efficiency of 13.83% roundabout. After optimization of CZTS layer thickness, the effect of working temperature was examined on the performance of solar cell. The absorption coefficient variation from $1 \cdot 10^4$ to $1 \cdot 10^9$ cm^{-1} caused major effects on the characteristics parameters of solar cell along with on J-V characteristics and Quantum Efficiency curve. At $1 \cdot 10^9$ cm^{-1} absorption coefficient the efficiency of solar cell boost up to 16.24%. This is the remarkable improvement in the efficiency of solar cell from 13.82% to 16.24%. After optimization of all parameters, simulation was run at 280 K, having CZTS thickness of 3.5 μm, with 10% content Zn in ZnCdS (2.90 eV), and absoption coefficient of $1 \cdot 10^9$, the model efficiency reached up to 17.6% with Voc of 0.994 V, Jsc 26.1 mA/cm^2 and Fill factor was 71.4%.
Keywords: ZnCdS; CZTS; Simulation; Efficiency; SCAPS-1D
PACS: 02.60.Cb, 02.60.Pn, 82.47.Jk, 84.60.Jt, 42.79.Ek, 89.30.Cc

INTRODUCTION

Group II-VI semiconducting material of "Cadmium" focussed chalcogenide family have more modulation by academic researchers because of its excellent properties and potential contributions to the field of electrical, optoelectronic devices, light emitting, etc. Cadmium sulphide (CdS) is a chemical that belongs to the group II-VI.   Cadmium telluride (CdTe), copper indium diselenide/sulphide (CIDS), and copper indium gallium diselenide/Sulphide (CIGS) solar cells are semiconductor materials that have uses in a variety of heterojunction photovoltaic systems [1]. CdS thin films exhibit significant attenuation due to their optoelectronic characteristics [2]. A study of the processing of certain III-V and II-VI binary compound semiconductors for technological applications was conducted [3,4,5]. Te optical band-gap of CdS nanoparticles produced using the mw aided technique was investigated larger than that of bulk CdS nanoparticles [6,7]. The small bandgap reduces the power conversion efficiency by partially blocking transmission of high-energy photons to an absorber layer below. The larger bandgap of ZnxCd1-xS results in greater quantum efficiency in the blue part of the spectrum when CdS is substituted. The addition of Zn to the CdS buffer layer material lowers the lattice constant, resulting in a more advantageous conduction band alignment with a lattice match to the CIGS absorber. It has been discovered that adding Zn to CIGS solar cells improves both Voc and Jsc of solar cell, resulting in a better conversion efficiency [8,9]. ZnCdS may also be used to make p-n junctions with no lattice mismatch in quaternary materials like $CuIn_xGa_{1-x}Se_2$ or $CuIn_xGa_{1-x}Se_2(S_xSe_{1-x})_2$. By adjusting the Zn content, the growth characteristics of ZnCdS films may be fine-tuned. Different Zn concentrations control the pace of CdS development and are a key element in influencing the film's characteristics [10]. Ternary zinc cadmium sulfide (ZnCdS) has long been recognized as a suitable material for thin-film photovoltaic applications due to its high optical absorption coefficient [11]. Thin film Electrodeposition, chemical co-precipitation, spray pyrolysis, chemical vapor deposition, chemical bath deposition, and dip coating have all been used to make ZnCdS. Chemical bath deposition is one of the most used methods because of its convenience, simplicity, uniformity, stability, adhesion, homogeneity, and compactness with no pin holes thin films [12]. To improve the collection of short wavelength photons, minimize electron-hole recombination, as well as promote charge transfer to photoelectrode, ZnCdS was used as a window layer, and high efficiency has been achieved in thin copper indium gallium selenide (CIGSe$_2$) and copper indium gallium sulfide (CIGS$_2$) absorber layers [13,14]. A catalyst with a direct bandgap of 2.4 eV

for CdS and 3.7 eV for ZnS is thought to be effective [15]. ZnCdS has reasonable and adjustable absorbance based on the Zn/Cd ratio in the visible solar spectrum and good electrical conductivity [16,17]. As a result, ZnCdS is widely regarded as a competent bandgap material for photocatalytic degradation [18]. When Zn is doped with CdS to produce ZnCdS, the CdS bandgap increases to 3.7 eV due to the doped ZnS semiconductor bandgap. Because of this property, ZnCdS has been identified as an alternate buffer and window layer for solar cells, replacing CdS [19]. When Zn was doped with CdS, the material's resistance was found to be greater than that of CdS. In addition, Zn aids in the reduction of absorption losses at the window layer in CdS. The open circuit voltage and short circuit current in the hetero-junction structure grow as a result of this [20,21]. Because ZnCdS has a higher spectrum response than CdS due to the Zn component.The performance of ZnCdS-based solar devices will be greatly anticipated as a result of this characteristic, and ZnCdS will be employed as a suitable material for manufacturing p-n junctions. By raising the Zn content in the bath, the crystal size of ZnCdS was decreased. Furthermore, the absorption wavelength of CdS-based materials has been shown to change to lower wavelengths owing to Zn doping [22]. The effect of Zn on the CdS brings the changes in bandgap of ZnCdS according to the concentration of Zn, hence at each concentration the performance of Solar Cell is analyzed using SCAPS-1D Simulator.

SOLAR CELL MODEL AND NUMERICAL PARAMETERS

The solar model that has been used for the simulation in this research paper is shown in Figure. 1.
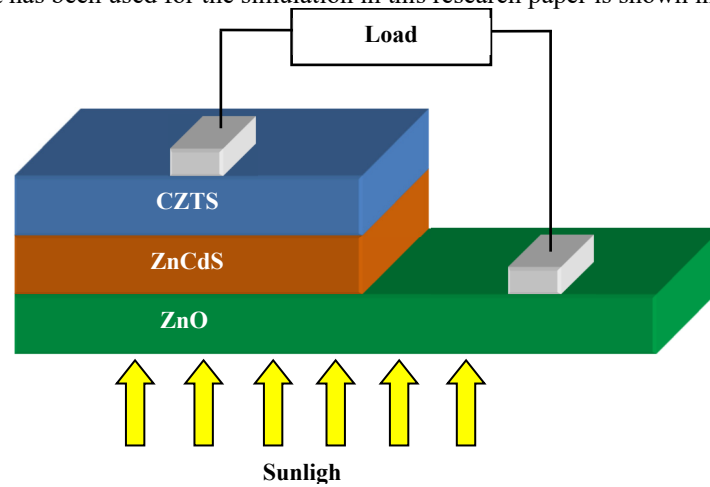

Figure 1. Solar cell model in Simulation.

To analyze the performance of the solar cell a one-dimensional software SCAPS-1D is used. The solar model that has been examined is consisting of CZTS absorber layer, ZnCdS is used as a buffer layer and ZnO is being used as window layer. Solar cell characteristics utilized in our simulation were chosen from academic literature, theories, and experiment-based results as shown in Table 1 [23]. The lighting spectrum is adjusted to AM1.5 G 1 sun, whereas working temperature is set to 300 K [24,25]. Quaternary semiconductors are difficult to manufacture and need a variety of time-consuming and costly technical processes. However, utilizing experimental techniques to confirm theoretical assumptions that are necessary in research is unavoidable [26]. Computer based simulation software allows time and money to be saved. It's a strong approach for predicting and assessing the influence of numerous model parameters and material characteristics on output performance of a solar cell. In this study, we use SCAPS software developed by Marc Bargeman and colleagues at the University of Gent [27,28].

When modelling solar cells, ensure that the program can solve the Poisson's equations for the charge electrostatic potential $div\,(\varepsilon\nabla\Psi) = -\rho$ [29], as well as the carrier continuity equations for electrons and holes equations 1 and 2 [30].

$$\frac{\partial n}{\partial t} = \frac{1}{q} div \overrightarrow{J_n} + G_n - R_n, \tag{1}$$

$$\frac{\partial p}{\partial t} = -\frac{1}{q} div \overrightarrow{J_p} + G_p - R_p, \tag{2}$$

where,
$n = concentration\ of\ electrons, p = concentration\ of\ holes,\ J_n = Electron\ current\ density,$
$J_p = Hole\ current\ density,\ G_n = Electron\ Generation\ Rate,\ G_p = Hole\ Generation\ Rate,$
$R_n = Electron\ Recombination\ Rate,\ R_p = Hole\ Recombination\ Rate$

The influence of Zn content on ZnCdS layer plays an important role in varying its bandgap and hence this varied bandgap has been examined with CZTS based solar cell. After that the effect of CZTS thickness and absorption coefficient variation has been examined as well as effect of different teperatutres on the performance of solar cell was next simulated.

The solar cell parameters used in simulation are listed below in Table 1. Whereas, parameters for both front and back contacts are shown in the Table 2.

Table 1. Numerical Parameters used for simulation [31,32].

Parameters	CZTS	ZnCdS	ZnO
$W\ (\mu m)$	2.00	0.10	0.05
$E_g(eV)$	1.55	2.42	3.35
$\chi\ (eV)$	4.500	4.440	4.210
ε_r	10.000	9.300	9.000
$N_C(cm^{-3})$	2.200E+18	2.100E+18	2.200E+18
$N_V(cm^{-3})$	1.800E+19	1.700E+19	1.800E+19
$V_e\ (cm/s)$	1.000E+7	1.000E+7	1.000E+7
$V_P\ (cm/s)$	1.000E+7	1.000E+7	1.000E+7
$\mu_e(cm^2/(Vs))$	1.000E+2	9.500E+1	2.500E+1
$\mu_p(cm^2/(Vs))$	2.000E+1	3.500E+1	1.000E+2
$N_D(cm^{-3})$	0.000E+0	2.500E+16	1.000E+18
$N_A(cm^{-3})$	8.220E+18	0.000E+0	0.000E+0
α	Scaps Value	Scaps Value	Scaps Value

Table 2. Simulation Parameters used for back and front contact from SCAP-1D.

Parameters	Front Contact	Back Contact
Surface recombination velocity of electrons (cm/s)	1.00×10^7	1.00×10^5
Surface recombination velocity of holes (cm/s)	1.00×10^5	1.00×10^7
Metal work function (eV)	4.6039	5.8973
Majority carrier barrier height relative to Ef (eV)	0.0539	0.1527
Majority carrier barrier height relative to Ev (eV	0.0000	0.0000

Study as a function of Zn content in ZnCdS buffer layer

Both CdS and ZnCdS are semiconductors with a direct bandgap. Optical bandgap of semiconductors may then be calculated through graphing a square of the photon energy $(\alpha h\nu)^2$ vs photon energy $(h\nu)$. A value of optical bandgap is determined through extrapolating a linear component of this curve to an energy axis. Figure 2 illustrates a curve of $(\alpha h\nu)^2$ as a function of photon energy for varied Zn concentrations in ZnCdS thin films. The results demonstrate that when the Zn concentration increases, the bandgap moves to higher energies. Table 3 show the results for optical bandgaps ranging from 2.42 eV for CdS to 2.90 eV for various ZnCdS thin films. Figure 2 and Table 3 are taken from the article [33].
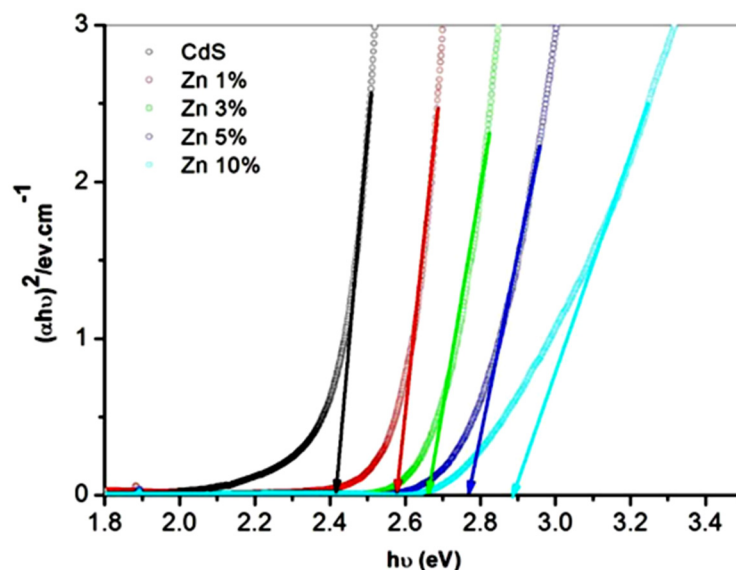

Figure 2. Plot of $(\alpha h\nu)^2$ vs photon energy $(h\nu)$ for ZnCdS thin films with different Zn concentrations

Table 3. Optical bandgap for ZnCdS thin films with different Zn amounts

Sr#	Zn Content	ZnCdS band gap
	%	eV
1	0	2.42
2	1	2.58
3	3	2.67
4	5	2.78
5	10	2.90

To observe this varying bandgap effect on performance of CZTS based solar cell of proposed model *"Glass/Back Contact/CZTS/ZnCdS/ZnO/Front Contact"* has been simulated where the thickness of CZTS and ZnO was kept 2 μm and 0.05 μm respectively. The working temperature has been kept constant 300K. Series resistance is taken as to zero ohm where as the shunt resistance as infinite.

Study as a function of CZTS absorber layer thickness

To observe an effect of thickness of CZTS absorber layer in solar device model *"Glass/Back Contact/CZTS/ZnCdS/ZnO/Front Contact"*on performance of solar cell, thickness of ZnO layer was kept 0.05 μm and ZnCdS layer with thickness of 0.01 μm was used. The working temperature is maintained 300 K [34]. Series resistance is taken as to be zero ohm where as the shunt resistance as an infinite. The effect of CZTS thickness varying from 1.0 μm to 3.0 μm was simulated.

Study as a function of working temperature

To observe an effect of different working temperautes of solar cell model *"Glass/Back Contact/CZTS/ZnCdS/ZnO/Front Contact"*on a performance of solar cell, thickness of ZnO layer was kept 0.05 μm and ZnCdS layer with thickness of 0.01 μm was used. Whereas the thickness of CZTS absorber layer fixed was 2.0 μm. The series resistance is taken as to be zero ohm whereas the shunt resistance as an infinite. The effect of working temperature varying from 280 K to 350 K was simulated.

Study as a function of absorption coefficient

To observe an effect of absorption coeffieicient of absorber layer in solar cell model *"Glass/Back Contact/CZTS/ZnCdS/ZnO/Front Contact"* on performance of solar cell, thickness of ZnO layer was kept 0.05 μm and ZnCdS layer with thickness of 0.01 μm was used. Whereas the thickness of CZTS absorber layer fixed was 2.0 μm. The series resistance is taken as to be zero ohm whereas the shunt resistance as an infinite. The working temperature is kept 300 K. The effect of absorption coefficient varying from $1 \cdot 10^4$ cm^{-1} to $1 \cdot 10^8$ cm^{-1} was simulated.

RESULTS AND DISCUSSIONS
Energy Band Diagram

Energy band diagram of proposed solar model *"Glass/Back Contact/CZTS/ZnCdS/ZnO/Front Contact"* is shown below and this is taken from the SCAPS-1D simulation software. The importance of this energy band diagram is to help out the discussion of optical properties of solar cell [35]. The band gap is adjusted by ZnCdS buffer layer in between CZTS absorber and ZnO window layers.
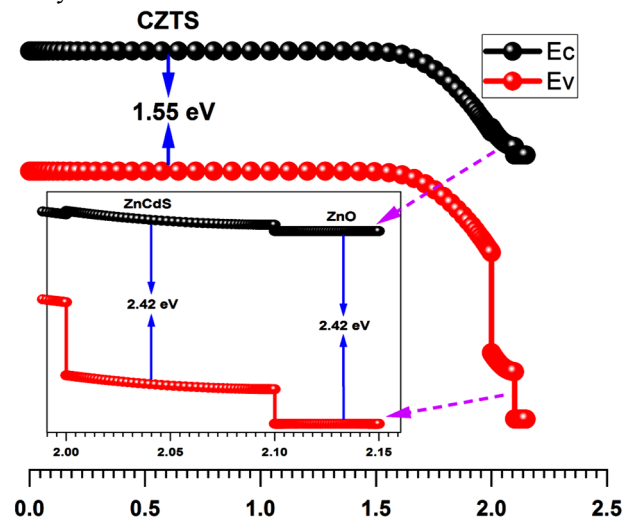
Figure 3. Energy band diagram

The visible light is absorbed throughout the absorber as well as at the heterojunction. The bandgap value for incident light photons that is ideal for most of the light to be absorbed for efficient power conversion efficiency is more or equal to 1.55 eV [36].

Effect of Zn Content

Under AM1.5 G 1 sun simulation was executed and at first we used ZnCdS buffer layer with 0% of Zn content and as a result Voc was 0.883483 V, Jsc was 22.55786 mA/cm^2, FF was 69.3755% and eta was 13.8262%. As the 1% of Zn content was dopped with CdS, its bandgap enhanced upto 2.58 eV, and at this bandgap Voc was 0.883434 V, Jsc was 22.54279 mA/cm^2, FF was 69.4027% and eta was recorded 13.8216%. All the parameters were decreased up to some extend because initially the Zn content was less in percentage and hence recombination of charges increased causing the decrement in the characteristics parameters of solar cell as shown in Table 4.

Table 4. Effect of Zn content on the characteristic's parameters of solar cell

Zn Content	ZnCdS band gap	Voc	Jsc	FF	Eta
%	eV	V	mA/cm^2	%	%
0	2.42	0.883483	22.55786	69.3755	13.8262
1	2.58	0.883434	22.54279	69.4027	13.8216
3	2.67	0.883421	22.5389	69.4176	13.822
5	2.78	0.883414	22.53656	69.4349	13.8239
10	2.90	0.883414	22.53607	69.4507	13.8267

But as the percentage of Zn content was gone on increasing the all characteristics parameters were also gone on increasing accordingly. The effect is also shown in the following Figure 4. Finally, when Zn content of 10% doped, the Voc improved to 0.883414 V, Jsc increased up to 22.53607 mA/cm^2, FF reached 69.4507% and hence the efficiency achieved 13.8267%. This value of efficiency is more than the efficiency at pure CdS. Finally, it is proved that as the Zn content increased the efficiency was also increased to some extent.
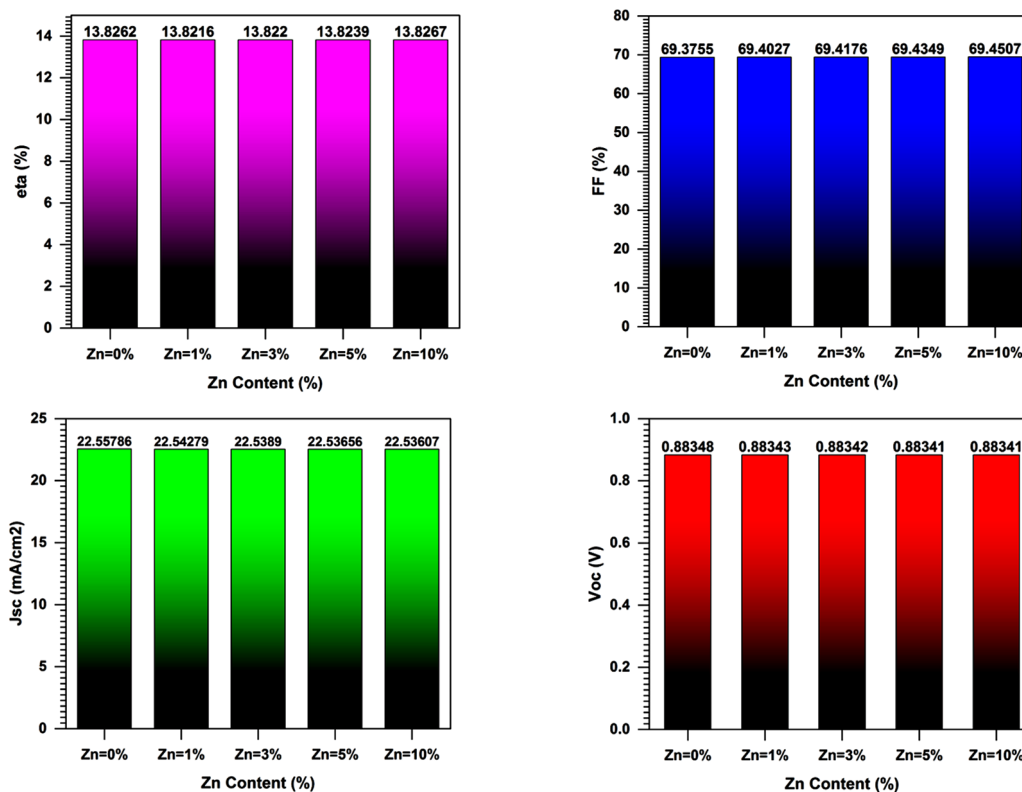

Figure 4. Effect of Zn content on Characteristics parameters of solar cell

The pattern of Zn content on the performance of solar cell is also shown on the J-V characteristic curve of solar device in following Figure 5. Effect of Zn content on J-V curve is same as in efficiency of cell as discussed above. Initially when there is 0% content of Zn and bandgap is 2.42 eV, its curve shows gud performance than 1%, 3% and 5% content of Zn with ZnCdS having 2.58 eV, 2.67 eV and 2.78 eV of bandgap respectively.
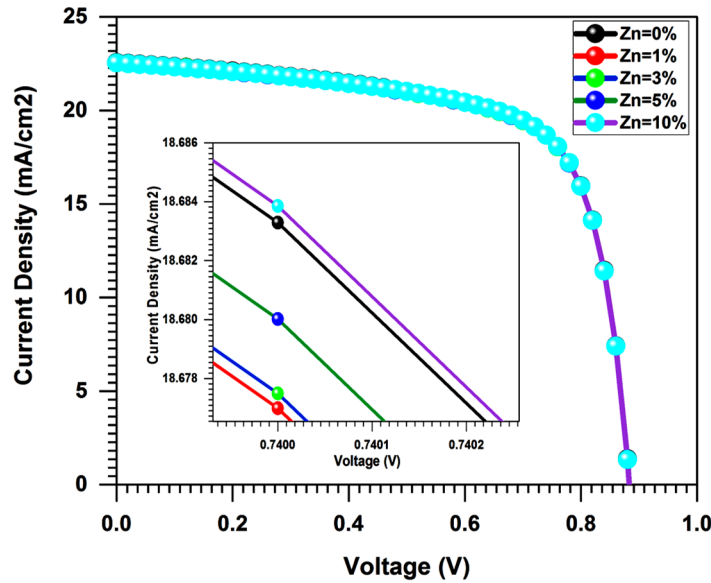
Figure 5. Effect of Zn content on J-V curve of the proposed solar cell

But at 10% content of Zn giving the 2.90 eV gave the most improved curve with skyblue bubles as shown in Figure 5.

Effect of CZTS Thickness

Because the optimum Zn concentration value of 10% produced satisfactory results, ZnCdS with a bandgap of 2.90 was simulated using a buffer layer of 0.1 μm thickness.

Table 5. CZTS Thickness effect on Characteristics Parameters

CZTS Thickness	Voc	Jsc	FF	eta
um	V	mA/cm^2	%	%
1.5	0.88339	22.52569	69.457	13.82123
2.0	0.88342	22.53815	69.45105	13.82813
2.5	0.88341	22.5484	69.4465	13.83345
3.0	0.88345	22.5571	69.44461	13.83897
3.5	0.88344	22.56487	69.4324	13.84117

As a window layer, ZnO with a thickness of 0.05 μm was used. Working temperature was held at 300K under A.M 1.5 G 1 solar irradiation, and simulation was performed by changing thickness of the CZTS absorber layer from 1.5 to 3.5 μm.
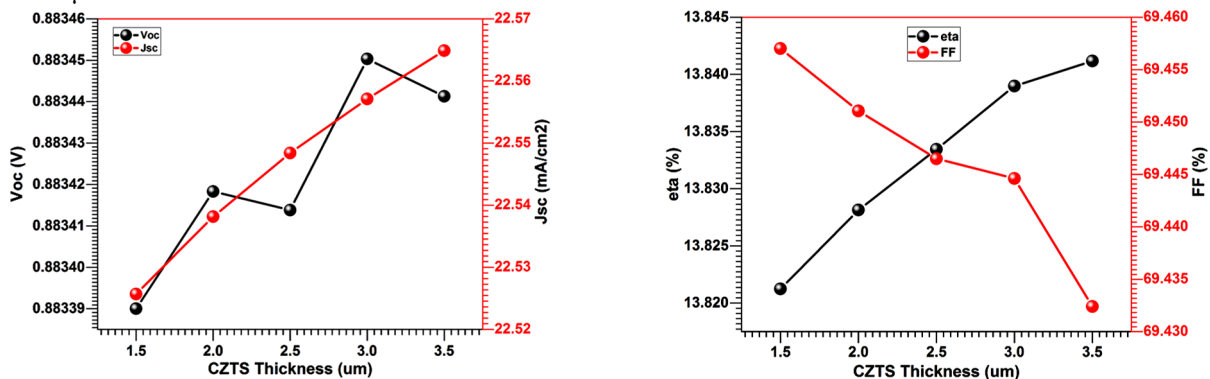

Figure 6. Effect of CZTS layer thickness on Characteristics parameters curves

Voc was 0.88339 V at 1.5 μm, Jsc was 22.525 mA/cm^2, FF was 69.457 %, and eta was 13.821 %. The open circuit voltages climbed to 0.88342 V as the thickness grew from 1.5 to 2.0 μm, and the current density increased to 22.538 mA/cm^2, while the factor fell to 69.451 %, yet efficiency improved to 13.828 %. The thickness of CZTS was then adjusted to 2.5 μm, and the Voc, Jsc, FF, and eta were reported as 0.88341 V, 22.548 mA/cm^2, 69.446 %, and 13.833%, respectively, at this thickness. Finally, when the thickness was raised from 3.0 to 3.5 μm, Voc went from 0.88345 to 0.88344 V, and Jsc went from 22.5571 to 22.5648 mA/cm^2. Similarly, FF varied from 69.4446 to 69.4324 %, while eta varied from 13.8389 to 13.8411 % as shown in Table 5 and Figure 6.

Temperature Effect

From the above results and discussion, we conclude the optimized Zn content of 10% with bandgap 2.90 eV of ZnCdS along with the CZTS optimum layer thickness of 3.5 μm, the simulation was run again to check an effect of working temperature on performance of solar device.

The temperature was varied from 280 to 350 K. At 280 K temperature, Voc was 0.9535 V, Jsc 22.6074 mA/cm^2, FF 70.208% and efficiency raised to 14.846%. As the temperature is very low hence the heating effect on the solar cell is negligible that's why its efficiency raised to 14.846%. This is very fruitful improvement because of temperature.

But as temperature rises from 280 to 350 K, all the parameters are affected largely as shown in Table 6 and Figure 7.

Table 6. Temperature effect on Characteristics Parameters

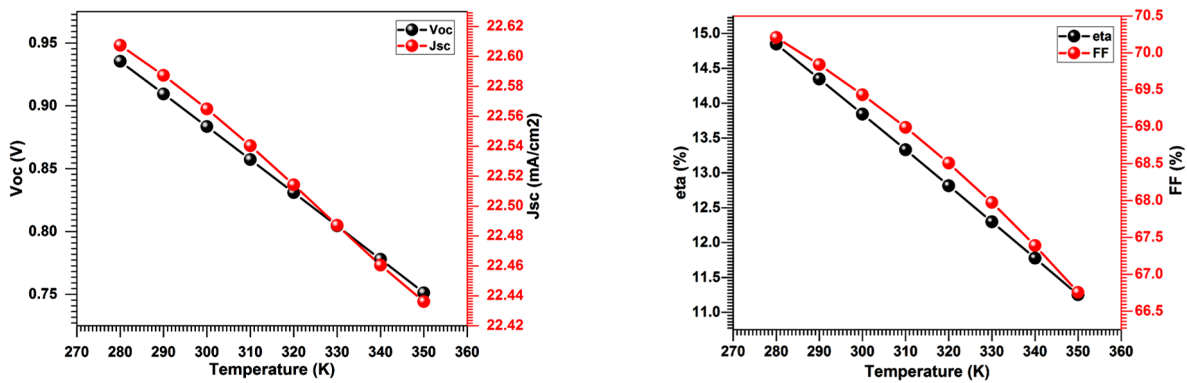| Temperature	Voc	Jsc	FF	eta
K	**V**	**mA/cm^2**	**%**	**%**
280	0.93535	22.60743	70.20864	14.84627
290	0.9094	22.58729	69.84021	14.34577
300	0.88344	22.56487	69.43240	13.84117
310	0.85725	22.54034	68.99134	13.33098
320	0.83086	22.51415	68.50709	12.81500
330	0.80449	22.48712	67.97279	12.29675
340	0.77797	22.46051	67.39014	11.77553
350	0.75123	22.43615	66.75632	11.25160

Figure 7. Temperature effect on Characteristics parameter curves

At 290 K of temperature the Voc decreased to 0.9094 V, Jsc also decreased to 22.5872 mA/cm^2, FF 69.84% and efficiency decreased up to 14.34% from 14.846%. Because as the temperature rises, the collision of electrons and holes increases and due to their collision, the flow of these charges slow down hence causing the less generation of potential as a result efficiency decreases. The negative effect of increasing temperature is also shown in J-V curve as shown in the Figure 8.
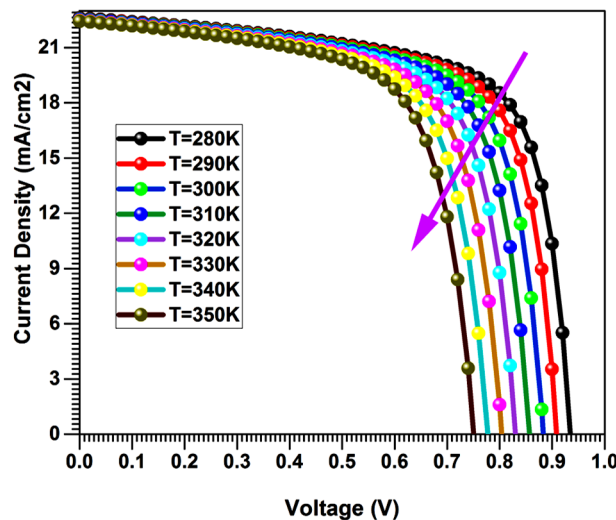

Figure 8. Temperature effect on J-V curve

A negative effect of rising temperature is not only on the characteristic's parameters (Voc, Jsc, FF and eta) and not on J-V curve, but it imparts its effect on the quantum efficiency. As quantum efficiency is a ratio of carriers collected by the solar cell to number of photons of sunlight incident on the solar cell. So as by increasing the temperature, its curve is moving down, that means the ratio is decreasing which ensures that number of carriers collecting on solar device surface are decreasing because of increasing temperature as shown in Figure 9.
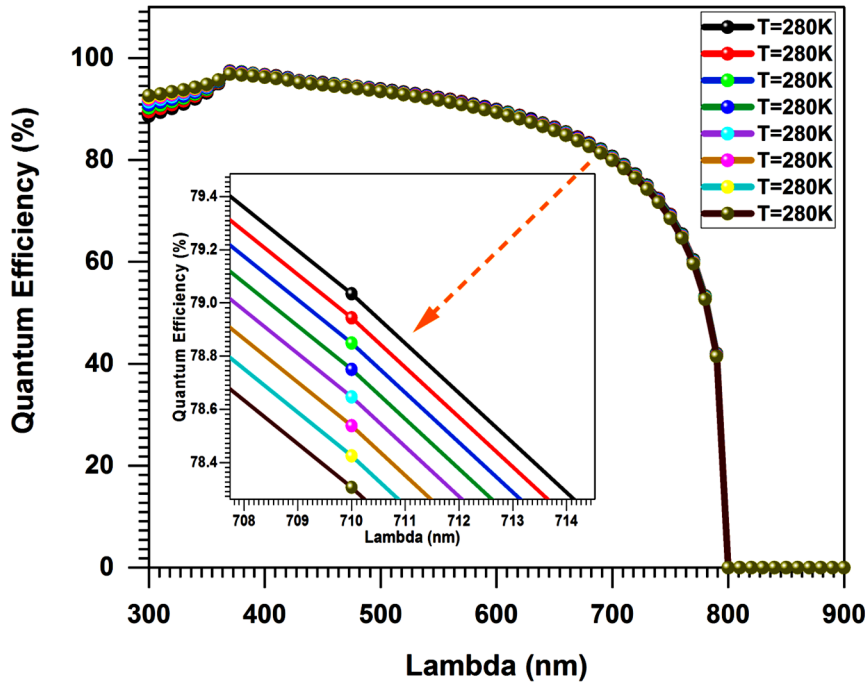

Figure 9. Temperature effect on Quantum Efficiency of Solar Cell

Finally at 350K, Voc changed from 0.93535 to 0.75123 V, Jsc decreased from 22.60743 to 22.43615 mA/cm^2, FF from 70.20864 to 66.75632% and eta effect the most from 14.84627 to 11.2516%.

Effect of Absorption Coefficient

Proposed solar cell *"Back Contact/Glass/CZTS/ZnCdS/ZnO/Front Contact"* was simulated at 300 K temperature under AM 1.5 G 1 SUN. The optimized thickness of CZTS of 3.5 μm, Zn contented ZnCdS having optimized bandgap of 2.90 with 0.1 μm thickness and ZnO with fixed thickness of 0.05 μm were used in the simulation program.

The penetration of sun light in the solar cell has the major role on its efficiency. Because as much light will penetrate in the solar cell material, the more light will be able to absorbed. So, absorption coefficient tells about this absorption. As the absorption coefficient increases, the number of photons going to be absorbed is also increased. Hence to check an effect of absorption coefficient on a performance of solar device, its value was varied from $1 \cdot 10^4$ to $1 \cdot 10^9$ cm^{-1}.

At $1 \cdot 10^4$ cm^{-1} of absorption coefficient, the Voc was 0.8158 V, Jsc 6.447 mA/cm^2, FF was 60.635% and eta was only 3.189%. But as the absorption coefficient was increased the characteristics parameters were also increased as shown in Table 7. At $1 \cdot 10^5$ cm^{-1} absorption coefficient, Voc was increase upto 0.882 V. But in Jsc there was very surprisingly increment was observed from 6.44 to 22.10 mA/cm^2 with FF 68.89%. There was a remarkable effect of absorption coefficient on the efficiency of solar cell because it was improved from 3.18% to 13.43%. This effect can be observed in the Figure 10 of characteristics parameters of solar cells also.The absorption coefficient was varied upto $1 \cdot 10^9$ cm^{-1} and at this value the Voc was recorded 0.8917 V, Jsc of 25.92%, FF upto 70.278% and efficiency boost up to 16.24%.

Table 7. Absorption Coefficient Effect on Characteristics Parameters

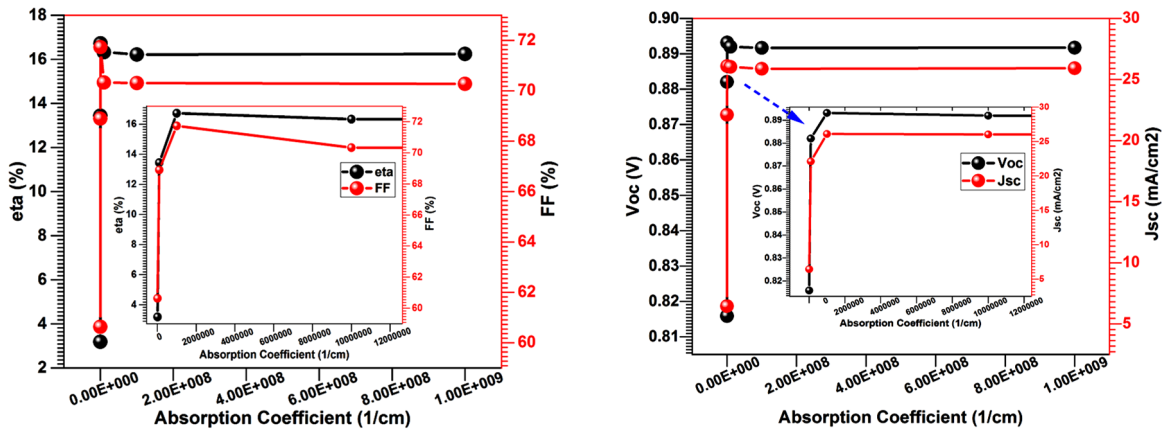| Absorption Coefficient	Voc	Jsc	FF	Eta
cm^{-1}	V	mA/cm^2	%	%
1.00×10^4	0.81587	6.447810	60.63543	3.189760
1.00×10^5	0.88202	22.10740	68.89824	13.43457
1.00×10^6	0.89316	26.09574	71.73494	16.71967
1.00×10^7	0.89199	26.02355	70.33203	16.32608
1.00×10^8	0.89168	25.87128	70.30721	16.21917
1.00×10^9	0.89170	25.92108	70.27816	16.24390

Figure 10. Effect of Absorption coefficient on characteristic parameters curves

Figure 11 represents the effect of absorption coefficient on J-V characteristic curve of solar cell. From the curve it is investigated that by increasing an absorption coefficient, the curve goes up going away from the origin showing the improvement in the performance of solar cell.
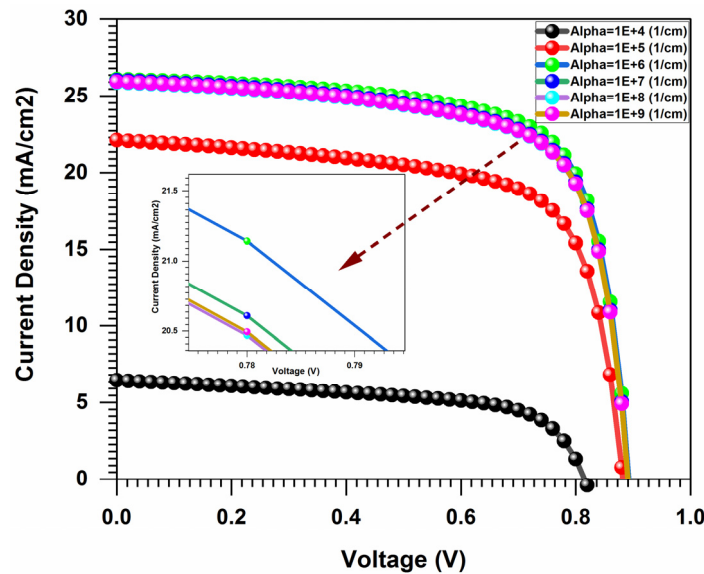

Figure 11. Effect of Absorption coefficient on characteristic parameters curves
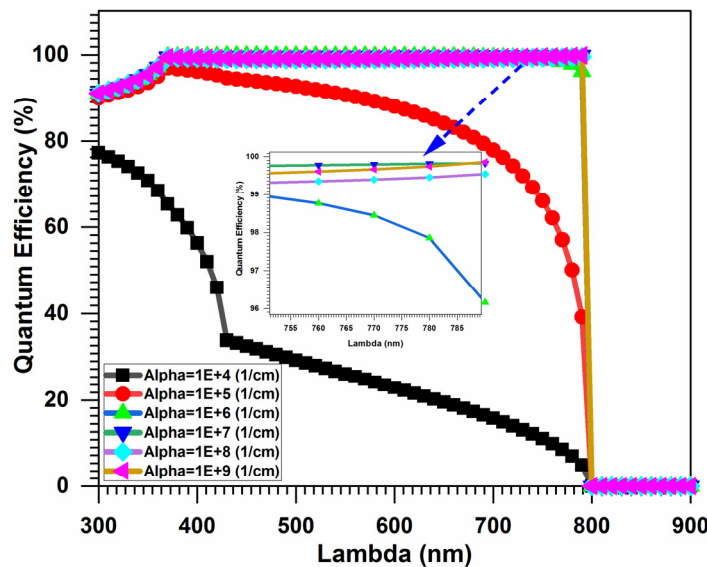

Figure 12. Effect of Absorption coefficient on Quantum Efficiency of solar cell.

Quantum efficiency graph in Figure 12 shows the effect of absorption coefficient. As the absorption coefficient increases, the graph improves to upward matching to 100% quantum efficiency showing an enhancement in the performance of solar cell.

CONCLUSION

Proposed solar cell model "*Back Contact/CZTS/ZnCdS/ZnO/Front Contact*" was simulated to investigate an effect of ZnCdS buffer layer varied badgap on the performance of solar cell. By increasing the bandgap of ZnCdS the performance of solar is improved hence the role of Zn content in ZnCdS has definite impact because all characteristics parameters were changed at different content of Zn. At 10% Zn content ZnCdS has 2.90 eV, and this was the optimized value at which we got maximum efficiency of 13.826% along with 69.45% fill factor. Later on the effect of CZTS absorber layer was observed on characteristics parameters and J-V curve of the solar cell. Thickness of CZTS was varied from 1.5 μm to 3.5 μm. The optimized thickness was 3.5 μm because at this thickness efficiency was 13.841% which was initially 13.826%. After optimization of Zn content and CZTS absorber layer, the effect of working temperature was observed by varying it from 280 K to 350 K. By increasing temperature the efficiency decreased from 14.84% to 11.25% for 280K to 350K. But it is note able that as the temperature was decreased from 300K (normal temperature) to 280K, the efficiency was increased from 13.82% to 14.84%. At the end the effect of absorption coefficient was studied by varying it from $1\cdot10^4$ to $1\cdot10^9$. At $1\cdot10^9$, the efficiency boost up to 16.24%. After optimization of all parameters, simulation was run at 280K, having CZTS thickness of 3.5 μm, with 10% content Zn in ZnCdS (2.90 eV), and absoption coefficient of $1\cdot10^9$, the model efficiency reached up to 17.6% with Voc of 0.994 V, Jsc 26.1 mA/cm^2 and Fill factor was 71.4%. These results are very remarkable and will be very useful for the researcher's consideration during synthesis of this "*Back Contact/CZTS/ZnCdS/ZnO/Front Contact*" purposed model type solar cell and the simulation results may be utilized experimentally to build "CZTS/ ZnCdS /ZnO" based solar cells in future with optimization of this work.

Conflict of Interest. Authors declared that there is no conflict of interest.

ORCID IDs
Muhammad Aamir Shafi, https://orcid.org/0000-0001-9813-7029; **Hanif Ullah,** https://orcid.org/0000-0002-0529-973X
Laiq Khan, https://orcid.org/0000-0003-3659-3824; **Bernabe Mari,** https://orcid.org/0000-0003-0001-419X

REFERENCES
[1] Repins, S. Glynn, J. Duenow, T.J. Coutts, W.K. Metzger, and M.A. Contreras, in: *Proc. SPIE 7409, Thin Film Solar Technology*, 74090M (United States, 2009), https://doi.org/10.1117/12.828365

[2] H. Khallaf, I.O. Oladeji, G. Chai, and L. Chow, "Characterization of CdS thin films grown by chemical bath deposition using four different cadmium sources", Thin Solid Films. **516**(21), 7306 (2008), https://doi.org/10.1016/j.tsf.2008.01.004

[3] L.S.S. Singh, K.P. Tiwary, R.K. Purohit, Z.H. Zaidi, and M. Husain, "ECR plasma etching of GaAs in CCl2F2/Ar/O2 discharge and IR studies of the etched surface", Current Applied Physics, **5**(4), 351 (2005), https://doi.org/10.1016/j.cap.2004.04.002

[4] S.K. Choubey, A. Kaushik, and K.P. Tiwary, "Structural and optical properties of pure and Mg doped CdSe nanoparticles synthesised by microwave assisted method", Chalcogenide Letters, **15**(3), 125 (2018), https://chalcogen.ro/125_ChoubeyS.pdf

[5] R. Kumar, R. Praveen, S, Rani, K. Sharma, K.P. Tiwary, and K.D. Kumar, "ZnSe Nanoparticles Reinforced Biopolymeric Soy Protein Isolate Film", Journal of Renewable Materials, **7**(8), 749 (2019), https://www.techscience.com/jrm/v7n8/30575

[6] S.K. Choubey, and K.P. Tiwary, Digest Journal of nanomaterials and Biostructures, **11**(1), 33 (2016), https://chalcogen.ro/33_Choubey.pdf

[7] S.K. Choubey, and K.P. Tiwary, International Journal of Innovative Research in Science, Engineering and Technology, **3**(3), 10670 (2014), https://techjournals.stmjournals.in/index.php/NTs/article/download/829/747

[8] B.S. Tosun, C. Pettit, S.A. Campbell, and E.S. Aydil "Structure and Composition of ZnxCd1–xS Films Synthesized through Chemical Bath Deposition", ACS Appl. Mater. Interfaces. **4**(7), 3676 (2012), https://doi.org/10.1021/am300771k

[9] J. Song, S.S. Li, S. Yoon, J. Song., S.S. Li, S. Yoon, W.K. Kim, J. Kim, J. Chen, V. Craciun, T.J. Anderson, O. D. Crisalle, and F. Ren, "Growth and characterization of CdZnS thin film buffer layers by chemical bath deposition", in: *Conference Record of the IEEE Photovoltaic Specialists Conference*, (IEEE, 2005), pp. 449-452.

[10] S. Kumar, and K.P. Tiwary, "ZnCdS thin film chalcogenide by chemical bath deposition method", Nanotrends AJ Nanotechnol Appl, **22**(1), 19 (2020), https://techjournals.stmjournals.in/index.php/NTs/article/download/829/747

[11] T.P. Kumar, S. Saravanakumar, and K. Sankaranarayanan, "Effect of annealing on the surface and band gap alignment of CdZnS thin films", Applied Surface Science, **257**(6), 1923-1927 (2011), http://dx.doi.org/10.1016%2Fj.apsusc.2010.09.027

[12] C. Xing, Y. Zhang, W. Yan, and L. Guo, "Band structure-controlled solid solution of Cd1-x ZnxS photocatalyst for hydrogen production by water splitting", International Journal of Hydrogen Energy, **31**(14), 2018 (2006), https://doi.org/10.1016/j.ijhydene.2006.02.003

[13] S. Horoz, Q. Dai, F. S. Maloney, B. Yakami, J. M. Pikal, X. Zhang, J. Wang, W. Wang, and J. Tang, "Absorption induced by Mn doping of ZnS for improved sensitized quantum-dot solar cells", Physical Review Applied, **3**(2), 024011 (2015), https://doi.org/10.1103/PhysRevApplied.3.024011

[14] P.K. Santra, and P.V. Kamat, "Mn-doped quantum dot sensitized solar cells: a strategy to boost efficiency over 5%", Journal of the American Chemical Society, **134**(5), 2508 (2012), https://doi.org/10.1021/ja211224s

[15] J.K. Salem, T.M. Hammad, S. Kuhn, M.A. Draaz, N.K. Hejazy, R. Hempelmann, J. Mater. Sci: Mater. Electron, **25**, 2177 (2014), https://doi.org/10.1007/s10854-014-1856-8

[16] H.J. Liu, and Y.C. Zhu, "Synthesis and characterization of ternary chalcogenide ZnCdS 1D nanostructures", Materials Letters, **62**(2), 255 (2008), https://doi.org/10.1016/j.matlet.2007.05.011

[17] B. Kumar, P. Vasekar, S.A. Pethe, N.G. Dhere, and G.T. Koishiyev, Thin Solid Films, **517**, 2295 (2009), https://doi.org/10.1016/j.tsf.2008.10.108

[18] B. Dawoud, E.H Amer, and D.M. Gross, "Experimental investigation of an adsorptive thermal energy storage", International journal of energy research, **31**(2), 135 (2007), https://doi.org/10.1002/er.1235

[19] M.C. Baykul, and N. Orhan, "Band alignment of Cd (1− x) ZnxS produced by spray pyrolysis method", Thin Solid Films, **518**(8), 1925 (2010), https://doi.org/10.1016/j.tsf.2009.07.142

[20] A.J. Clayton, M.A. Baker, S. Babar, R. Grilli, P.N. Gibson, G. Kartopu, D.A. Lamb, V. Barrioz, and S.J.C.Irvine, "Effects of Cd1-xZnxS alloy composition and post-deposition air anneal on ultra-thin CdTe solar cells produced by MOCVD", Materials Chemistry and Physics, **192**, 244 (2017), https://doi.org/10.1016/j.matchemphys.2017.01.067

[21] I. Levchuk, C. Würth, F. Krause, A. Osvet, M. Batentschuk, U.R. Genger, C. Kolbeck, P. Herre, H.P. Steinr ück, W. Peukert, and C.J. Brabec, Energy Environ. Sci. **9**, 1083 (2016, https://doi.org/10.1039/C5EE03165F

[22] B. Kumar, P. Vasekar, S.A. Pethe, N.G. Dhere, and G.T. Koishiyev, "ZnxCd1− xS as a heterojunction partner for CuIn1− xGaxS2 thin film solar cells", Thin Solid Films, **517**(7), 2295 (2009), https://doi.org/10.1016/j.tsf.2008.10.108

[23] B. Bibi, B. Farhadi, W. Rahman, and A. Liu, "A novel design of CTZS/Si tandem solar cell: A numerical approach", (2021), https://doi.org/10.21203/rs.3.rs-309446/v1

[24] M.A. Shafi, A. Bouich, K. Fradi, J.M. Guaita, L. Khan, and B. Mari, "Effect of Deposition Cycles on the Properties of ZnO Thin Films Deposited by Spin Coating Method for CZTS-based Solar Cells", Optik, 168854 (2022), https://doi.org/10.1016/j.ijleo.2022.168854

[25] M.A. Shafi, L. Khan, S. Ullah, A. Bouich, H. Ullah, and B. Mari, "Synthesis of CZTS kesterite by pH adjustment in order to improve the performance of CZTS thin film for photovoltaic applications", Superlattices and Microstructures, 107185 (2022), https://doi.org/10.1016/j.spmi.2022.107185

[26] S. Chen, J.H. Yang, X.G. Gong, A. Walsh, and S.H. Wei, "Intrinsic point defects and complexes in the quaternary kesterite semiconductor Cu_2ZnSnS_4", Physical Review B, **81**(24), 245204 (2010), https://doi.org/10.1103/PhysRevB.81.245204

[27] A. Cherouana, and R. Labbani, "Numerical simulation of CZTS solar cell with silicon back surface field", Materials Today: Proceedings, **5**(5), 13795 (2018), https://doi.org/10.1016/j.matpr.2018.02.020

[28] M.A. Shafi, L. Khan, S. Ullah, M.Y. Shafi, A. Bouich, H. Ullah, and B. Mari, "Novel Compositional Engineering for~ 26% Efficient CZTS-Perovskite Tandem Solar Cell", Optik, **253**, 168568 (2022), https://doi.org/10.1016/j.ijleo.2022.168568

[29] H. Movla, D. Salami, and S.V. Sadreddini, "Simulation analysis of the effects of defect density on the performance of pin InGaN solar cell", Applied Physics A, **109**(2), 497 (2012), https://doi.org/10.1007/s00339-012-7062-8

[30] R.S. Crandall, "Modeling of thin film solar cells: Uniform field approximation", Journal of Applied Physics, **54**(12), 7176 (1983), https://doi.org/10.1063/1.331955

[31] M. Uddin, M.S. Hossain, and N. Amin, Study on the prospects of Sb2Te3 back surface field in ZnCdS/ZnCdTe thin film solar cell, in: *2015 2nd International Conference on Electrical Information and Communication Technologies (EICT)*, (IEEE, 2015), pp. 403-406.

[32] S.K. Pandey, and K. Kumar, "Device Modelling and Performance Analysis of CZTS/CdTe Solar Cell", Advanced Science, Engineering and Medicine, **11**(5), 351 (2019), https://doi.org/10.1166/asem.2019.2362

[33] S. Ullah, H. Ullah, F. Bouhjar, M. Mollar, B. Marí, and A. Chahboun, "Influence of zinc content in ternary ZnCdS films deposited by chemical bath deposition for photovoltaic applications", ECS Journal of Solid State Science and Technology, **7**(8), P345 (2018), https://doi.org/10.1149/2.0021808jss

[34] M.A. Shafi, H. Ullah, S. Ullah, L. Khan, S. Bibi, and B.M. Soucase, "Numerical Simulation of Lead-Free Sn-Based Perovskite Solar Cell by Using SCAPS-1D", Engineering Proceedings, **12**(1), 92 (2022), https://doi.org/10.3390/engproc2021012092

[35] Y. Hamakawa, H. Okamoto, and Y. Nitta, "A new type of amorphous silicon photovoltaic cell generating more than 2.0 V", Applied Physics Letters, **35**(2), 187 (1979), https://doi.org/10.1063/1.91031

[36] M.M.A. Moon, M.H. Ali, M.F. Rahman, J. Hossain, and A.B.M. Ismail, "Design and Simulation of FeSi2-Based Novel Heterojunction Solar Cells for Harnessing Visible and Near-Infrared Light", Physica Status Solidi (a), **217**(6), 1900921 (2020), https://doi.org/10.1002/pssa.201900921

**ЧИСЛОВЕ МОДЕЛЮВАННЯ ДЛЯ ПІДВИЩЕННЯ ЕФЕКТИВНОСТІ
ТОНКОПЛІВКОВОГО СОНЯЧНОГО ЕЛЕМЕНТУ НА ОСНОВІ CZTS З ВИКОРИСТАННЯМ SCAPS-1D**

**Мухаммад Аамір Шафіф[a,e,f], Сумайя Бібі[b], Мухаммад Муніб Хан[c],
Харун Сікандар[d], Фейсал Джавед[c], Ханіф Уллах[e], Лайк Хан[a], Бернабе Марі[f]**
[a]Факультет електротехніки та комп'ютерної техніки, Університет COMSATS Ісламабад, Пакистан
[b]Факультет електротехніки, Університет Бахауддіна Закарії, Мултан, Пакистан
[c]Факультет електротехніки, Пакистан Інститут Південного Пенджабу Мулатн, Пакистан
[d]CEME, Коледж електротехніки та машинобудування, Нуст Ісламабад, Пакистан
[e]Факультет електротехніки, Федеральний університет мистецтв і технологій урду, Ісламабад, Пакистан
[f]Інститут дизайну та виробництва (IDF), Політехнічний університет Валенсії (UPV), Іспанія

У цій роботі ми запропонували сонячну батарею з моделлю «Задній контакт *«Back Contact* т/CZTS/ZnCdS/ZnO/Front Contact». CZTS працює як поглинаючий шар, ZnCdS як буферний шар і ZnO як віконний шар із заднім і переднім контактами. Вміст Zn змінювався від 0% до 10%, а заборонена зона змінювалася з 2,42 до 2,90 еВ, як описано в літературі. Вплив зміни ширини забороненої зони спостерігали на продуктивність сонячних елементів за допомогою програмного забезпечення SCAPS-1D.

Ефективність змінювалася за рахунок зміни ширини забороненої зони тонкоплівкового шару ZnCdS. Моделювання проводили при 300 К під час A.M. 1,5 G 1 сонячного освітлення. Діаграма енергетичної забороненої зони була взята з SCAPS, щоб пояснити різні параметри сонячних елементів. Спостерігали вплив ZnCdS, що має різні значення ширини забороненої зони. Потім товщину шару CZTS змінювали, щоб перевірити його дію, і, отже, при 3,0 мкм забезпечили покращену ефективність у 13,83 %. Після оптимізації товщини шару CZTS було досліджено вплив робочої температури на продуктивність сонячного елемента. Зміна коефіцієнта поглинання від $1 \cdot 10^4$ до $1 \cdot 10^9$ cm^{-1} спричинила значний вплив на параметри характеристик сонячної батареї, а також на характеристики J-V і кривої квантової ефективності. При коефіцієнті поглинання $1 \cdot 10^9$ cm^{-1} ККД сонячних елементів збільшується до 16,24%. Це чудове підвищення ефективності сонячних елементів з 13,82% до 16,24%. Після оптимізації всіх параметрів моделювання проводилося при 280 К, товщина CZTS 3,5 мкм, з вмістом Zn в ZnCdS 10% (2,90 еВ) і коефіцієнтом поглинання $1 \cdot 10^9$, ефективність моделі досягала 17,6% при Voc порядку 0,994 В, AT 26,1 мА/см2 і коефіцієнта заповнення 71,4%.
Ключові слова: ZnCdS; CZTS; моделювання; Ефективність; SCAPS-1D